



저작자표시-비영리-변경금지 2.0 대한민국

이용자는 아래의 조건을 따르는 경우에 한하여 자유롭게

- 이 저작물을 복제, 배포, 전송, 전시, 공연 및 방송할 수 있습니다.

다음과 같은 조건을 따라야 합니다:



저작자표시. 귀하는 원저작자를 표시하여야 합니다.



비영리. 귀하는 이 저작물을 영리 목적으로 이용할 수 없습니다.



변경금지. 귀하는 이 저작물을 개작, 변형 또는 가공할 수 없습니다.

- 귀하는, 이 저작물의 재이용이나 배포의 경우, 이 저작물에 적용된 이용허락조건을 명확하게 나타내어야 합니다.
- 저작권자로부터 별도의 허가를 받으면 이러한 조건들은 적용되지 않습니다.

저작권법에 따른 이용자의 권리는 위의 내용에 의하여 영향을 받지 않습니다.

이것은 [이용허락규약\(Legal Code\)](#)을 이해하기 쉽게 요약한 것입니다.

[Disclaimer](#)

공학박사 학위논문

**Preparation of Graphene Oxide Nanosheets-  
Embedded Thin-Film Composite Reverse  
Osmosis Membrane with High Flux, Anti-  
Biofouling, and Chlorine Resistance**

높은 투수도, 방오성, 내염소성을 가지는  
그래핀 옥사이드 함유 역삼투용  
박막 복합 분리막 제조

2016 년 8 월

서울대학교 대학원

화학생물공학부

채 희 로



## **Abstract**

# **Preparation of Graphene Oxide Nanosheets- Embedded Thin-Film Composite Reverse Osmosis Membrane with High Flux, Anti- Biofouling, and Chlorine Resistance**

Hee-Ro Chae

School of Chemical and Biological Engineering

The Graduate School

Seoul National University

Recently, a few studies reported that the coating of graphene oxide (GO) nanosheets on a thin-film composite (TFC) reverse osmosis (RO) membrane effectively enhanced chlorine resistance and anti-biofouling property. However, it turned out that the GO coating could not improve membrane water permeability because the GO coating layer interfered with water permeation. In this study, GO

nanosheets were embedded in TFC RO membranes to solve such interference with water permeation. The performances of GO-embedded TFC RO membranes were evaluated in terms of chlorine resistance, anti-biofouling property, and water permeability and factors affecting such performances were investigated.

Firstly, the TFC RO membrane with GO nanosheets embedded in the active layer (A-GO-TFC membrane) was fabricated via addition of the size-controlled GO nanosheets in MPD aqueous solution. The GO nanosheets embedded in active layer enhanced chlorine resistance of a membrane via shielding the active layer and forming hydrogen bonding with the active layer. In addition, the embedment of GO nanosheets increased hydrophilicity and negative zeta potential and decreased surface roughness of a membrane. As a result, the anti-biofouling property of the membrane was dramatically ameliorated. Furthermore, water permeability was significantly improved due to the high membrane hydrophilicity and low interference of dispersed GO nanosheets with the water permeation.

Secondly, the TFC RO membrane with GO nanosheets embedded in both the active and support layers (AS-GO-TFC membrane) was prepared via addition of GO nanosheets in MPD and PSf solutions. The embedment of GO nanosheets in the support layer further raised the hydrophilicity, negative zeta potential, and even surface roughness due to the functional groups of GO nanosheets in both of active and support layer and high surface roughness of GO embedded support layer. In addition, the GO embedded support layer could make GO nanosheets in MPD solution disperse more evenly. Consequently, the water flux and anti-biofouling

property of the AS-GO-TFC membrane were significantly enhanced compared with the A-GO-TFC membrane.

The successful improvement of the membrane performances such as the water permeability, salt rejection, chlorine resistance, and anti-biofouling property by embedding GO nanosheets in both the active and support layers of the TFC membrane could be expanded to industrial RO system and various environmental engineering systems.

### **Keywords**

Thin-film composite (TFC) membrane, Reverse osmosis (RO), Graphene oxide (GO), Nanocomposite, Anti-biofouling, Chlorine resistance

***Student Number:*** 2010-23334

# Table of Contents

<b>Abstract .....</b>	<b>i</b>
<b>List of Figures .....</b>	<b>vii</b>
<b>List of Tables.....</b>	<b>xvii</b>
<b>I. Introduction .....</b>	<b>1</b>
I.1. Background.....	2
I.2. Objectives .....	5
<b>II. Literature Review.....</b>	<b>7</b>
<b>II.1. Graphene oxide nanosheets.....</b>	<b>8</b>
II.1.1. Introduction .....	8
II.1.2. Synthesis of graphene oxide nanosheets .....	13
II.1.3. Preparation of graphene oxide nanosheets embedded polymeric membrane for water treatment.....	18
II.1.4. Preparation of graphene oxide-layered membrane. ....	19
II.1.5. The shape of the graphene and graphene oxide nanosheets on a substrate.....	23
<b>II.2.Phase separation for water treatment membrane .....</b>	<b>26</b>
II.2.1. Introduction .....	26
II.2.2. Nonsolvent induced phase separation method to prepare water treatment membrane.....	31
II.2.3. Interior structures of a membrane prepared by NIPS.....	37
II.2.4. Control factors for membrane interior structure at NIPS method.....	41

<b>II.3. Interfacial polymerization for reverse osmosis membrane .....</b>	<b>49</b>
II.3.1. Introduction .....	49
II.3.2. Interfacial polymerization method to prepare thin-film composite reverse osmosis membrane.....	56
II.3.3. Recent trend of reverse osmosis membrane .....	59
<b>III. Thin-Film Composite Reverse Osmosis Membrane with         Graphene Oxide-Embedded in the active layer .....</b>	<b>72</b>
<b>III.1. Introduction .....</b>	<b>73</b>
<b>III.2. Experimental.....</b>	<b>77</b>
III.2.1. Materials.....	77
III.2.2. Preparation of graphene oxide nanosheets .....	78
III.2.3. Preparation of GO-TFC membrane .....	80
III.2.4. Characterization of graphene oxide nanosheets .....	81
III.2.5. Characterization of GO-TFC membrane.....	83
III.2.6. Performance of GO-TFC membrane .....	86
<b>III.3. Results and discussion .....</b>	<b>88</b>
III.3.1. Characterization of graphene oxide nanosheets .....	88
III.3.2. Characterization of GO-TFC membrane.....	94
III.3.3. Performance of GO-TFC membrane .....	105
<b>III.4. Conclusions .....</b>	<b>113</b>
<b>IV. Synergetic Effect of Graphene Oxide Nanosheets         embedded in the Active and Support Layers on the         performance of Thin-Film Composite Membranes .....</b>	<b>114</b>
<b>IV.1. Introduction.....</b>	<b>115</b>

<b>IV.2. Experimental</b> .....	<b>117</b>
IV.2.1. Materials.....	117
IV.2.2. Preparation of graphene oxide nanosheets .....	118
IV.2.3. Preparation of GO-support layers .....	119
IV.2.4. Preparation of GO-TFC membranes .....	120
IV.2.5. Characterization of graphene oxide nanosheets.....	121
IV.2.6. Characterization of the GO-support layers.....	122
IV.2.7. Characterization of the GO-TFC membranes.....	123
IV.2.8. Evaluation of the GO-TFC membrane performance.....	124
<b>IV.3. Results and discussion</b> .....	<b>126</b>
IV.3.1. Characterization of the graphene oxide nanosheets .....	126
IV.3.2. Characterization of the GO-support layers.....	129
IV.3.3. Characterization of the GO-TFC membranes.....	132
IV.3.4. Performance of the GO-TFC membranes.....	140
<b>IV.4. Conclusions</b> .....	<b>157</b>
<b>V. Conclusions</b> .....	<b>158</b>
<b>V.1. Conclusions</b> .....	<b>159</b>
<b>국문 초록</b> .....	<b>160</b>
<b>Reference</b> .....	<b>162</b>

## List of Figures

<b>Figure II-1. The possible structure model of a GO nanosheet supposed by (a) Lerf et al., (b) Compton et al., (c) He et al., (d) Szabo et al. (Lerf, He et al. 1998, Compton, Nguyen 2010, He, Klinowski et al. 1998, Szabo, Berkesi et al. 1997, Dreyer, Park, et al. 2009).....</b>	<b>11</b>
<b>Figure II-2. Schematic procedure to fabricate GO nanosheets (Li, Müller et al. 2008) .....</b>	<b>15</b>
<b>Figure II-3. Schematic illustrating the chemical structure of graphite oxide and GO nanosheets (Potts, Dreyer et al. 2011) .....</b>	<b>16</b>
<b>Figure II-4. (a) AFM images of GO nanosheets prepared via chemical exfoliation. (b) Thickness of them (Wang, Wang et al. 2015)...</b>	<b>17</b>
<b>Figure II-5. Schematic illustration of GO-layered membrane. GO nanosheets were cross-linked by TMC (Hu, Mi 2013) .....</b>	<b>20</b>
<b>Figure II-6. Schematic illustration of GO-layered membrane. GO nanosheets and aminated GO nanosheets were deposited alternately, and cross-link formed between them (Choi, Choi et al. 2013) .....</b>	<b>21</b>
<b>Figure II-7. Schematic illustration of GO-layered membrane. GO nanosheets formed covalent bonding with membrane surface via cross-linker (Perreault, Tousley et al. 2013).....</b>	<b>22</b>

<b>Figure II-8. AFM images of GO nanosheets on a substrate. GO nanosheets were (a),(b) folded and stacked, or (c),(d) wrinkled. The bright spots in (c) and (d) is Cu<sup>2+</sup> particles (Yang, Chang et al. 2010)</b>	<b>24</b>
<b>Figure II-9. A SEM image of GO nanosheets on a substrate. There are many wrinkles, especially indicated as the circles (Xie, Spallas 2012)...</b>	<b>25</b>
<b>Figure II-10. Classification of water treatment membrane based on membrane pore size (Lalia, Kochkodan et al. 2013).....</b>	<b>28</b>
<b>Figure II-11. Schematic illustration of casting polymer solution (grey region) in a substrate using casting knife (Baker 2004).....</b>	<b>32</b>
<b>Figure II-12. Schematic illustration of liquid-liquid demixing, a part of NIPS. P: polymer, S: solvent, NS: non-solvent (Witte, Dijkstra et al. 1996) .....</b>	<b>33</b>
<b>Figure II-13. The phase diagram of the three-component mixture. NIPS proceeds along the line A-B (Lloyd 1985) .....</b>	<b>36</b>
<b>Figure II-14. (a) The sponge-like structure membrane and (b) the finger-like structure membrane (Lloyd 1985).....</b>	<b>39</b>
<b>Figure II-15. (a) The early, (b) middle, and (c) late formation stages of the finger-like structure membrane (Lloyd 1985). Precipitant is a</b>	

synonym of the non-solvent..... 40

**Figure II-16. The SEM images of the membrane with cross-sectional view. a) 12 % cellulose acetate in DMAc b) 12 % polyamide in DMSO, c) 12 % polysulfone in DMF. The SEM images shows effect of polymer and solvent set on membrane interior structure (Lloyd 1985) ..... 43**

**Figure II-17. The SEM images of the membrane with top view. The surface pore size of the membrane was decreased with increasing polymer concentration. The number under the lower left-handed corner of each image represents the polymer concentration of PSf in NMP (Misdan, Lau, et al. 2013)..... 45**

**Figure II-18. The SEM images of the membrane with cross-sectional view. The macrovoid size of the membrane was decreased with increasing polymer concentration. In other words, the membrane interior structure changed from finger-like structure to sponge-like structure with increasing polymer concentration. The number under each image represents the polymer concentration of PA 1in NMP (Lloyd 1985) ..... 46**

**Figure II-19. The SEM images of the membrane with cross-sectional view increasing concentration of LiCl (left) and PVP (right) in the casting solution (Fontananova, Jansen et al. 2006) ..... 48**

**Figure II-20. The Schematic procedure of the IP. a) Support membrane was immersed in DI water overnight. b) Surface of the support membrane contact an aqueous MPD solution for 10 min c) Aqueous MPD droplets was squeezed from the support membrane with a rubber roller. d) Surface of the support membrane contact a solution of TMC in n-dodecane for 1 min, e) Surface of the support membrane was rinsed with n-hexane. f) The prepared TFC membrane was stabilized and stored in DI water until use (Xie, Geise et al. 2012)..... 58**

**Figure II-21. The transmission electron microscopy (TEM) images with cross-sectional view of a) TFC membrane and TFN membrane with zeolite NP embedded in its active layer (Jeong, Hoek et al. 2007) ..... 62**

**Figure II-22. Schematic Illustration of the TFN membrane including CNTs. Water Molecules rapidly transfer via fluid transport channel (Kim, Choi et al. 2014) ..... 63**

**Figure II-23. Proposed formation pathway of g) an Ag/MWNT grafted TFC membrane: a) pristine MWNT, b) acid-treated MWNT, c) PEG-grafted MWNT, d) silver NPs deposited MWNT, e) EDC-linked Ag/MWNT, and f) EDA-attached membrane surface (Gunawan, Guan et al. 2011)..... 65**

<b>Figure II-24. Schematic illustration for immobilization of Ag NPs on TFC membrane surface (Yin, Yang et al. 2013).....</b>	<b>66</b>
<b>Figure II-25. a) Schematic illustration of mLBL mechanism and b) procedure (Chan, Lee et al. 2012).....</b>	<b>69</b>
<b>Figure II-26. a) Schematic illustration of automated spin-coater system with syringe pump (Chan, Lee et al. 2012).....</b>	<b>70</b>
<b>Figure III-1. Schematic illustration of GO molecular structure.....</b>	<b>75</b>
<b>Figure III-2. SEM surface images of three TFC membranes: TFC membranes prepared (a, a', and a'') without GO nanosheets and with (b, b', and b'') non-fractionated and (c, c', and c'') fractionated GO nanosheets. The GO concentration in MPD solutions for the A- and AS-GO-TFC membranes was 15 ppm.....</b>	<b>79</b>
<b>Figure III-3. (a) Cross-sectional SEM image, (b) active layer part of the SEM image, and (c) silhouetted active layer part.....</b>	<b>85</b>
<b>Figure III-4. (a) SPM image of GO nanosheets (white spots) on silicon wafer (dark background) and (b) lateral size and thickness of several GO nanosheets .....</b>	<b>90</b>
<b>Figure III-5. (a) Size distributions in volume fraction and (b) number concentration at each given size of fractionated and non-fractionated GO nanosheets.....</b>	<b>91</b>

<b>Figure III-6. TEM image of fractionated GO nanosheets.....</b>	<b>92</b>
<b>Figure III-7. (a) FTIR spectrum and (b) C1s XPS spectrum of fractionated GO nanosheets .....</b>	<b>93</b>
<b>Figure III-8. (a) Raman spectra of 152-GO-TFC membrane and TFC membrane without GO nanosheets. D and G represent the typical GO peaks. Schematic molecular structure images of (b) PSF and (c) PA .....</b>	<b>95</b>
<b>Figure III-9. Contact angle, surface zeta potential and surface average roughness of the 0, 15, 38, and 76-GO-TFC membranes .....</b>	<b>98</b>
<b>Figure III-10. SPM surface images for the (a) 0, (b) 15, (c) 38, and (d) 76-GO- TFC membranes. The ridge heights and surface roughness were observed to decrease with increasing GO content.....</b>	<b>99</b>
<b>Figure III-11. SEM images of top and cross-sectional views of 0-GO-TFC (a) and (c) and 76-GO-TFC membranes (b) and (d) .....</b>	<b>100</b>
<b>Figure III-12. Average thickness of polyamide layer as a function of GO content for the 0, 15, 38, and 76-GO-TFC membranes.....</b>	<b>101</b>
<b>Figure III-13. Oxygen weight fraction of the 0, 15, 38, and 76-GO-TFC membranes measured by EDS.....</b>	<b>104</b>
<b>Figure III-14. The water fluxes and salt rejections of the 0, 15, 38, and 76-GO- TFC membranes in a cross-flow filtration of 2000-ppm NaCl</b>	

solution. Pre-filtration was conducted at 350 psi for 30 min to achieve membrane compaction before the main filtration, which was performed at 225 psi for 30 min ..... 107

Figure III-15. The water fluxes of the 0, 15, 38, and 76-GO-TFC membranes containing fractionated or non-fractionated GO nanosheets. The measurement condition was same as above ..... 108

Figure III-16. CLSM images of biofilm formed on the (a) 0, (b) 15, (c) 38, and (d) 76-GO-TFC membranes and (e) biovolume of cells attached on the membrane surface with corresponding GO content. GFP tagged PAO1 were cultured in a CDC reactor in which membranes containing various GO contents were set .....110

Figure III-17. Salt rejections and water fluxes of the 0, 15, 38, and 76-GO-TFC membranes before and after chlorination which was conducted with a 2000-ppm NaOCl solution (pH 7) for 24 h .....112

Figure IV-1. (a) SPM image of the GO nanosheets on silicon wafer. The background wave is the wafer roughness. (b) The thickness was calculated as the difference between the maximum and minimum absolute heights. The wave pattern is due to the wafer roughness..... 127

Figure IV-2. FTIR spectrum of GO nanosheets ..... 128

Figure IV-3. (a) Contact angle (n=6) and (b) surface zeta potential (n=3) of the

control support and GO-support layers .....	130
<b>Figure IV-4. Average pore size (n=3) and average surface roughness (n=9) of the control support and GO-support layers. ....</b>	<b>131</b>
<b>Figure IV-5. Raman spectra of (a) TFC, (b) S-GO-TFC, (c) A-GO-TFC, and (d) AS-GO-TFC membranes (n=2). The GO concentration in MPD solutions for the A- and AS-GO-TFC membranes was 76 ppm... ..</b>	<b>134</b>
<b>Figure IV-6. (a) Contact angle (n=6) and (b) surface zeta potential (n=3) of the TFC, S-GO-TFC, A-GO-TFC, and AS-GO-TFC membranes..... ..</b>	<b>136</b>
<b>Figure IV-7. Average surface roughness of the TFC, S-GO-TFC, A-GO-TFC, and AS-GO-TFC membranes (n=5). The average surface roughness of smooth regions on the A-GO-TFC membrane with 152 ppm is also plotted.....</b>	<b>137</b>
<b>Figure IV-8. SEM images of the (a) A-GO-TFC and (b) AS-GO-TFC membranes with 152 ppm of GO concentration in MPD solution at 1000× magnification, and of (c) a smooth region and (d) a rough region of A-GO-TFC at 30000× magnification. The dashed regions indicate the smooth regions .....</b>	<b>139</b>
<b>Figure IV-9. (a) Water flux and (b) salt rejection of the TFC, S-GO-TFC, A-GO-TFC, and AS-GO-TFC membranes with 38, 76, 114, and</b>	

152 ppm of GO concentration in an MPD solution (n=3) ..... 142

**Figure IV-10. Comparison of the water permeability and salt rejection of the AS-GO-TFC membrane (152 ppm of GO concentration in an MPD solution) prepared in this study to various reported TFC membranes with nanoparticles in their active layers. All the reported TFC membranes showed more than 80% of salt rejections at 2000 ppm NaCl solutions. The diagonal lines represented the trade-off lines for water permeability and salt rejection..... 145**

**Figure IV-11. Comparison of the water permeability and salt rejection of the AS-GO-TFC membrane (152 ppm of GO concentration in an MPD solution) prepared in this study to various reported NF/RO membranes applied GO. Only the data which exhibited water permeability over 1.0 L/m<sup>2</sup>·h·bar and salt rejections over 80% of at 2000 ppm NaCl feed solution were showed. The diagonal lines represented the trade-off lines for water permeability and salt rejection. .... 147**

**Figure IV-12. CLSM images of biofilm formed on the (a) TFC, (b) S-GO-TFC, (c) A-GO-TFC, and (d) AS-GO-TFC membranes. The GO concentration in MPD solutions for the A- and AS-GO-TFC membranes was 76 ppm. Green color indicates microorganisms ..... 150**

<b>Figure IV-13. The biovolume of cells attached on the TFC, S-GO-TFC, A-GO-TFC, and AS-GO-TFC membranes (n=9) .....</b>	<b>151</b>
<b>Figure IV-14. The relative water flux with operation time of the TFC and AS-GO-TFC membranes with 76 and 152 ppm of GO concentration in an MPD solution (n=3) .....</b>	<b>152</b>
<b>Figure IV-15. Water fluxes and salt rejection of the TFC, S-GO-TFC, A-GO-TFC, and AS-GO-TFC membranes before and after chlorine treatment, which was conducted with 5000 ppm of NaOCl solution for 16 h (n=3). The thick boundaries indicate water fluxes and salt rejection after the chlorine treatment. The GO concentration in MPD solutions for the A- and AS-GO-TFC membranes was 76 ppm.....</b>	<b>155</b>

## **List of Tables**

<b>Table II-1. The features of the synthesis methods for graphene and GO nanosheets (Kumar and Lee 2013).....</b>	<b>12</b>
<b>Table II-2. Summary of the classification of a water treatment membrane, preparation methods, and commonly used materials were summarized (Lalia, Kochkodan et al. 2013).....</b>	<b>29</b>
<b>Table II-3. The features of various phase separation methods (Mulder 1996, Lloyd 1985, Strathmann and Kock 1977, Strathmann 1985, Lalia, Kochkodan et al. 2013) .....</b>	<b>30</b>
<b>Table II-4. The performance and chemical structure of asymmetric RO membranes (Lee, Arnot et al. 2011).....</b>	<b>50</b>
<b>Table II-5. The performance and chemical structure of TFC RO membranes (Lee, Arnot et al. 2011).....</b>	<b>52</b>
<b>Table IV-1. The water flux and salt rejection of the NF/RO membranes applied GO.....</b>	<b>146</b>
<b>Table IV-2. The summary of the changes in membrane properties and performances depending on types of GO-TFC membrane .....</b>	<b>156</b>



# **Chapter I**

## **Introduction**

## **I.1. Background**

Recently, water scarcity has become worse due to change in climate and increment of population. Consequently, the demands for clean water and water purification technique have been increased (Oki, Kanae 2006). One of the best approaches to solve the problem of water shortage is seawater desalination since the amount of seawater is superabundant. Nowadays the reverse osmosis (RO) process has emerged as the most popular technique for seawater desalination (Greenlee, Lawler et al. 2009, Miller, Shemer et al. 2015) due to its highest energy efficiency among desalination techniques (Elimelech and Phillip 2011).

The RO membrane which is the key element for the energy efficiency of RO process has been developed over the last 40 years (Clark, Allgeier et al. 1998, Escobar, Hoek et al. 2005) since Loeb invented asymmetric CA membrane (Loeb and Sourirajan 1962). However, it is still required to improve the RO membrane in terms of permselectivity, anti-biofouling property, and chlorine resistance (Clark, Allgeier et al. 1998, Escobar, Hoek et al. 2005). The permselectivity is an essential property of RO membrane. Furthermore, anti-biofouling property suppresses biofouling which leads to higher energy consumption (Tiraferrri, Vecitis et al. 2011, Kwak, Kim et al. 2001), and chlorine resistance is also required for polyamide (PA) RO membrane because PA is very vulnerable to chlorine (Elimelech, Phillip 2011, Glater, Hong et al. 1994).

Hydrophilic nanoparticles (NPs) have been applied to RO membrane via several methods. As the result water permeability (Barona, Lim et al. 2013) and

anti-biofouling property (Goosen, Sablani et al. 2004) were quite enhanced. For example, several hydrophilic NPs such as zeolite (Jeong, Hoek et al. 2007), alumina (Saleh, Gupta 2012), titanium dioxide (Lee, Im et al. 2008), and functionalized carbon nanotube (Kim, Choi, et al. 2014) have been used via embedment of NPs in active and/or support layers (Kim, Choi, et al. 2014, Pendergast, Ghosh, et al. 2013, Kim, Hwang, et al. 2012), chemical grafting (Tiraferri, Vecitis, et al. 2011), layer-by-layer assembly (Sun, Chung, et al. 2013), self-assembly (Bae, Kim, et al. 2006), vacuum filtration process (Kim, Baek, et al. 2014), chemical vapor deposition (Yang, Xu, et al, 2011), electrostatic attraction (Ben-Sasson, Zodrow, et al. 2014), and adsorption–reduction (Zhang, Qiu, et al. 2013). To go one step further, nowadays another excellent hydrophilic nanoparticle, graphene oxide (GO) nanosheet, has attracted great attention because extremely large specific surface area of a GO nanosheet has myriad hydrophilic and negatively charged functional groups (Lerf, He et al. 1998, Compton, Nguyen 2010, He, Klinowski et al. 1998).

In previous studies, GO nanosheets was coated on upper side, bottom side, or both sides of PA active layer via layer-by-layer deposition of GO or covalent bonding between GO nanosheets and PA surface (Kim, Hyeon et al. 2013, Perreault, Tousley et al. 2013, Choi, Choi et al. 2013). As the result, chlorine resistance and anti-fouling property of GO-coated TFC membrane were improved. However, it was difficult to enhance water flux because GO coating layer interfered water permeation. Therefore, a new method for application of GO nanosheets to a RO membrane should be developed to improve chlorine resistance, anti-fouling

property, and even permselectivity.

## **I.2. Objectives**

The objectives of the study were to develop a novel RO membrane with outstanding permselectivity, anti-biofouling property, and chlorine resistance via embedment of GO nanosheets in both the active and support layers of a TFC membrane. The detailed objectives are as follows:

- (1) Preparation of TFC membrane with GO nanosheets embedded in the active layer.

As an early stage study, GO nanosheets were embedded in the active layer of a TFC membrane via adding GO nanosheets to an MPD aqueous solution. Then, the water flux, salt rejection, chlorine resistance, and anti-biofouling property of TFN membrane with GO nanosheets were evaluated to confirm the effect of GO nanosheets embedment. To examine the causes of change in membrane performance, hydrophilicity, negative surface zeta potential, and surface roughness were also evaluated.

- (2) Preparation of TFC membrane with GO nanosheets embedded in both the active and support layers.

TFC membrane with GO nanosheets embedded in both the active and support layers was prepared based on the early stage study. Then, the causes of changes in its permselectivity, anti-biofouling property, and

chlorine resistance were investigated by comparing its properties and the properties with performances of TFC membranes with GO nanosheets embedded only in the active or support layers.

# **Chapter II**

## **Literature Review**

## **II.1. Graphene oxide nanosheets**

### **II.1.1. Introduction**

Graphene and graphene oxide (GO) nanosheet, two-dimensional layers of  $sp^2$ -bonded carbon, have attracted great interest from many researchers due to their outstanding electron mobility ( $230,000 \text{ cm}^2 \cdot \text{V}^{-1} \cdot \text{s}^{-1}$  at 300 K) (Bolotin, Sikes et al. 2008), thermal conductivity ( $5,300 \text{ W} \cdot \text{m}^{-1} \cdot \text{K}^{-1}$ ) (Balandin, Ghosh et al. 2008, Stankovich, Dikin et al. 2006), thermal stability (200 °C) (Stankovich, Dikin et al. 2007), specific surface area ( $2630 \text{ m}^2 \cdot \text{g}^{-1}$ ) (Bonaccorso, Colombo et al. 2015), and mechanical properties (Young's modulus of 1 TPa, tensile strength of 130 GPa) (Lee, Wei et al. 2008).

Because of those excellent properties, graphene and GO nanosheets were applied to various fields such as transistor (Novoselov, Geim et al. 2004), sensor (Schedin, Geim et al. 2007), dye-sensitized solar cell (Wang, Zhi et al. 2008), transparent electrodes (Kim, Zhao et al. 2009), flexible display (Ahn, Hong 2014), electronic inks (Torrise, Coleman 2014), battery (Liu 2014), preventive agent against corrosion (Böhm 2014). Especially, GO nanosheets were also applied to water treatment membranes because hydrophilicity and negative surface zeta potential enhance membrane properties (Wang, Yu et al. 2012, Zhang, Wu et al. 2013, Lee, Chae et al. 2013).

GO nanosheet have numerous functional groups such as epoxy, hydroxyl, carbonyl and carboxyl groups due to their large specific surface area (He, Klinowski et al. 1998, Lurf, He et al. 1998, Stankovich, Dikin et al. 2006, Compton, Nguyen 2010). These functional groups is the origin of the outstanding hydrophilicity. However, their structure is not exactly established, and just several possible models were supposed as shown in Figure II-1 (Lurf, He et al. 1998, Compton, Nguyen 2010, He, Klinowski et al. 1998, Szabo, Berkesi et al. 1997, Dreyer, Park, et al. 2009). In addition, GO nanosheets are well dispersed in aqueous solution and maintain the colloids state stably due to electrostatic repulsion caused by ionization of the hydroxyl and carboxylic acid groups (Li, Müller et al. 2008).

Several synthesis methods for graphene and GO nanosheets have been developed to utilize their exceptional properties. Graphene and GO nanosheets can be produced by chemical vapor deposition (Eizenberg and Blakely 1979, Aizawa, Souda et al. 1990), mechanical exfoliation of highly ordered pyrolytic graphite (Novoselov, Geim et al. 2004), epitaxial graphene growth (Berger, Song et al. 2006), and plasma synthesis (Dato, Radmilovic et al. 2008). These methods are suitable to fabricate graphene with a relatively perfect structure and excellent properties. Another preparation method is chemical exfoliation based on Hummers method (Stankovich, Dikin et al. 2006, Hummers, Offeman 1958). This method is appropriate for mass production of GO nanosheets (Rafiee, Rafiee et al. 2009, Lin, Shen et al. 2012). Moreover the method is quite simple and inexpensive to fabricate large scale graphene and consequently widely used for researches and

productions (Paredes, Villar-Rodil et al. 2011, Stankovich, Dikin et al. 2006, Lin, Shen et al. 2012). Detailed features for the current synthesis methods of graphene and GO nanosheets were summarized in Table II-1 (Kumar and Lee 2013).

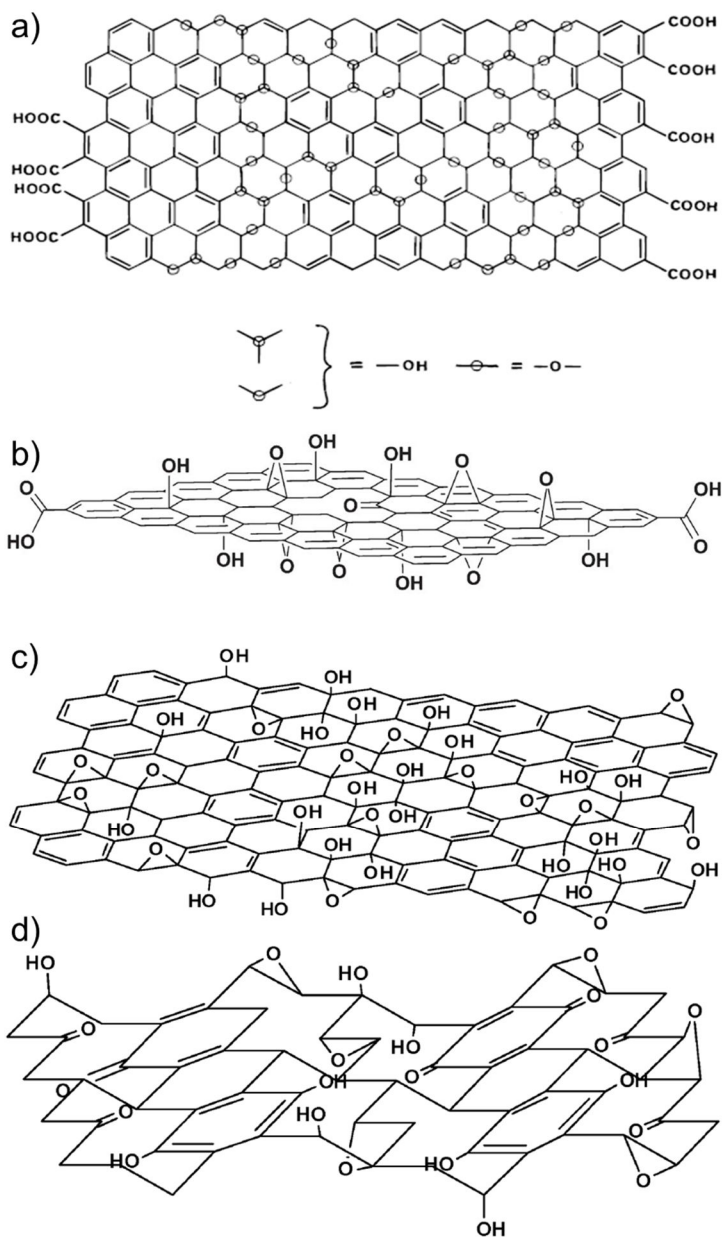


**Figure II-1. The possible structure model of a GO nanosheet supposed by (a) Lerf et al., (b) Compton et al., (c) He et al., (d) Szabo et al. (Lerf, He et al. 1998, Compton, Nguyen 2010, He, Klinowski et al. 1998, Szabo, Berkesi et al. 1997, Dreyer, Park, et al. 2009).**

**Table II-1. The features of the synthesis methods for graphene and GO nanosheets (Kumar and Lee 2013).**

synthesis method	For graphene synthesis	For GO synthesis	For Large-scale synthesis
Chemical vapor deposition	M	P	G
Mechanical exfoliation	G	P	P
Epitaxial growth	M	P	P
Plasma synthesis	P	P	G
Chemical exfoliation	P	G	G

G = Good, M = Moderate, P=Poor

## II.1.2. Synthesis of graphene oxide nanosheets

GO nanosheets are usually prepared via chemical exfoliation method as shown in Figure II-2 (Li, Müller et al. 2008). Firstly, graphite powder was oxidized by oxidizing agents such as  $\text{KMnO}_4$  and  $\text{H}_2\text{SO}_4$  (Hummer's method) or  $\text{KClO}_3$  and  $\text{HNO}_3$  (Brodie method) (Dreyer, Park et al. 2009) and converted to graphite oxide. In this step, many oxygen atoms are added to graphite and make bond between them. Consequently, epoxy, hydroxyl, carbonyl and carboxyl groups were created as shown in Figure II-3. Interlayer distance of graphite oxide are from 0.6 nm under high vacuum (Buchsteiner, Lerf et al. 2006) to 0.8 nm at 45% relative humidity (Dikin, Stankovich et al. 2007) as shown in Figure II-3. The cause of the difference between the values is that water molecules intercalate Interlayer of graphite oxide (Buchsteiner, Lerf et al. 2006).

Because graphite oxide is hydrophilic and has expanded interlayer distance, graphite oxide is relatively readily exfoliated in aqueous solution via ultrasonication. Through this step, graphite oxide is separated into several layers, which are called GO nanosheets (Park and Ruoff 2009). Figure II-3 shows the structural difference between graphite oxide and GO nanosheets. The negative zeta potential of GO nanosheets caused by their carboxylate groups generates electrostatic repulsion between each other. Therefore, GO nanosheets stably dispersed in aqueous solution (Park and Ruoff 2009). However, GO nanosheets can be aggregated over their critical coagulation (aggregation) concentrations (Wu, Liu et al. 2013).

The GO nanosheets prepared via chemical exfoliation were successfully exfoliated as single-layer as shown in Figure II-4 (Wang, Wang et al. 2015, Gómez-Navarro, Weitz et al. 2007, Stankovich, Dikin et al. 2007). Their lateral size can be controlled via sonication in a range of nanometer (Dreyer, Park et al. 2009, Li, Zhang et al. 2009).

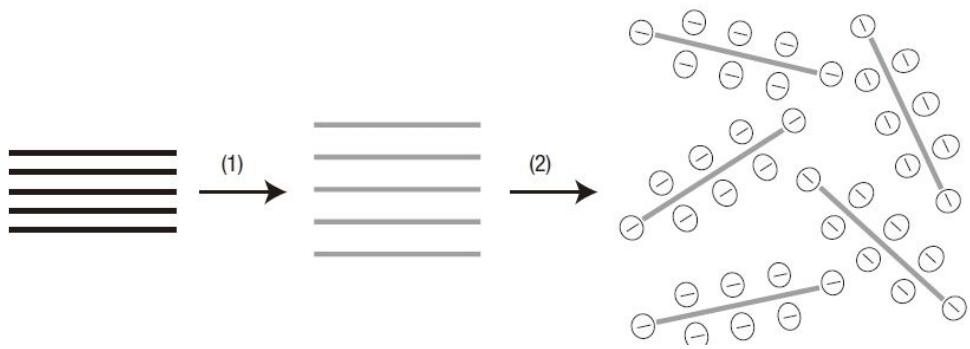


**Figure II-2. Schematic procedure to fabricate GO nanosheets (Li, Müller et al. 2008).**



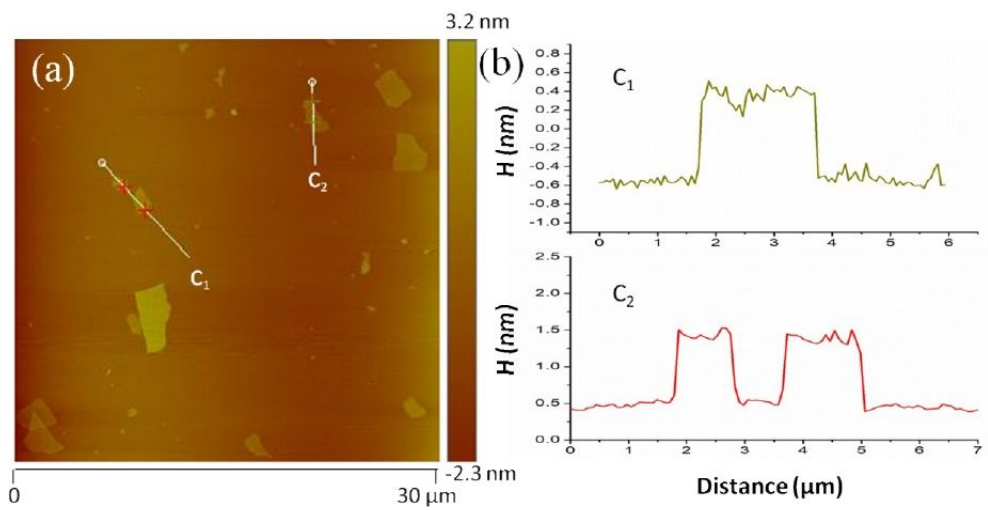


**Figure II-4. (a) AFM images of GO nanosheets prepared via chemical exfoliation. (b) Thickness of them (Wang, Wang et al. 2015).**

### **II.1.3. Preparation of graphene oxide nanosheets embedded polymeric membrane for water treatment.**

The GO nanosheets embedded polymeric membranes for water treatment were reported (Wang, Yu et al. 2012, Jin, LV et al. 2013, Lee, Chae et al. 2013). Firstly, the solvent of graphitic oxide, water, was replaced with polar organic solvents (N,N-dimethylacetamide (DMAc), N,N-dimethylformamide (DMF), or N-methyl-2-pyrrolidinone(NMP)) before sonication, and then the graphitic oxide in organic solvent were exfoliated via ultrasonication. Then polymer (polyvinylidene fluoride (PVDF), polyethersulfone (PES), or polysulfone(PSf)) was dissolved in the GO organic solution. Then, the solution was casted support layer and the casted solution was immersed in non-solvent, water in order to induce non-solvent phase separation (NIPS). The prepared GO nanosheets embedded polymeric membranes exhibited higher water permeability and anti-biofouling caused by their hydrophilicity and negative surface zeta potential.

#### **II.1.4. Preparation of graphene oxide-layered membrane.**

The GO-layered membrane was prepared via deposition of GO nanosheets on PSf, PES, polyamide (PA) membrane (Hu, Mi 2013, Choi, Choi et al. 2013, Kim, Hyeon et al. 2013, Perreault, Tousley et al. 2013). One method is layer-by-layer deposition of GO nanosheets on polysulfone membrane and cross-linking the GO nanosheets using 1,3,5-benzenetricarbonyl trichloride (TMC) (Figure II-5) (Hu, Mi 2013). Another layer-by-layer deposition method is using negatively charged GO nanosheets alternately with positively charged aminated GO nanosheets. Then, cross-link formed between them (Figure II-6) (Choi, Choi et al. 2013, Kim, Hyeon et al. 2013). The other method is covalent bonding between membrane surface and GO nanosheets using cross-linkers (Figure II-7) (Perreault, Tousley et al. 2013). Water pass through interlayer channel between GO-layer, however salts do not pass through the interlayer channel. Because the height of the interlayer channel is approximately 4.5 Å (Joshi, Carbone et al. 2016).

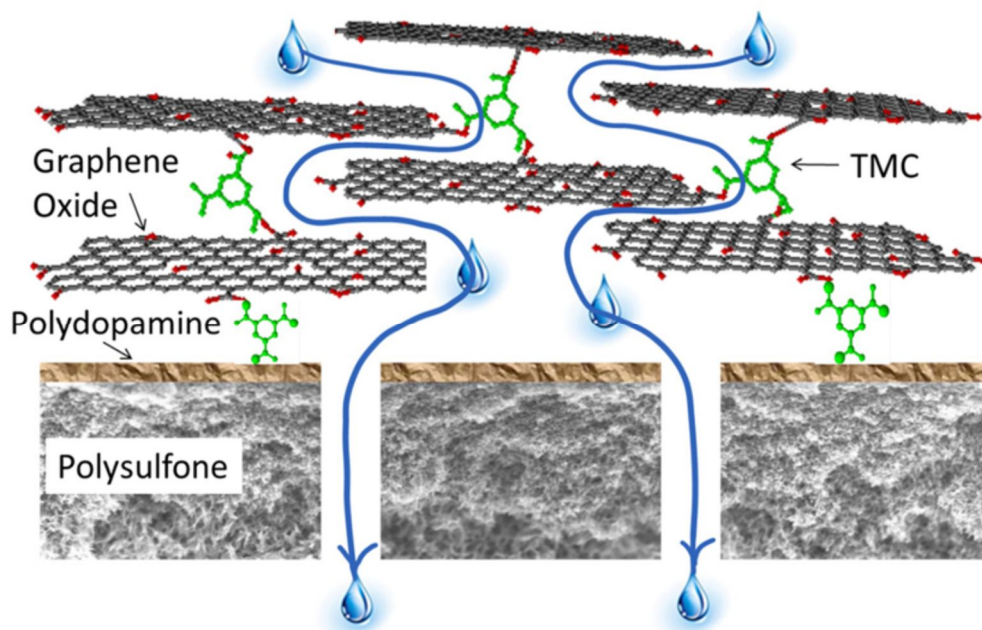


**Figure II-5. Schematic illustration of GO-layered membrane. GO nanosheets were cross-linked by TMC (Hu, Mi 2013).**

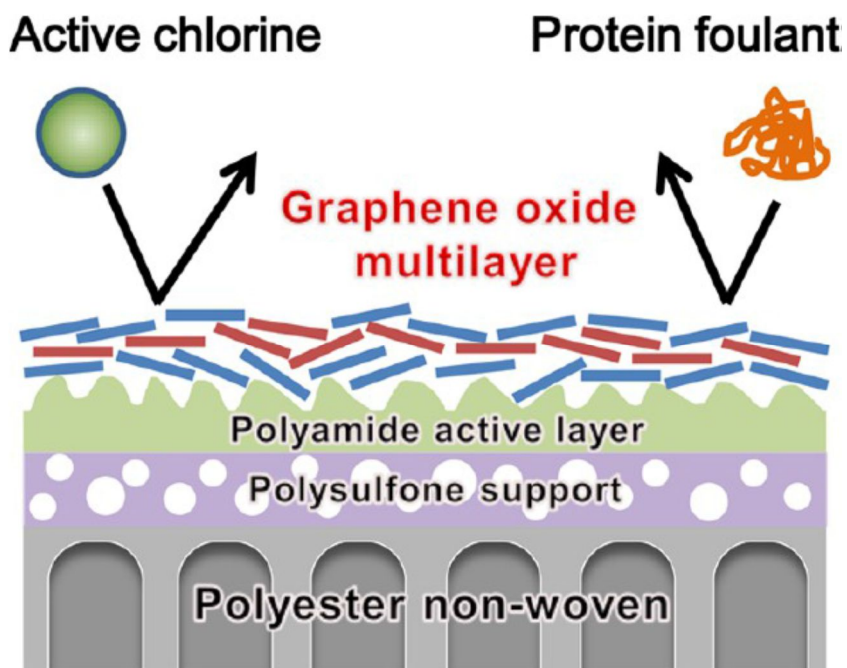
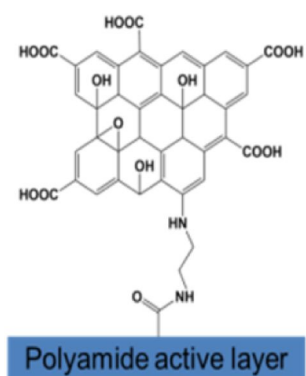


Figure II-6. Schematic illustration of GO-layered membrane. GO nanosheets and aminated GO nanosheets were deposited alternately, and cross-link formed between them (Choi, Choi et al. 2013).



**Figure II-7. Schematic illustration of GO-layered membrane. GO nanosheets formed covalent bonding with membrane surface via cross-linker (Perreault, Tousley et al. 2013).**

### **II.1.5. The shape of the graphene and graphene oxide nanosheets on a substrate**

Graphene and GO nanosheets place on a substrate transversely whether a substrate is taken out from the solution (Yang, Yang et al. 2014) or the solution drop on a substrate (Yang, Chang et al. 2010) because of Langmuir-Blodgett theory (Yang, Yang et al. 2014) or their planar shape (Yang, Chang et al. 2010), respectively. In addition, graphene and GO nanosheets on a substrate are wrinkled, folded, and stacked as shown in Figure II-8 (Yang, Chang et al. 2010). Wrinkling is characteristic feature of graphene and GO nanosheets as shown in Figure II-9 (Pandey, Reifemberger et al. 2008, Chae, Gunes, 2009, Yang, Chang et al. 2010, Calado, Schneider et al. 2012, Gao, Ren et al. 2012). Folding of graphene and GO nanosheets appear with large size of them (Pandey, Reifemberger et al. 2008, Dreyer, Park, et al. 2009, Yang, Chang et al. 2010). Stacking between boundaries of each other graphene and GO nanosheets is occurred when they was aggregated at high concentration of them (Dreyer, Park, et al. 2009, Yang, Chang et al. 2010, Diez-Betriu, Mompean et al. 2014).

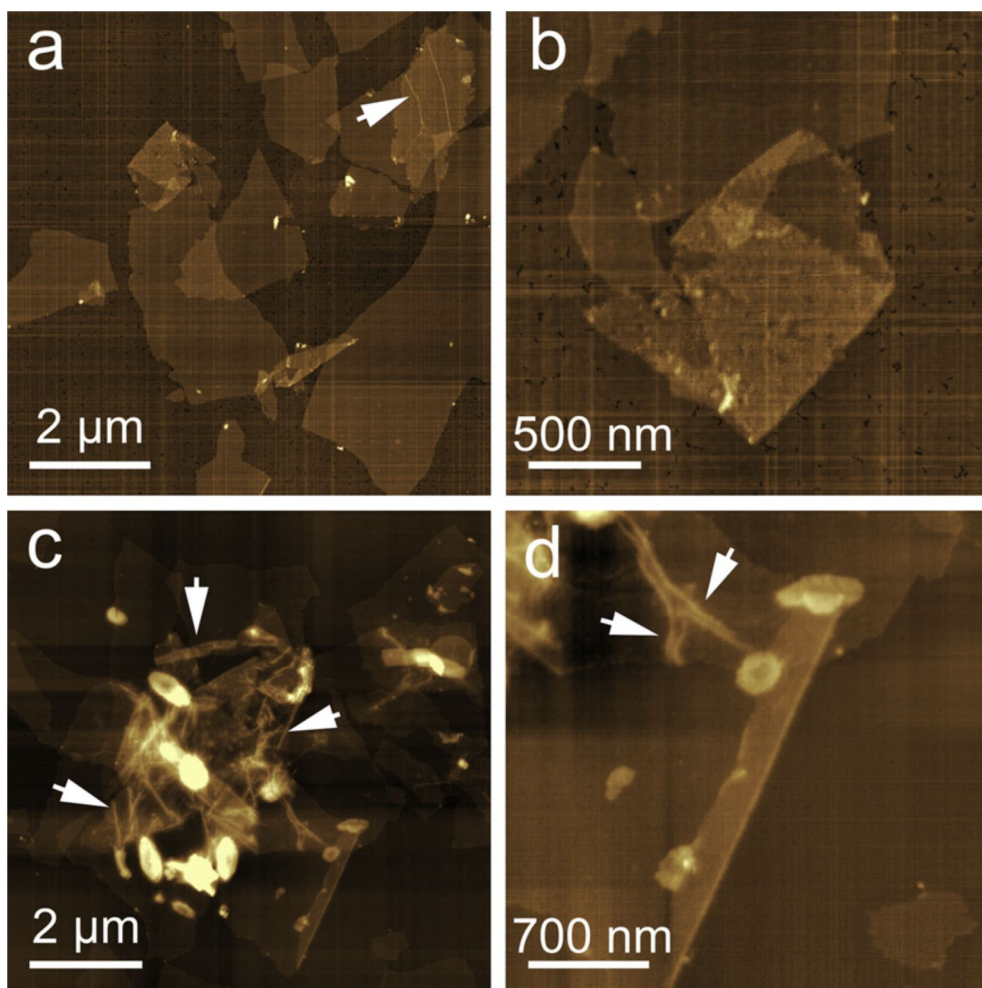


**Figure II-8. AFM images of GO nanosheets on a substrate. GO nanosheets were (a),(b) folded and stacked, or (c),(d) winkled. The bright spots in (c) and (d) is  $\text{Cu}^{2+}$  particles (Yang, Chang et al. 2010).**

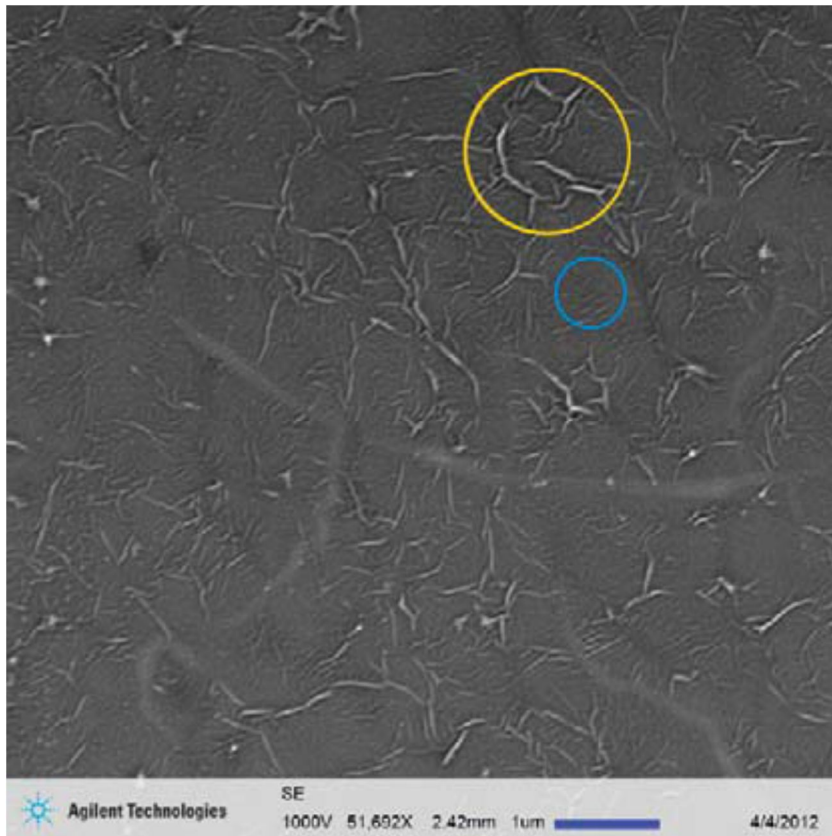


**Figure II-9. A SEM image of GO nanosheets on a substrate.**

**There are many wrinkles, especially indicated as the circles (Xie, Spallas 2012).**

## **II.2. Phase separation for water treatment membrane**

### **II.2.1. Introduction**

A water treatment membrane can be fabricated via several preparation methods such as phase separation, interfacial polymerization, electro-spinning, layer-by-layer deposition, stretching, track-etching, solution casting, and solution wet-spinning. The phase separation, interfacial polymerization are the most common methods among them (Lalia, Kochkodan et al. 2013). A membrane is classified based on its pore size as microfiltration (MF), ultrafiltration (UF), nanofiltration (NF), and reverse osmosis (RO) membranes as shown in Figure II-10 (Lalia, Kochkodan et al. 2013). MF and UF membranes of which pore size is relatively larger are commonly prepared via phase separation with a homogeneous polymer solution whereas NF and RO membranes of which pore size is relatively smaller are usually fabricated via interfacial polymerization. The classification of a water treatment membrane, preparation methods, and commonly used materials were summarized in Table II-2 (Lalia, Kochkodan et al. 2013).

The phase separation is easy (Kools 1998) and economic feasibility (Baker 2004). Therefore, it is widely used to fabricate membrane (Lalia, Kochkodan et al. 2013). A polymer which is dissolved in organic solvent changes in solid phase when the solution is immersed in aqueous non-solvent due to low solubility of a polymer in aqueous solvent (Strathmann and Kock 1977, Strathmann 1985). In detail, instantaneous distribution of polymer molecules is not uniform whereas

polymer molecules uniformly distributed. After starting phase separation, the regions of which polymer concentration are very high converts to solid polymer particle. The polymer particle grow up while concentration of polymer-poor phase decrease via Ostwald ripening (Shaw 1994) Consequently, polymer-rich phase and polymer-poor phase change into polymer membrane structure and membrane pores (Strathmann and Kock 1977, Strathmann 1985). The properties and morphology are controlled by thermodynamic and kinetic parameters such as the chemical potential, solubility, miscibility, diffusivity, Gibbs free energy of mixing (Strathmann and Kock 1977, Strathmann 1985).

Nowadays, several phase separation methods was developed such as non-solvent induced phase separation (NIPS) (Mulder 1996), vapor induced phase separation (VIPS) (Lloyd 1985), evaporation induced phase separation (EIPS) (Strathmann and Kock 1977, Strathmann 1985), and thermally induced phase separation (TIPS) (Lalia, Kochkodan et al. 2013). Those methods use other factors to induce phase separation whereas all of those proceed via similar mechanism. Those methods were explained in detail (Table II-3).

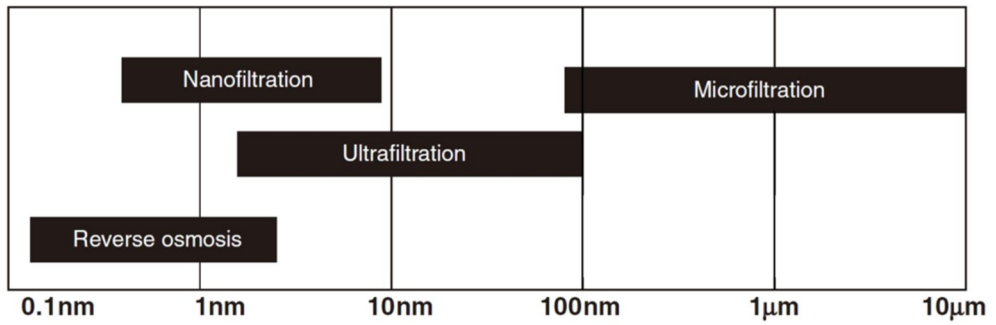


**Figure II-10. Classification of water treatment membrane based on membrane pore size (Lalia, Kochkodan et al. 2013).**

**Table II-2. Summary of the classification of a water treatment membrane, preparation methods, and commonly used materials were summarized (Lalia, Kochkodan et al. 2013).**

Membrane classification	Commonly used materials	Preparation methods
MF (0.1–10 $\mu\text{m}$ )	PVDF	Phase separation
	PTFE	Stretching
	Polypropylene (PP)	Track-etching
	Polyethylene (PE)	
UF (1–100 nm)	PES	
	PSf	Phase separation
	PVDF	Solution wet-spinning
	Polyacrylonitrile (PAN)	
NF (1–10 nm)	PA	Interfacial polymerization
	PSf	Layer-by-layer deposition
	Polyols	Phase separation
	Polyphenols	
RO (3–5 $\text{\AA}$ )	Cellulose acetate	Interfacial polymerization
	Aromatic PA	Layer-by-layer deposition
	Polypiperzine	Phase separation
	Polybenziimidazoline	Solution casting

PTFE: Poly(tetrafluorethylene)

**Table II-3. The features of various phase separation methods (Mulder 1996, Lloyd 1985, Strathmann and Kock 1977, Strathmann 1985, Lalia, Kochkodan et al. 2013).**

Phase separation methods	Composition of polymer solution	Factor inducing phase separation
NIPS	Polymer, Miscible organic solvent	Decrease of solubility with increasing the amount of immiscible non-solvent
VIPS	Polymer, Miscible organic solvent	Decrease of solubility with increasing the amount of immiscible non-solvent as vapor form
EIPS	Polymer, Miscible organic solvent, Immiscible aqueous solvent	Decrease of solubility with decreasing the amount of miscible organic solvent via evaporation
TIPS	Excessive polymer, Miscible organic solvent (At high temperature)	Decrease of excessive solubility with decreasing temperature

## **II.2.2. Nonsolvent induced phase separation method to prepare water treatment membrane**

Among the phase separation methods, NIPS has been the most widely used to prepare a lab-scale membrane because NIPS method is quite easy to make a membrane and control membrane properties at low cost whereas TIPS has been commonly used to fabricate a commercial membrane for high quality via TIPS (Mulder 1996, Baker 2004, Rajabzadeh, Maruyama et al. 2008, Rajabzadeh, Maruyama et al. 2009). The procedure of NIPS is as follows (Mulder 1996, Baker 2004, Witte, Dijkstra et al. 1996).

- 1) A polymer solution is casted on a support layer (ex. non-woven fabric) using a casting knife as shown in Figure II-11 (Baker 2004).
- 2) Casted polymer solution is immersed into a non-solvent (ex. water) to induce phase separation.
- 3) As shown in Figure II-12, solvent of polymer solution and non-solvent is exchanged with each other due to concentration gradient (liquid-liquid demixing).
- 4) After then, a polymer solution membrane stabilizes via rearrangement of polymer structure.

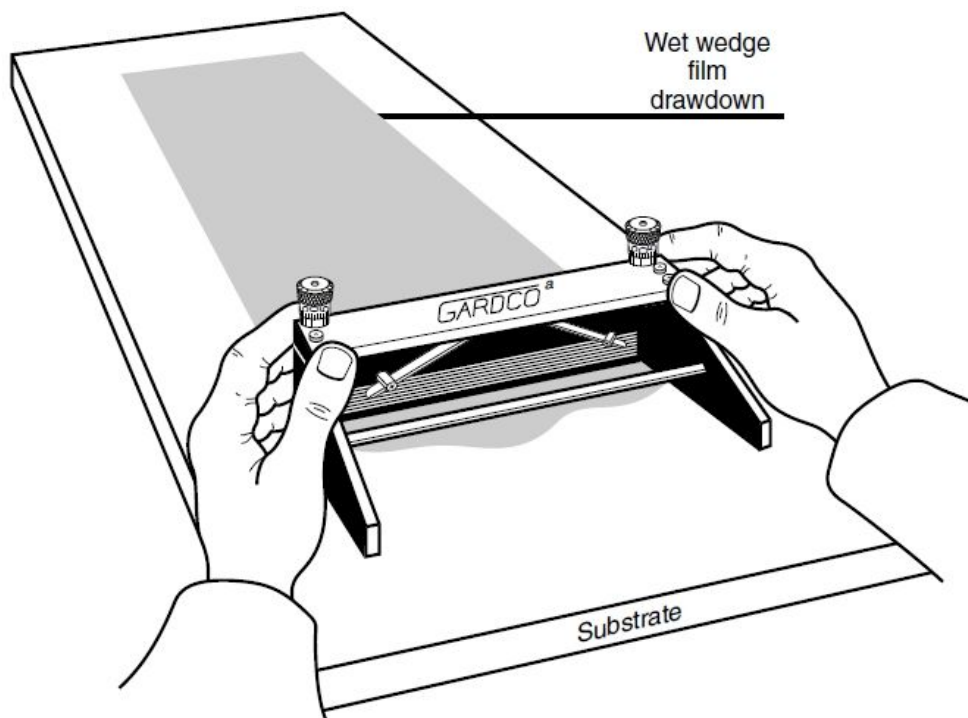


**Figure II-11. Schematic illustration of casting polymer solution (grey region) in a substrate using casting knife (Baker 2004).**

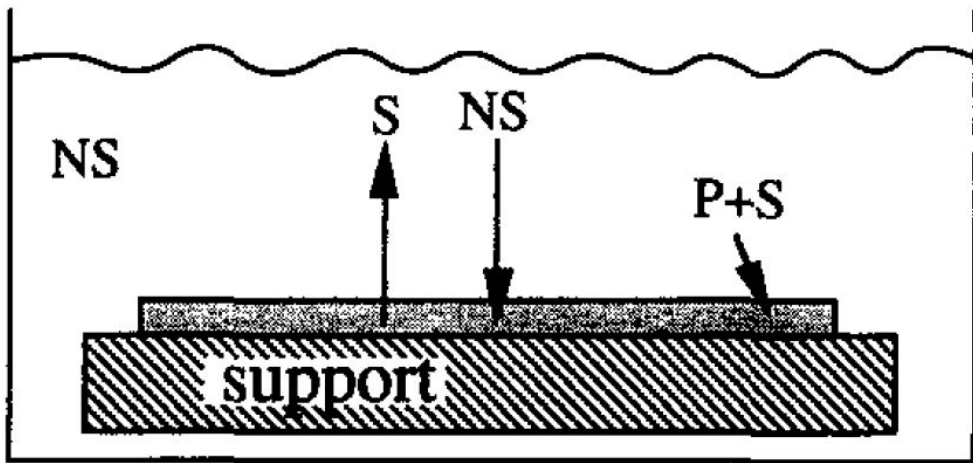


Figure II-12. Schematic illustration of liquid-liquid demixing, a part of NIPS.

P: polymer, S: solvent, NS: non-solvent (Witte, Dijkstra et al. 1996).

The properties of a polymeric membrane fabricated by NIPS are controlled by thermodynamic and kinetic factors. Above all, pore size of a polymeric membrane is determined by the ratio of solvent diffusion flux ( $J_s$ ) to non-solvent diffusion flux ( $J_{ns}$ ) (Lalia, Kochkodan et al. 2013). In detail, pore size of a membrane become 1–30 nm as UF membrane at the ratio ( $J_s/J_{ns}$ )  $\gg 1$  whereas become 200–500 nm as MF membrane at the ratio ( $J_s/J_{ns}$ )  $\approx 1$  because the high ratio ( $J_s/J_{ns}$ ) imply that the concentrations of solvent and non-solvent are quite low and that of polymer is quite high. The solvent diffusion flux ( $J_s$ ) and non-solvent diffusion flux ( $J_{ns}$ ) can be altered by change of temperature and addition of additives (Lalia, Kochkodan et al. 2013).

The phase diagram (Figure II-13) of the three-component (polymer, solvent, and non-solvent) indicates the state of polymer solution and the pathway of phase separation in more detail (Strathmann 1985, Mulder 1996, Baker 2004). Firstly, a composition of polymer solution is one of the factors which determine membrane characteristics. The composition of polymer solution comprised of 25 wt% of polymer and 75 wt% of solvent in Figure II-13 determines the membrane composition. When the concentration of polymer in polymer solution is increased, the concentration of polymer in membrane is also raised and the point B moves toward B'.

When the polymer solution of which composition is A is immersed non-solvent, the composition point moves toward C. That means that non-solvent soaks into the polymer solution (system). Eventually the polymer solution phase

separates into a polymer-rich phase and a polymer-poor phase at C in Figure II-13. Then the composition of a polymer-rich phase moves toward D' and B', and that of a polymer-poor phase proceeds along the curved line toward D" and B", and that of total solution goes toward B and D. The pathway can be altered by change of temperature and addition of additives. Then, composition and morphology of a membrane are changed (Strathmann 1985, Mulder 1996, Baker 2004).

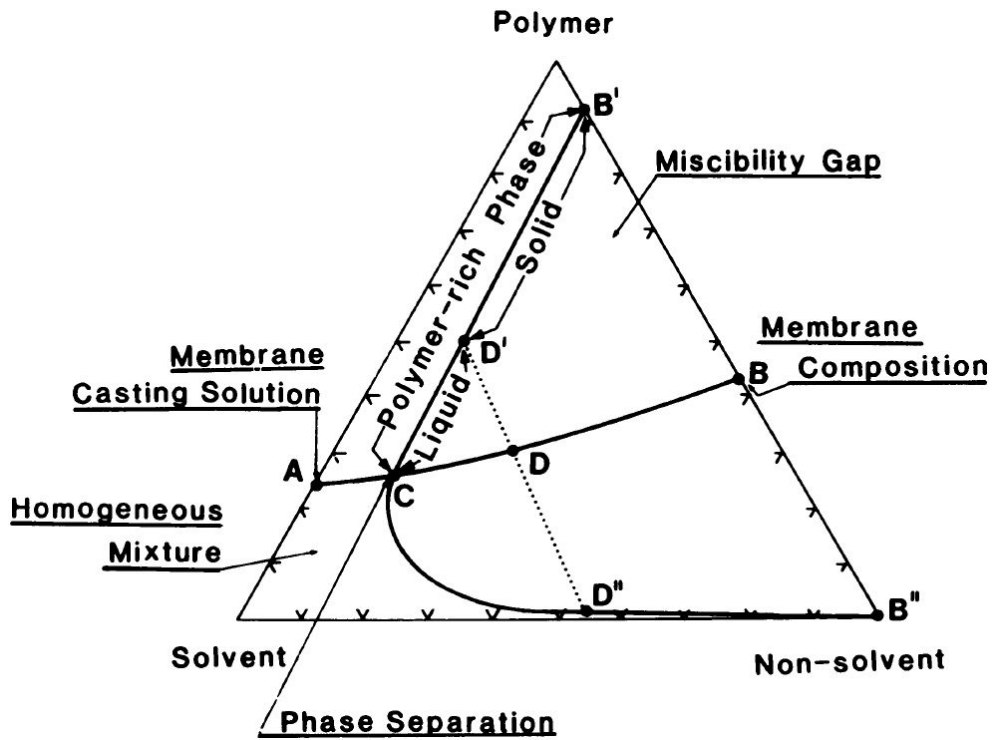


Figure II-13. The phase diagram of the three-component mixture. NIPS proceeds along the line A-B (Lloyd 1985).

### **II.2.3. Interior structures of a membrane prepared by NIPS**

A membrane has two types of interior structures of a membrane, finger- and sponge-like structures as shown in Figure II-14 (Lloyd 1985). The finger-like structure is made up of microvoid region and macrovoid region whereas sponge-like structure consists of small microvoid which is uniformly distributed. The macrovoids which have elongated shape such as finger is randomly distributed. The interior structure of a membrane is determined by demixing rate (Lloyd 1985, Mulder 1996).

The finger-like structure is formed via rapid solidification of a polymer-rich phase caused by rapid demixing between solvent and non-solvent. The demixing rate increases with high temperature, miscibility and activity gradient between the solvent and non-solvent and low viscosity of them. The just solidified polymer has many fractures and much stress because the polymer randomly solidified. However, the stress cannot be released and the fractures cannot be rearranged when the solidification too rapidly progresses as shown in Figure II-15a (Lloyd 1985). Then non-solvent flows in polymer solution through the fracture points and the flow becomes faster because other region except the fracture points is blocked. The quickened flow makes and enlarges macrovoids (Figure II-15b and c). However, the fracture points cannot enlarge because the skin layer already solidified. Consequently, (bottle- or) finger-like structure is formed (Lloyd 1985, Mulder 1996).

On the contrary, the sponge-like structure is formed via relatively slow solidification of a polymer-rich phase. The slow solidification is caused by high miscibility between polymer or non-solvent or slow demixing between solvent and non-solvent. The dense skin layer of the sponge-like structure membrane also has a lot of fractures and stress at early stage. However, in this case, there is enough time to alleviate the fractures and stress. Therefore, small size pores are formed and well distributed. Then, non-solvent slowly flows in polymer solution and size of voids decreases. As the result, sponge-like structure membrane is prepared.

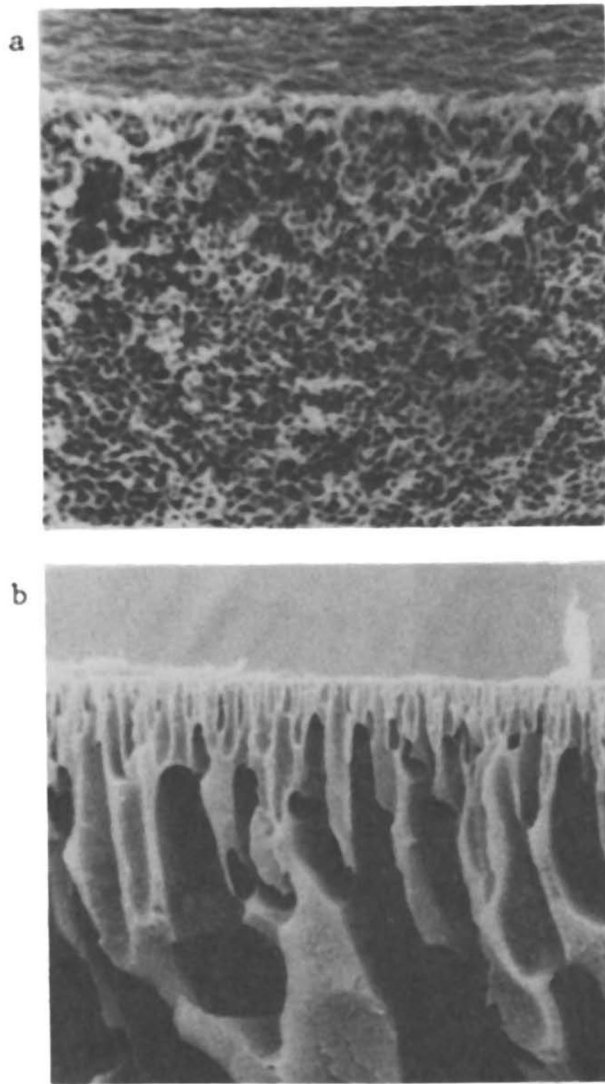


**Figure II-14. (a) The sponge-like structure membrane and (b) the finger-like structure membrane (Lloyd 1985).**

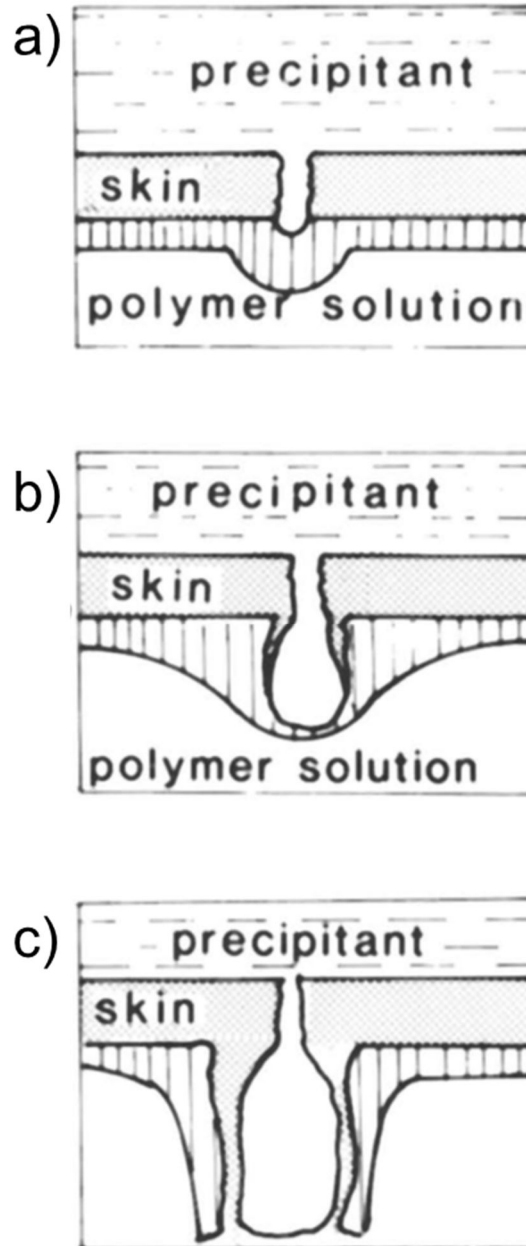


Figure II-15. (a) The early, (b) middle, and (c) late formation stages of the finger-like structure membrane (Lloyd 1985). Precipitant is a synonym of the non-solvent.

## **II.2.4. Control factors for membrane interior structure at NIPS method**

As mentioned in the above two sections, membrane interior structure prepared by NIPs can change depending on kinetic parameters. It was reported that membrane interior structure can be controlled by adjusting Temperature, polymer concentration, activities of polymer, solvent, and non-solvent, or miscibility between them. In other researches, membrane interior structure was controlled using additives (Lloyd 1985, Mulder 1996, Smolders, Reuvers et al. 1992, Zheng, Wang et al. 2006, Amirilargani, Saljoughi et al. 2010, Lalia, Kochkodan et al. 2013).

### **II.2.4.1. The effect of polymer, solvent, and non-solvent set on the membrane structure**

First of all, activities of polymer, solvent, and non-solvent are important in phase separation because activities of them determines membrane properties and membrane structure as shown in Figure II-16 (Lloyd 1985). However, it is difficult to obtain the activity coefficients of them and the relationship between these activity coefficients on creation composition. Therefore, the dependence between polymer and solvent can be roughly estimated based on the disparity between the solubility parameters of them (Lloyd 1985). For example, the smaller solubility

parameters disparity of them, the better compatibility between them. Then, demixing rate lowers and membrane interior structure becomes more like sponge-like structure. Likewise, higher solubility parameters disparities between solvent and non-solvent or between polymer and non-solvent induce slow demixing. Then, membrane interior structure also changes more like sponge-like structure (Lloyd 1985). In addition, the miscibility between solvent and non-solvent can be also examined via evaluating the heat of mixing of a solvent and non-solvent (Lloyd 1985). The smaller heat of mixing implies that the mixing is less favorable, and then sponge-like structure is formed (Strathmann and Kock 1977, Lloyd 1985).

In detail, more polar organic solvents such as NMP, DMA, DMF, and dimethyl sulfoxide (DMSO) which are more miscible and more able to make hydrogen bonding with aqueous non-solvent induce rapid demixing and finger-like structure. Therefore, they are widely used to prepare highly porous membrane (Lalia, Kochkodan et al. 2013). Besides, affinity between polymer and solvent also affect to membrane interior structure although demixing rate between solvent and non-solvent is equal. For instance, NMP which has higher affinity with PSf than DMF slowly diffuses from casting solution during phase separation compared with DMF (Hansen 2007, Tiraferri, Yip et al. 2011). As the result, influx of non-solvent into the casting solution becomes faster using NMP as solvent than DMF, and a larger amount of non-solvent penetrates into the casting solution. Consequently, NMP and DMF induce finger- and sponge-like structure with PSf, respectively.

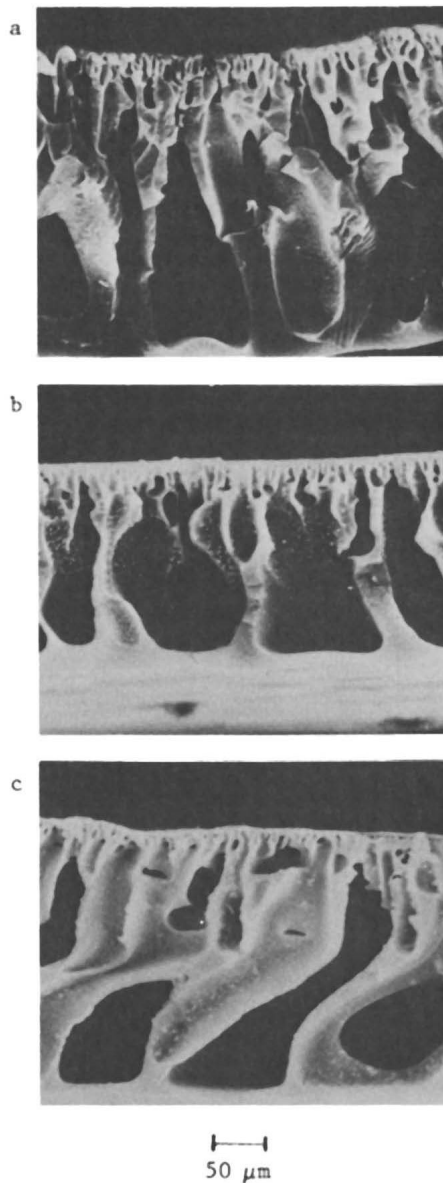


**Figure II-16. The SEM images of the membrane with cross-sectional view. a) 12 % cellulose acetate in DMAc b) 12 % polyamide in DMSO, c) 12 % polysulfone in DMF. The SEM images shows effect of polymer and solvent set on membrane interior structure (Lloyd 1985).**

#### **II.2.4.2. The effect of polymer concentration in polymer solution on the membrane structure**

The polymer concentration of polymer solution is also one of major determinant factors for membrane structure. When the polymer concentration is decreased during NIPS, membrane pore size is increased and membrane interior structure changes toward sponge-like structure as shown in Figure II-17 and II-18 (Lloyd 1985, Misdan, Lau, et al. 2013, Ding, Yin et al. 2014).

The polymer concentration affects to polymer concentration via two ways. One is change in the composition of polymer solution and polymer membrane. As shown in Figure II-13 and aforementioned, when the polymer concentration in a polymer solution is increased, the fraction of polymer-rich phase in a membrane is also raised. That means that the fraction of polymer-poor phase which will convert to pore is small. Consequently, the porosity (fraction of pores) is also reduced and the number and size of macrovoid also decreased because the fraction of fracture which is precursor of pore is declined (Lloyd 1985, Misdan, Lau, et al. 2013, Ding, Yin et al. 2014). The other one is change in the viscosity of polymer solution. When polymer solution is very viscous, solvent is hard to move out from polymer solution and non-solvent is also difficult to move in to polymer solution. In other words, the demixing rate lowers. Therefore, there is enough time to rearrange fractures. Then, the fractures which are precursors of pores distribute well and be smaller. Then, the sizes of pores and macrovoids become smaller (Lloyd 1985, Misdan, Lau, et al. 2013, Ding, Yin et al. 2014).

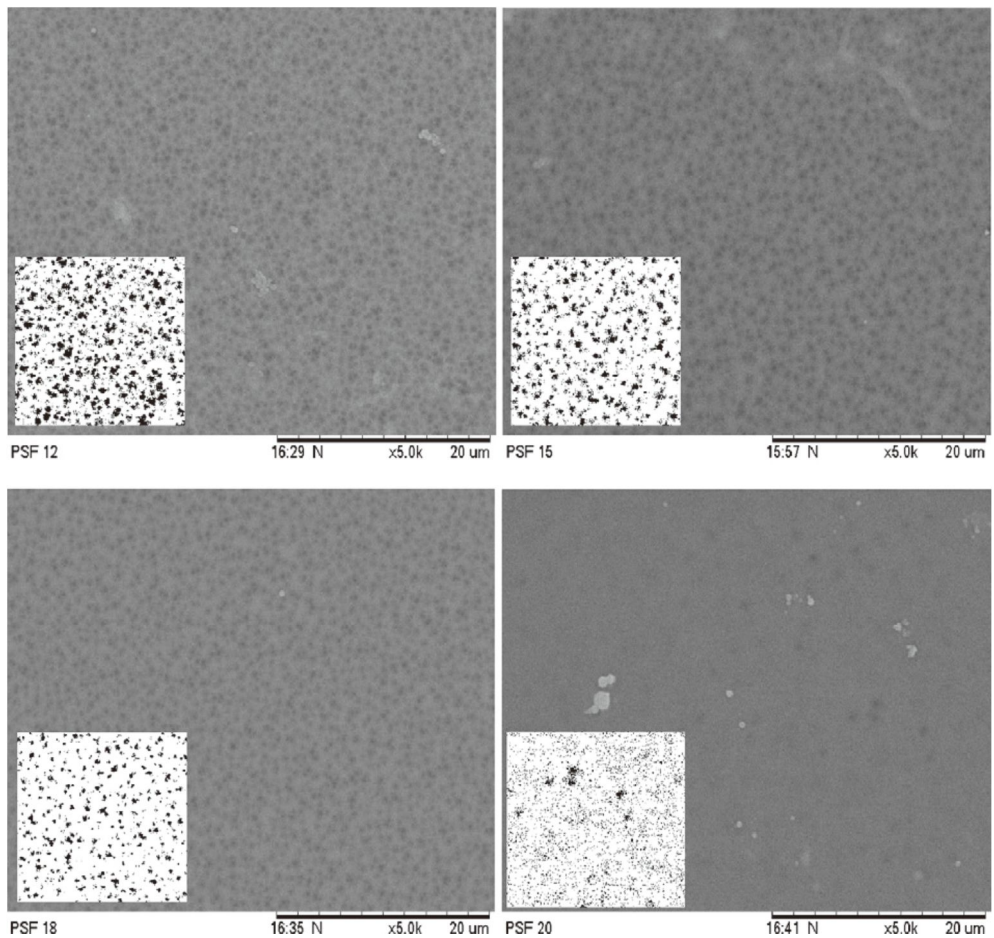


**Figure II-17. The SEM images of the membrane with top view. The surface pore size of the membrane was decreased with increasing polymer concentration. The number under the lower left-handed corner of each image represents the polymer concentration of PSf in NMP (Misdan, Lau, et al. 2013).**

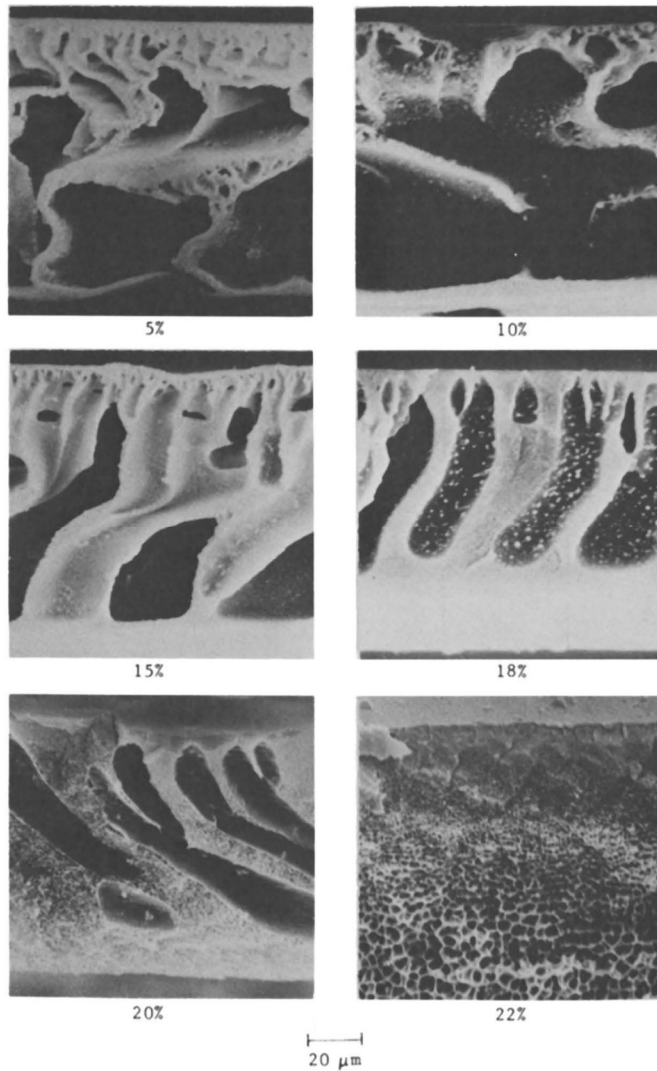


**Figure II-18. The SEM images of the membrane with cross-sectional view. The macrovoid size of the membrane was decreased with increasing polymer concentration. In other words, the membrane interior structure changed from finger-like structure to sponge-like structure with increasing polymer concentration. The number under each image represents the polymer concentration of PA in NMP (Lloyd 1985).**

### **II.2.4.3. The effect of additives on the membrane structure**

Various additives were applied to the NIPS membrane to enhance membrane properties such as its pore size, porosity, water permeability, anti-biofouling property. Firstly, several functional particles such as LiCl, poly(vinylpyrrolidone) (PVP), or polyethylene glycol (PEG) were widely used to improve properties, characteristics, and structure of NIPS membrane. Then, hydrophilicity and water flux were enhanced and the membrane interior structure was changed as shown in Figure II-19 (Lee, Won et al. 2002, Marchese, Ponce et al. 2003, Fontananova, Jansen et al. 2006, Arthanareeswaran, Thanikaivelan et al. 2007, Wang, Yu et al. 2009, Lafreniere, Talbot et al. 1987, Chuang, Young et al. 2000). Secondly, hydrophilic nanoparticles such as TiO<sub>2</sub>, zeolite, silver nanoparticles, functionalized carbon nanotube (CNT), or GO nanosheets were also adapted to NIPS membrane. Then, hydrophilicity of the NIPS membrane was quite increased. As the result, water permeability and anti-biofouling property were significantly ameliorated (Choi, Jegal et al. 2006, Yang, Zhang et al. 2007, Zodrow, Brunet et al. 2009, Haiyang, Shi et al. 2013, Shi, Liu et al. 2013).

Finally, solvent additive was used to control pore size of membrane interior structure. For example, pore size of membrane is reduced when solvent or solvent miscible liquid are added in non-solvent. The cause of the results is that  $J_s$  decreases due to decline concentration of solvent  $J_{ns}$  do not change and extraction of polymer is impeded (Lloyd 1985).

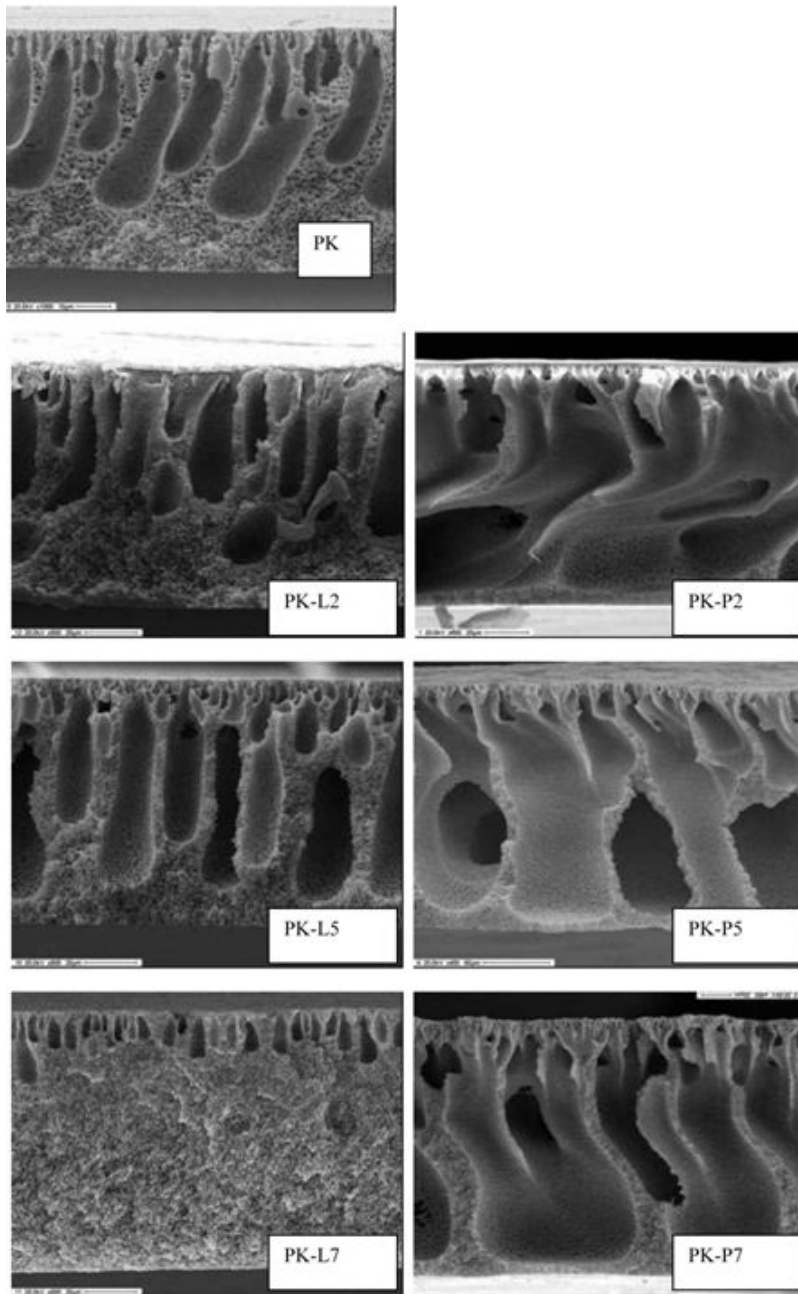


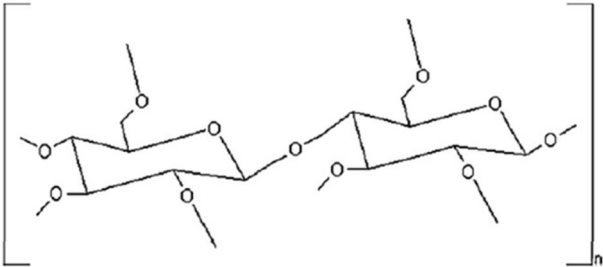
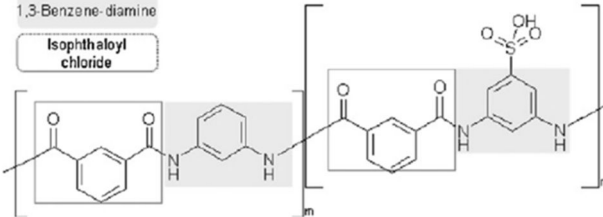
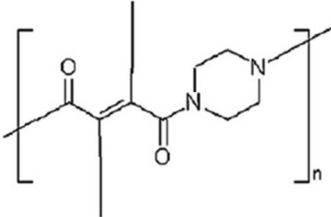
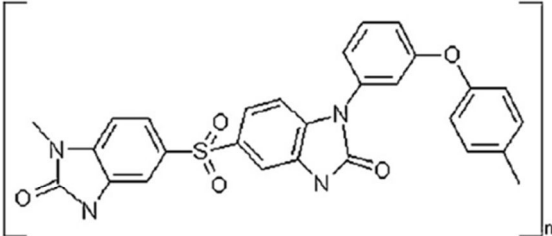
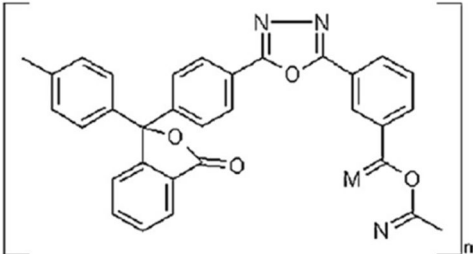
**Figure II-19. The SEM images of the membrane with cross-sectional view increasing concentration of LiCl (left) and PVP (right) in the casting solution (Fontananova, Jansen et al. 2006).**

## **II.3. Interfacial polymerization for reverse osmosis membrane**

### **II.3.1. Introduction**

In 1949, salt-rejecting membrane was reported as early-stage reverse osmosis (RO) membrane by G.L. Hassler. In 1959, hand-cast thin symmetric cellulose acetate (CA) membrane was reported by Reid and Breton. The symmetric CA membrane achieved high salt rejection of 98%. However, its water flux ( $0.01 \text{ L m}^{-2} \text{ h}^{-1}$ ) was too low to use for industrial (Lee, Arnot et al. 2011). Then, asymmetric CA membrane was developed by Loeb and Sourirajan in 1963 (Loeb and Sourirajan 1963). The asymmetric CA membrane exhibited appropriate water permeability and salt rejection for industrial RO membrane as shown in Table II-4. The performance and chemical structure of asymmetric RO membranes including the asymmetric CA membrane were listed in Table II-4 (Lee, Arnot et al. 2011). However, the asymmetric CA membrane has disadvantage to a long-term RO process. When CA membrane is pressed for a long time, the membrane is compacted and densified. Then its water permeability is dramatically decreased. Another shortage is that only few polymer is available to asymmetric membrane (Congjie 2003).

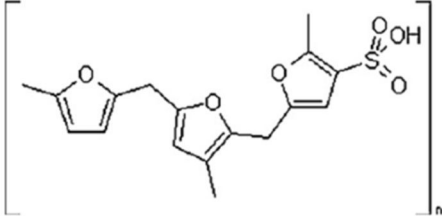
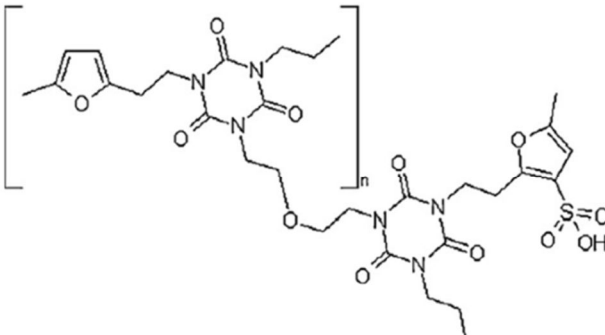
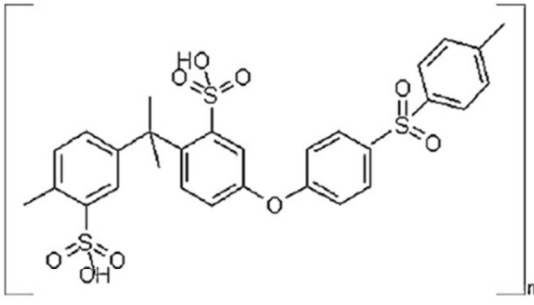
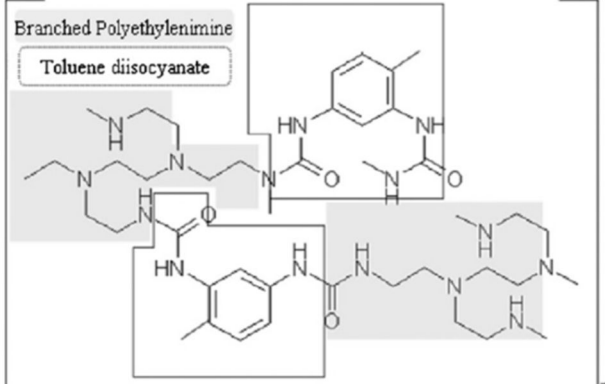
**Table II-4. The performance and chemical structure of asymmetric RO membranes (Lee, Arnot et al. 2011).**

Chemical type & description	Chemical structure
<p>1. Cellulose Acetate - Loeb-Sourirajan CA                      Flux: <math>0.35 \text{ m}^3 \text{ m}^{-2} \text{ day}^{-1}</math>                      Salt rejection: 99%                      Test: &gt; 100 bar, 4% NaCl solution</p>	 <p>The structure shows a repeating unit of cellulose acetate, consisting of two glucose rings linked by an oxygen atom. Each glucose ring has several hydroxyl groups replaced by acetyl groups (-O-C(=O)-CH<sub>3</sub>).</p>
<p>2. Aromatic Polyamide - Polyamide-hydrazide                      Flux: <math>0.67 \text{ m}^3 \text{ m}^{-2} \text{ day}^{-1}</math>                      Salt rejection: 99.5%                      Test: 30 °C, &gt; 100 bar, 3.5% NaCl solution</p>	<p>1,3-Benzene-diamine                      Isophthaloyl chloride</p>  <p>The structure shows a repeating unit of an aromatic polyamide-hydrazide. It features a central benzene ring with two amide groups (-NH-CO-) and a hydrazide group (-NH-CO-NH-CO-) attached. The amide groups are linked to a 1,3-benzenediamine moiety, and the hydrazide group is linked to an isophthaloyl chloride moiety.</p>
<p>3. Polypiperazine-amide                      Flux: <math>0.67 \text{ m}^3 \text{ m}^{-2} \text{ day}^{-1}</math>                      Salt rejection: 97.2%                      Test: &gt; 80 bar, 0.36% NaCl solution</p>	 <p>The structure shows a repeating unit of a polypiperazine-amide. It features a central piperazine ring (a six-membered ring with two nitrogen atoms) linked to an amide group (-NH-CO-). The amide group is further linked to a carbonyl group (-C(=O)-) which is part of a larger chain.</p>
<p>4. Polybenzimidazole                      Flux: <math>0.13 \text{ m}^3 \text{ m}^{-2} \text{ day}^{-1}</math>                      Salt Rejection: 95%                      Test: &gt; 6 bar, 0.105% NaCl solution</p>	 <p>The structure shows a repeating unit of a polybenzimidazole. It features a central benzimidazole ring system (a benzene ring fused to an imidazole ring) linked to a sulfonamide group (-SO<sub>2</sub>-NH-). The sulfonamide group is further linked to a benzene ring, which is then linked to another benzimidazole ring system.</p>
<p>5. Polyoxadiazole                      Flux: <math>0.07 \text{ m}^3 \text{ m}^{-2} \text{ day}^{-1}</math>                      Salt Rejection: 92%                      Test: &gt; 45 bar, 0.5% NaCl solution</p>	 <p>The structure shows a repeating unit of a polyoxadiazole. It features a central oxadiazole ring system (a five-membered ring with two nitrogen atoms and one oxygen atom) linked to a carbonyl group (-C(=O)-). The carbonyl group is further linked to a benzene ring, which is then linked to another oxadiazole ring system.</p>

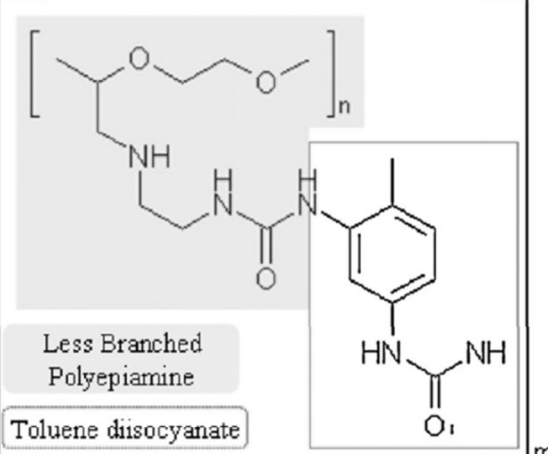
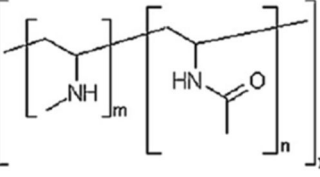
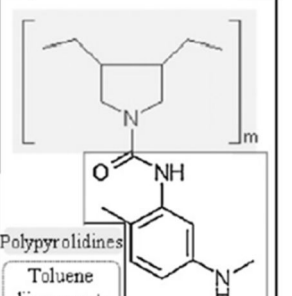
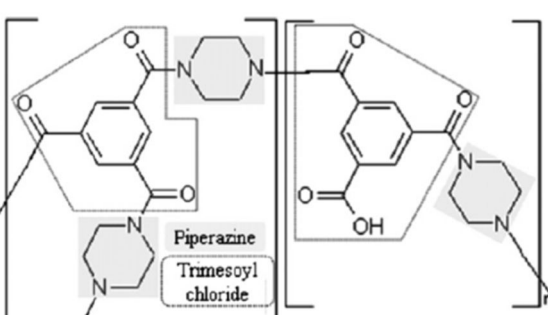
For these reasons, the porous layer and dense layer of the RO membrane was prepared separately. The porous layer is thick and mechanically strong whereas the dense layer is thin. A role of the porous layer is support dense layer, and dense layer plays a role as filtration media. Therefore, the whole membrane, porous layer, and dense layer are named as thin-film composite (TFC) membrane, support, and active layers, respectively (Lee, Arnot et al. 2011). The performance and chemical structure of TFC RO membranes were listed in Table II-5 (Lee, Arnot et al. 2011). The first TFC membrane was fabricated by lamination of CA thin-film layer by float-casting on a CA porous support layer and subsequent annealing. However, the float-casting method is quite difficult and is unsuitable to mass production (Francis 1966). Consequently, more readily dip-coating method was invented to substitute for the float-casting method (Riley, Lonsdale et al. 1971, Kirsh and Popkov 1988). The reaction of furfural alcohol, sulphuric acid and polyoxyethylene (or 1, 3, 5-tris(hydroxyethyl) isocyanuric acid) was used for the dip-coating method as shown in Table II-5 (Lee, Arnot et al. 2011). The membranes prepared by the dip-coating method exhibited excellent salt rejection but were vulnerable to irreversible swelling, hydrolysis of sulphate linkage, or chlorine attack (Lee, Arnot et al. 2011). In other studies, active layer was formed via plasma or atomic polymerizations. However, the membrane fabricated by the methods has poor chemical durability such as low chlorine resistance (Lee, Arnot et al. 2011).

**Table II-5. The performance and chemical structure of TFC RO membranes**

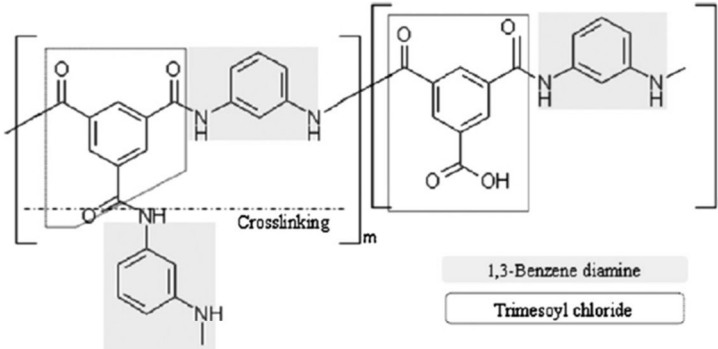
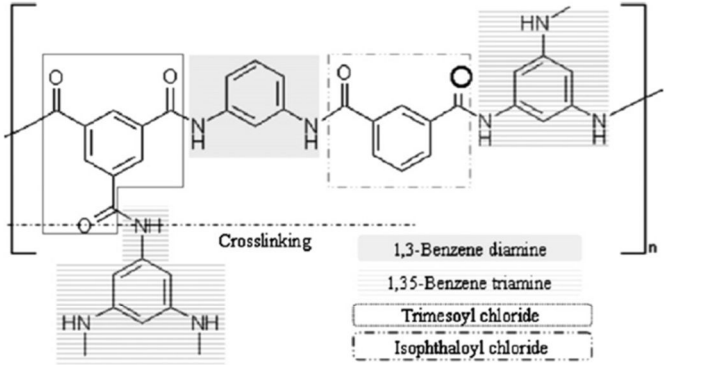
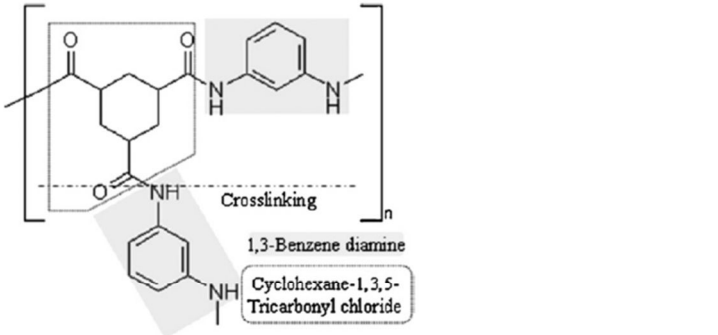
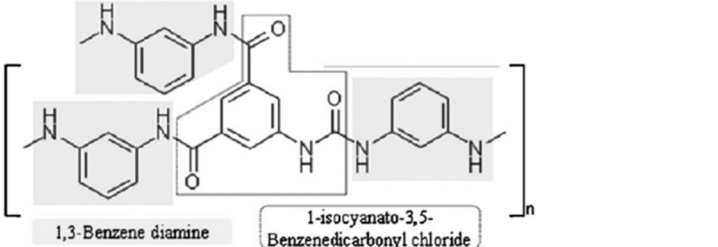
(Lee, Arnot et al. 2011).

Chemical type & description	Chemical structure
<p>1. Polyfurane - Name: NS-200                      Flux: <math>0.8 \text{ m}^3 \text{ m}^{-2} \text{ day}^{-1}</math>                      Salt Rejection: 99.8%                      Test: &gt; 100 bar, 3.5% NaCl solution</p>	
<p>2. Polyether-Polyfurane - Name: PEC-1000                      Flux: <math>0.5 \text{ m}^3 \text{ m}^{-2} \text{ day}^{-1}</math>                      Salt Rejection: 99.9%                      Test: &gt; 69 bar, 3.5% NaCl solution                      -Excellent organic rejection</p>	
<p>3. Sulfonated Polysulfone - Name: Hi-Flux CP                      Flux: <math>0.06 \text{ m}^3 \text{ m}^{-2} \text{ day}^{-1}</math>                      Salt Rejection: 98%                      Test: &gt; 69 bar, 3.5% NaCl solution                      -Excellent chlorine resistance</p>	
<p>4. Polyamide via polyethylenimine - Name: NS-100                      Flux: <math>0.7 \text{ m}^3 \text{ m}^{-2} \text{ day}^{-1}</math>                      Salt Rejection: 99%                      Test: &gt; 100 bar, 3.5% NaCl solution</p>	 <p>Branched Polyethylenimine                      Toluene diisocyanate</p>

**Table II-5. (continued)**

Chemical type & description	Chemical structure
<p>5. Polyamide via polyepiamine - Name PA-300 or RC-100 Flux: <math>1.0 \text{ m}^3 \text{ m}^{-2} \text{ day}^{-1}</math> Salt Rejection: 99.4% Test: &gt; 69 bar, 3.5% NaCl solution</p>	 <p>Less Branched Polyepiamine</p> <p>Toluene diisocyanate</p>
<p>6. Polyvinylamine - Name: WFX-X006 Flux: <math>2.0 \text{ m}^3 \text{ m}^{-2} \text{ day}^{-1}</math> Salt Rejection: 98.7% Test: &gt; 40 bar, Conductivity = <math>5000 \mu\text{S cm}^{-1}</math></p>	
<p>7. Polypyrrolidine Flux: <math>0.8 \text{ m}^3 \text{ m}^{-2} \text{ day}^{-1}</math> Salt Rejection: 99.7% Test: &gt; 40 bar, 0.5% NaCl solution</p>	 <p>Polypyrrolidines</p> <p>Toluene diisocyanate</p>
<p>8. Polypiperazine-amide - Name: NS-300 Flux: <math>3.3 \text{ m}^3 \text{ m}^{-2} \text{ day}^{-1}</math> Salt Rejection: 68% Test: &gt; 100 bar, 3.5% NaCl solution</p>	 <p>Piperazine</p> <p>Trimesoyl chloride</p>

**Table II-5. (continued)**

Chemical type & description	Chemical structure
<p>9. Cross linked Fully Aromatic Polyamide - 1 - Name: FT-30                      Flux: <math>1.0 \text{ m}^3 \text{ m}^{-2} \text{ day}^{-1}</math>                      Salt Rejection: 99%                      Test: &gt; 15 bar, 0.2% NaCl solution</p>	 <p style="text-align: center;">Crosslinking</p> <p style="text-align: right;">1,3-Benzene diamine Trimesoyl chloride</p>
<p>10. Cross linked Fully Aromatic Polyamide - 2 - Name: UTC series                      Flux: <math>0.8 \text{ m}^3 \text{ m}^{-2} \text{ day}^{-1}</math>                      Salt Rejection: 98.5%                      Test: &gt; 15 bar, 0.5% NaCl solution</p>	 <p style="text-align: center;">Crosslinking</p> <p style="text-align: right;">1,3-Benzene diamine 1,3,5-Benzene triamine Trimesoyl chloride Isophthaloyl chloride</p>
<p>11. Cross linked Aralkyl Polyamide - Name: A-15                      Flux: <math>0.26 \text{ m}^3 \text{ m}^{-2} \text{ day}^{-1}</math>                      Salt Rejection: &gt; 98%                      Test: &gt; 55 bar, 3.2% NaCl solution</p>	 <p style="text-align: center;">Crosslinking</p> <p style="text-align: right;">1,3-Benzene diamine Cyclohexane-1,3,5-Tricarboxylic acid</p>
<p>12. Cross linked Fully Aromatic Polyamide - 3 - Name: X-20                      Flux: <math>1 \text{ m}^3 \text{ m}^{-2} \text{ day}^{-1}</math>                      Salt Rejection: 99.3%                      Test: &gt; 15 bar, 0.2% NaCl solution</p>	 <p style="text-align: right;">1,3-Benzene diamine 1-isocyanato-3,5-Benzenedicarbonyl chloride</p>

The first non-cellulosic RO membrane, NS-100, was fabricated by Cadotte via interfacial polymerization between polythylenimine and toluene di-isocyanate (Table II-5). The NS-100 exhibited comparable water permeability and salt rejection as well as thermal and pH stabilities (Cadotte 1977, Bartels 1989, Mysels and Wrasidlo 1991). However, the NS-100 had poor chlorine resistance and was too brittle to endure high pressure (Lee, Arnot et al. 2011). After then, better membrane, PA-300 and RC-100 was developed in late 1970s. The materials of PA-300 and RC-100 are poly(ether/amide) and poly(ether/urea) as shown in Table II-5. PA-300 exhibited water flux of  $1\text{m}^3\text{m}^{-2}\text{d}^{-1}$  and salt rejection of 99.4% at 70 bar (Riley, Milstead et al. 1977, Lee, Arnot et al. 2011). In early 1980s, more improved TFC RO membrane, FT-30, was fabricated via interfacial polymerization between 1,3-benzenediamine (*m*-phenylenediamine; MPD) with trimesoyl chloride (TMC). The FT-30 had outstanding water permeability ( $1\text{m}^3\text{m}^{-2}\text{d}^{-1}$ ) and salt rejection (99.2%) at 55 bar as shown in Table II-5. Moreover, FT-30 had good chlorine resistance and pH stability (Glater, Zachariah et al. 1983, Lee, Arnot et al. 2011).

### **II.3.2. Interfacial polymerization method to prepare thin-film composite reverse osmosis membrane**

Interfacial polymerization (IP) method is the most widely used to prepare TFC RO membrane due to its excellent permselectivity, mechanical strength, chlorine resistance, and pH stability (Petersen 1993, Lau, Ismail et al. 2012). For IP, MPD and TMC, which were also applied to FT-30, are the most commonly used because both polymerization and cross-linking during IP are rapidly proceeded using them even at lower concentration of TMC (Cadotte, Petersen et al. 1980, Koo, Petersen et al. 1986, Lee, Arnot et al. 2011). In addition, the combination of aromatic amines (including MPD) and aromatic acyl halide (including TMC) induces much rough surface via growth of ridges than the surface prepared using aliphatic amines (Porter 1990).

The procedure of IP method is as follows as shown in Figure II-20 (Lee, Arnot et al. 2011, Xie, Geise et al. 2012, Kim, Jeong, et al. 2013). Firstly, a support membrane is immersed in DI water overnight for pore opening (Figure II-20a). If the support membrane stored in DI water is used, this step can be omitted. Secondly, the support membrane is immersed in an aqueous solution containing MPD for 1–10 min (Figure II-20b). During the immersion, MPD diffuse into DI water in the pores of the support membrane. Next, excess MPD aqueous solution is removed by hand roller or automatic roller (Figure II-20c). Sometimes, the support membrane soaked with MPD aqueous solution is additionally dried in air between the step (c) and (d). The support membrane containing MPD solution is immersed

in a solution of TMC in hexane (or dodecane) as shown in Figure II-20d. In this step, interfacial polymerization between MPD and TMC occurs at interface between DI water and hexane (or dodecane). Dodecane which is more hydrophobic than hexane make thinner interface with water, and thinner active layer. As the result, the water permeability of TFC membrane is slightly increased. However, dodecane is very expensive. For this reason, hexane is the most popular solvent for TMC. Subsequently, the residual unreacted TMC solution is removed by flow of hexane to make active layer much thinner (Figure II-20 (f)). However, this step is often omitted because the thickness of active layer can be also controlled by rolling strength or concentration of monomers. Finally, the prepared membrane is stabilized and stored in DI water until use (Figure II-20 (G)).

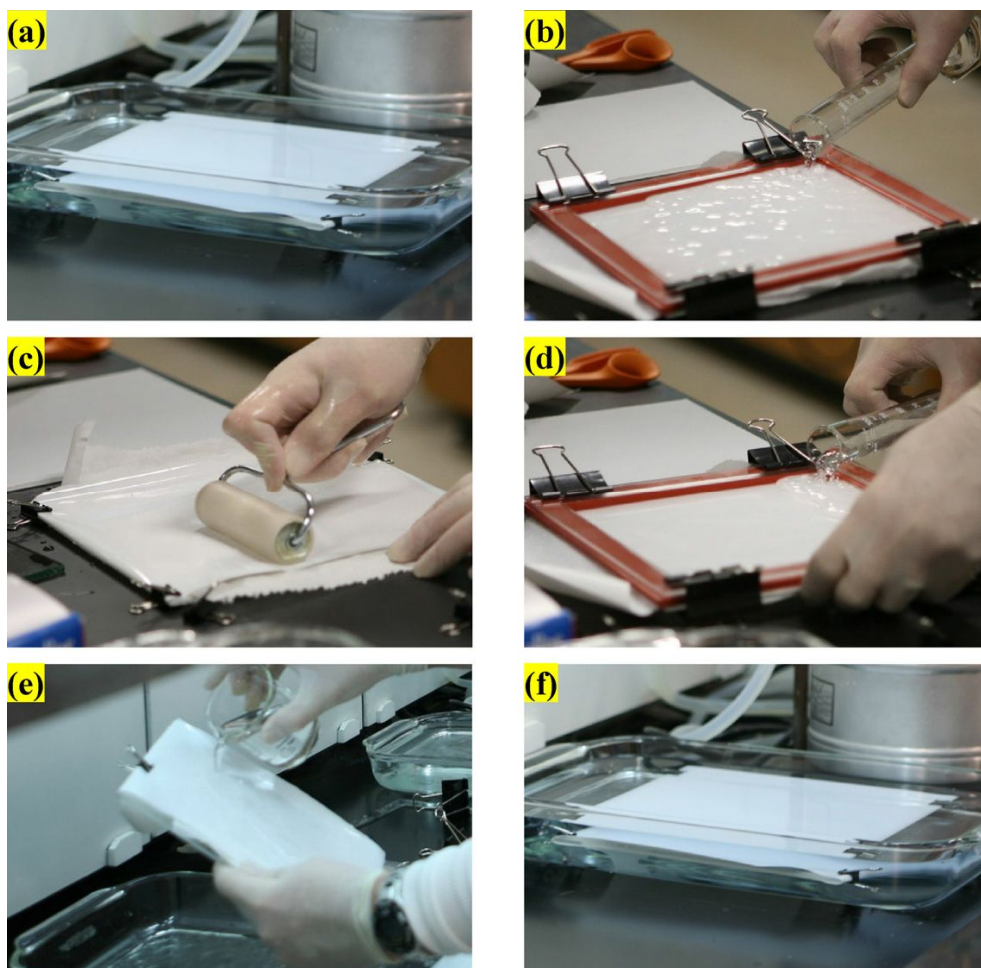


**Figure II-20. The Schematic procedure of the IP. a) Support membrane was immersed in DI water overnight. b) Surface of the support membrane contact an aqueous MPD solution for 10 min c) Aqueous MPD droplets was squeezed from the support membrane with a rubber roller. d) Surface of the support membrane contact a solution of TMC in n-dodecane for 1 min, e) Surface of the support membrane was rinsed with n-hexane. f) The prepared TFC membrane was stabilized and stored in DI water until use (Xie, Geise et al. 2012).**

### **II.3.3. Recent trend of reverse osmosis membrane**

First feasible RO membrane, an asymmetric CA membrane, was invented by the Loeb-Sourirajan in 1962 (Loeb and Sourirajan 1963) and Cadotte developed the TFC RO membrane with comparable flux and salt rejection such by via IP (Cadotte, Petersen et al. 1980). After then, the polyamide TFC RO membrane has been continually improved over the last 30 years. However, it still needs improvement in terms of its permselectivity, anti-biofouling, and chlorine resistance (Clark, Allgeier et al. 1998, Escobar, Hoek et al. 2005). Nowadays, the TFC RO membrane is consistently researched in terms of embedment of additives, surface modification with additives, layer-by-layer (LbL) deposition of additives, carbon nanomaterial based membrane, and support layer.

#### **II.3.3.1. Thin-film nanocomposite membrane**

TFC membrane with nanoparticle (NP) embedded in its active layer, which is called thin-film nanocomposite (TFN) membrane, have attracted much attention and is reported in numerous studies because TFN membrane exhibited outstanding permselectivity, chlorine resistance, anti-biofouling, and mechanical strength due to hydrophilicity and negative charge of NPs. Furthermore, NPs is more suitable to embed in active layer than other additives because very small NPs are more distributed and less aggregated. To prepare TFN membrane, NP is generally dispersed in MPD aqueous solution or TMC organic solution (Kim, Choi, et al.

2014, Jeong, Hoek et al. 2007, Wu, Tang et al. 2010, Zhao, Qiu et al. 2014, Yin, Deng 2015).

TFN membrane embedding hydrophilic and negatively charged zeolite NP was prepared via adding 0.4 w/v% zeolite NP to TMC organic solution. As the result, zeolite NP is successfully embedded in active layer of TFN membrane as shown in Figure II-21 (Jeong, Hoek et al. 2007). Then, the water permeability was approximately 80% improved compared with control TMC membrane maintaining salt rejection due to increment of hydrophilicity and negative surface zeta potential of the membrane (Jeong, Hoek et al. 2007). Similarly TiO<sub>2</sub>, Ag, and SiO<sub>2</sub> NPs were embedded in active layer of TFN RO membranes. TiO<sub>2</sub> NP is added in organic solution whereas Ag and SiO<sub>2</sub> NPs are usually applied to aqueous solution. The NPs enhanced water permeability or anti-biofouling property due to increment of hydrophilicity (Yin, Deng 2015, Lee, Kim et al. 2007, Jadav, Singh 2009).

Carbon nanotube (CNT) is another attractive additive to improve performance of TFN membrane. CNT has no hydrophilic or negative charged functional groups. For this reason, CNT is applied to TFN membrane after functionalization such as oxidation, carboxylation, or aluminosilication (Kim, Choi et al. 2014, Yin, Deng 2015, Wang, Chen et al. 2005, Wu, Tang et al. 2010, Baroña, Choi et al. 2012). After functionalization CNT has numerous functional groups due to its large specific area. The other advantage of CNT different with other NPs is fluid transport channel. It is reported that water much rapidly pass through the channel when water enter in fluid transport channel, inside space of CNT. However, ions

cannot pass through the channel (Corry 2008, Song, Corry 2009). Therefore, embedment of functionalized CNT in active layer of TFN membrane enhances water permeability and salt rejection via hydrophilicity and fluid transport channel as shown in Figure II-22 (Kim, Choi et al. 2014). Depending on the degree of functionalization for CNT, CNT can be added in MPD aqueous solution or TMC organic solution (Kim, Choi et al. 2014, Yin, Deng 2015, Wu, Tang et al. 2010, Baroña, Choi et al. 2012, Zhao, Qiu et al. 2014, Wang, Chen et al. 2005).

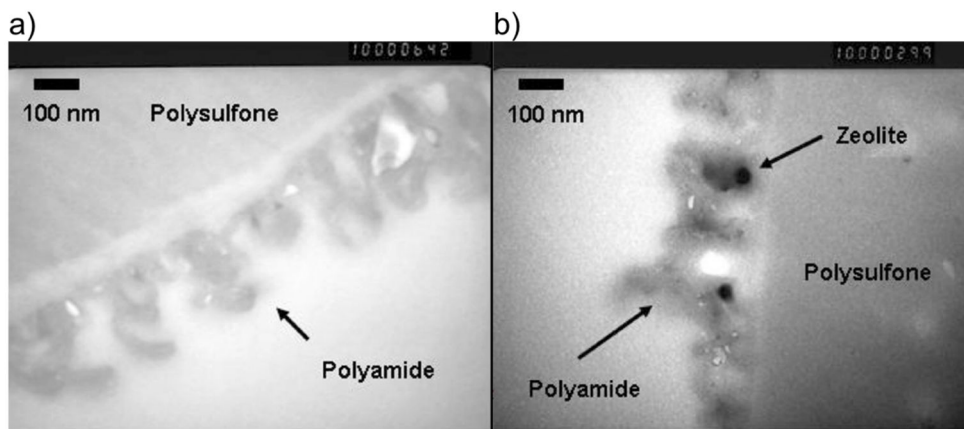


**Figure II-21.** The transmission electron microscopy (TEM) images with cross-sectional view of a) TFC membrane and TFN membrane with zeolite NP embedded in its active layer (Jeong, Hoek et al. 2007).

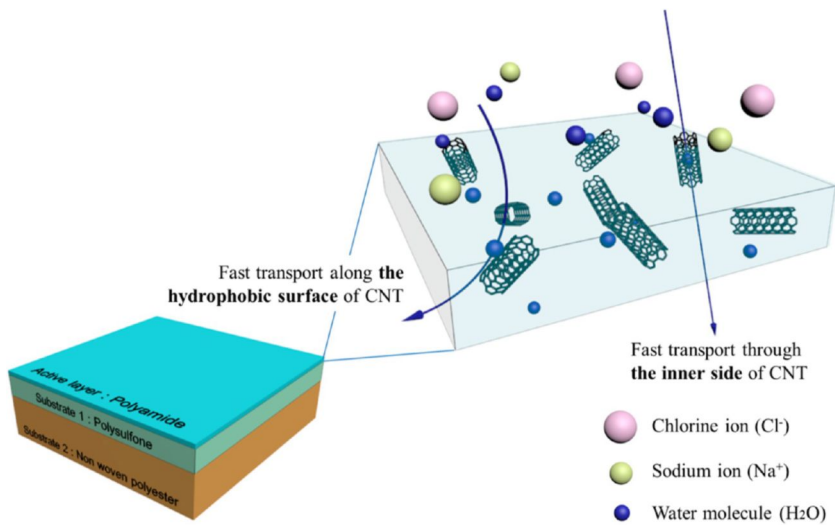


**Figure II-22. Schematic Illustration of the TFN membrane including CNTs. Water Molecules rapidly transfer via fluid transport channel (Kim, Choi et al. 2014).**

### **II.3.3.2. Chemical grafting on surface of TFC membrane**

Early stage grafting is just deposition of additives on TFC membrane surface via vacuum filtration process. Additives attached on the TFC membrane surface via weak van der Waals or electrostatic forces. Therefore, the additives were gradually removed during water filtration and also released to water stream leading to potential risks to humans (Yin, Deng 2015).

For this reason, additives were chemically bonded with TFC membrane surface in later studies. For example, Ag functionalized multi-walled carbon nanotube (MWNT) was grafted on TFC membrane surface using bridging structures such as PEG, ethylene dichloride (EDC), and ethylene diamine (EDA) as shown in Figure II-23 (Gunawan, Guan et al. 2011). Ag also grafted on TFC membrane surface using bridging structure, cysteamine as shown Figure II-24 (Yin, Yang et al. 2013). Furthermore, other functional additives such as TiO<sub>2</sub>, PEG, CNT, and polydopamine were grafted on TFC membrane as similar method as above. As the result, anti-biofouling of TFC membrane was quite increased, and sometimes water permeability was also raised (Yin, Deng 2015, McCloskey, Park et al. 2010, Kang, Liu et al. 2007, Tiraferri, Vecitis et al. 2011).

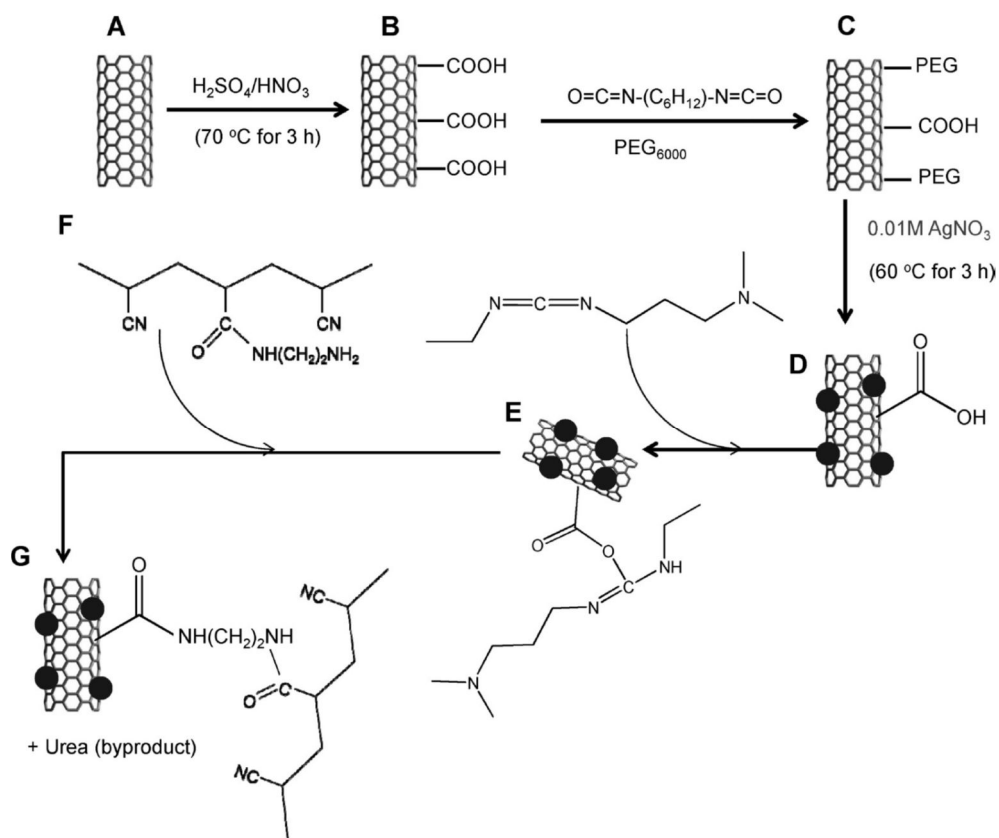


**Figure II-23.** Proposed formation pathway of g) an Ag/MWNT grafted TFC membrane: a) pristine MWNT, b) acid-treated MWNT, c) PEG-grafted MWNT, d) silver NPs deposited MWNT, e) EDC-linked Ag/MWNT, and f) EDA-attached membrane surface (Gunawan, Guan et al. 2011).

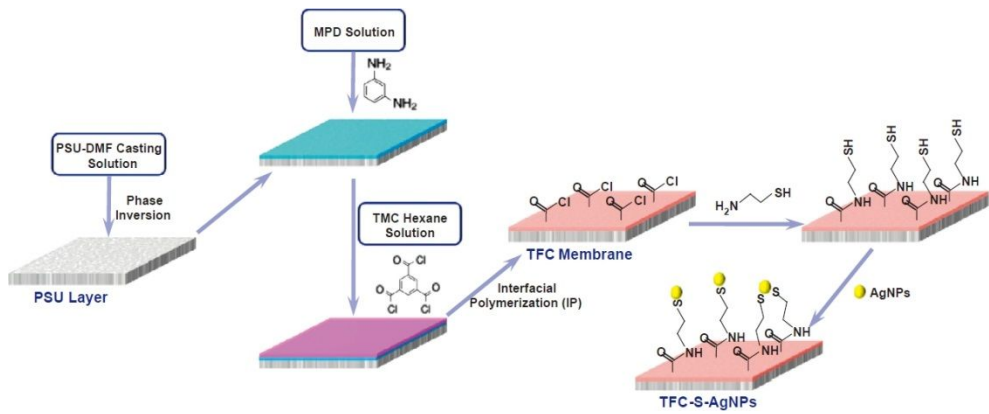


**Figure II-24. Schematic illustration for immobilization of Ag NPs on TFC membrane surface (Yin, Yang et al. 2013).**

### **II.3.3.3. Molecular layer-by-layer (mLbL) assembled TFC membrane**

The major determinants of water permeability of TFC membrane are thickness, surface roughness, and chemical characteristics (ex. hydrophilicity and surface zeta potential) of active layer (Freger 2003, Coronell, Mariñas et al. 2011). As one of approaches to improve water permeability, molecular layer-by-layer (mLbL) assembly method was developed to reduce active layer thickness (Chan, Lee et al. 2012, Gu, Lee et al. 2013, Chan, Young et al. 2013). The concept and mechanism of mLbL method is like that TMC monomers are deposited on the support layer and the MPD monomers are deposited on the TMC monomer layer alternately. At each deposition, deposited monomers make bonds with already deposited monomer. As the result, PA active layer was formed as shown in Figure II-25a (Chan, Lee et al. 2012).

The procedure for fabrication of mLbL TFC membrane is as follows as shown in Figure II-25b (Chan, Lee et al. 2012). 1) Solution **A** of TMC in toluene is deposited onto the substrate to react with the hydroxyl groups of substrate. The drop amount of TMC solution is automatically controlled via automated syringe pump as shown in Figure II-26 (Chan, Lee et al. 2012). 2) The TMC solution is uniformly dispersed via spin coater (Figure II-26). 3) Unreacted TMC is rinsed with solution **B** of toluene. 4) TMC monolayer is dried by spinning. 5) Solution **C** of MPD in toluene is dropped to react with the spare functional groups of TMC monolayer. 6) The MPD solution is dispersed and dried by spinning. 7) The

unreacted MPD is rinsed with solution **D** (acetone). 8) the MPD layer is dried via spinning. This cycle is repeated as desired. The thickness of active layer prepared by mLbL is from 10 nm to 50 nm depending on the number of the mLbL cycles. Because of thin active layer, water permeability of TMC membrane is improved (Chan, Lee et al. 2012). However, mLbL TMC membrane has significant problems. The surface of active layer prepared by mLbL is very smooth. Therefore, water permeability decreases as much as decline of surface roughness (Hirose, Ito et al. 1996, Lee 2014). Furthermore, thin active layer should have relatively low durability and chlorine resistance (Lee 2014).

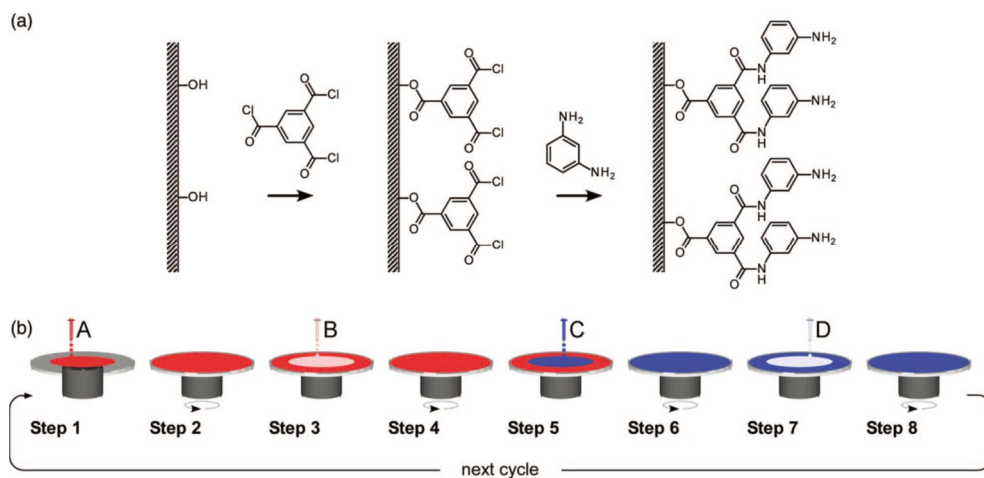


**Figure II-25. a) Schematic illustration of mLBL mechanism and b) procedure (Chan, Lee et al. 2012).**

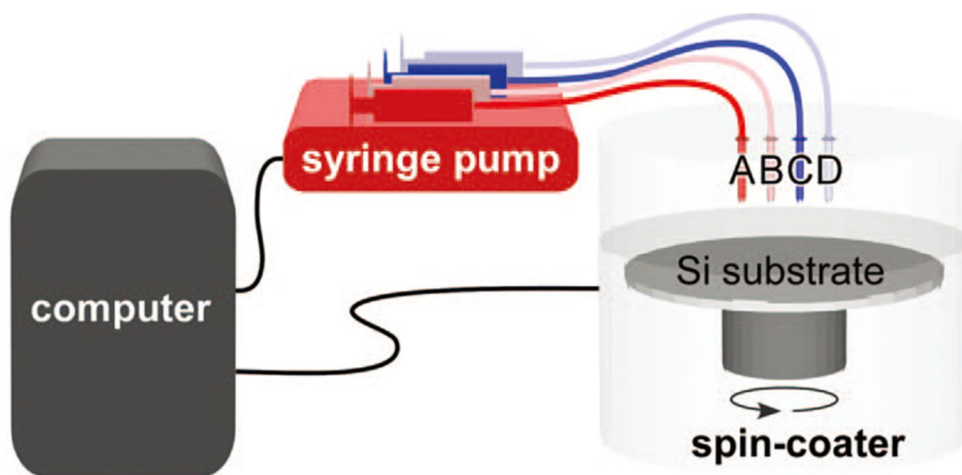


**Figure II-26. a) Schematic illustration of automated spin-coater system with syringe pump (Chan, Lee et al. 2012).**

#### **II.3.3.4. Modified support layer of TFC membrane**

PSf is commonly used for a support layer because PSf has good resistance to compaction, reasonable water permeability, and stability in an acidic environment. The stability in an acidic environment is most important factor since large amount of hydrochloric acid (HCl) is generated by acid polycondensation of MPD and TMC during interfacial polymerization (Lee, Arnot et al. 2011).

Therefore, nowadays there are no studies or reports for material for support layer. However, the effect of PSf concentration on TFC membrane have been recently reported (Ding, Yin et al. 2014, Lee, Jang et al. 2015). Lee et al. reported that the support layer made by lower concentration PSf solution has larger size pores, and consequently, TFC membrane prepared by the support layer exhibited higher water flux with equivalent salt rejection (Lee, Jang et al. 2015). However, Ding et al. reported that salt rejection was decreased whereas water flux was increased when concentration of PSf for support layer was lowed (Ding, Yin et al. 2014). Consequently, further research is required to verify the effect of support layer on TFC membrane.

## **Chapter III**

**Thin-Film Composite Reverse Osmosis Membrane**

**with Graphene Oxide Nanosheets**

**Embedded in the Active Layer**

### **III.1. Introduction**

In recent years, reverse osmosis RO has become one of the most popular desalination technologies because of its high energy efficiency (Feinberg, Ramon et al. 2013, Greenlee, Lawler et al. 2009). The high efficiency of the RO process arise from high water permeability and high salt rejection of polyamide thin-film composite (PA-TFC) membranes. The PA-TFC RO membrane has been continually improved over the last 30 years; however, it still needs improvement in terms of its permselectivity, anti-biofouling, and chlorine resistance (Clark, Allgeier et al. 1998, Escobar, Hoek et al. 2005). In particular, biofouling, the attachment and growth of microorganisms on the surface of a membrane, resulting in higher energy consumption is a major limiting factor in the PA-TFC RO process as it is in various membrane separation processes (Tirafferri, Vecitis et al. 2011, Kwak, Kim et al. 2001). Chlorine is widely used for membrane cleaning; however, the active layer is very vulnerable to chlorine because it readily attacks amide nitrogen and aromatic rings of PA (Elimelech, Phillip 2011, Glater, Hong et al. 1994). Therefore, both anti-biofouling and chlorine resistance are required to solve the biofouling problem in the PA-TFC RO membrane.

In previous studies, some hydrophilic nanomaterials, such as zeolite (Jeong, Hoek et al. 2007), alumina (Saleh, Gupta 2012), titanium dioxide (Lee, Im et al. 2008), and functionalized carbon nanotube (Kim, Choi et al. 2014), have been applied to RO membrane to enhance their permeability (Barona, Lim et al. 2013), anti-biofouling (Goosen, Sablani et al. 2004), and/or chlorine resistance (Kim,

Hyeon et al. 2013). Recently, graphene oxide (GO) nanosheets have been used for RO membrane (Kim, Hyeon et al. 2013, Perreault, Tousley et al. 2013, Choi, Choi et al. 2013) owing to its numerous hydrophilic functional groups (Figure III-1). However, it is difficult to simultaneously enhance all required properties. Kim et al. (Kim, Hyeon et al. 2013) prepared a GO-coated PA-TFC membrane through layer-by-layer deposition on a polysulfone (PSF) support layer before forming the active layer, and that membrane exhibited improved chlorine resistance. Perreault et al. (Perreault, Tousley et al. 2013) synthesized another GO-coated PA-TFC membrane via covalent bonds between GO nanosheets and PA on the active layer, resulting in 65% improved anti-fouling property. Choi et al. (Choi, Choi et al. 2013) reported that another GO-coated PA-TFC membrane prepared by layer-by-layer deposition on both PA and PSF layers not only exhibited chlorine resistance but also enhanced the anti-fouling property by 56% and increased the water flux by 12%. All previous studies adopted the “coating” method (i.e., GO layer on top of the active layer) in applying GO nanosheets. However, because the GO coating layer can interfere with water permeation, the “coating” method can pay a price for decrease in water permeability.

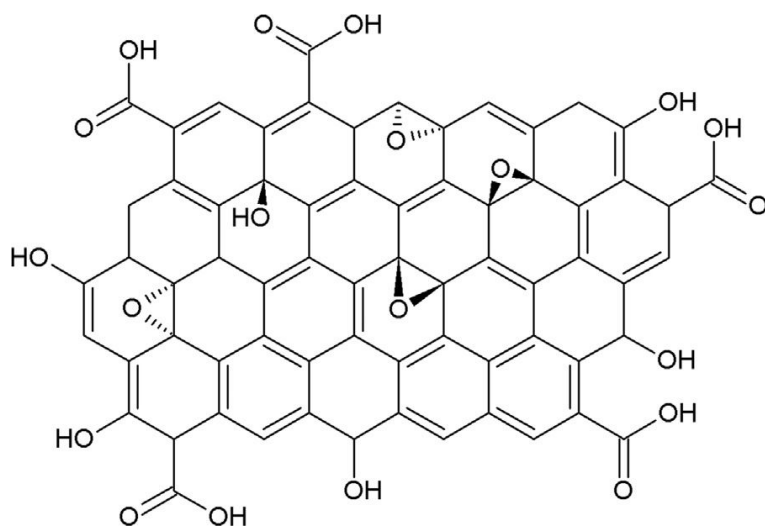


**Figure III-1. Schematic illustration of GO molecular structure.**

In this study, it was assumed that dispersed GO nanosheets in the active layer would not interfere with water permeation, Therefore, instead of coating GO nanosheets on top of the active layer, GO nanosheets were embedded in the active layer by adding it to an aqueous solution of MPD before interfacial polymerization. This GO-embedded PA-TFC RO membrane (GO-TFC membrane) was evaluated in terms of water permeability, anti-biofouling, and chlorine resistance as well as in a lab-scale cross-flow filtration system.

## III.2. Experimental

### III.2.1. Materials

Graphite (Sigma-Aldrich, USA), potassium permanganate ( $\text{KMnO}_4$ , Sigma-Aldrich, USA), sulfuric acid ( $\text{H}_2\text{SO}_4$ , Daejung Chemicals & Metals Co., Ltd., Korea), nitric acid ( $\text{HNO}_3$ , DC Chemical Co., Ltd., Korea), and hydrogen peroxide ( $\text{H}_2\text{O}_2$ , Junsei Chemical Co., Ltd., Japan) were used for the preparation of GO nanosheets. MPD that was provided by DuPont (USA) and trimesoyl chloride (TMC, Sigma-Aldrich, USA) were used for fabricating the active layer. Isoparaffin (ISOL-C) provided by SK Global Chemical Co., Ltd. (Korea) and the PSF ultrafiltration (UF) membrane provided by Woongjin Chemical Co., Ltd. (Korea) was used as the support layer for interfacial polymerization. Sodium chloride ( $\text{NaCl}$ ), sodium hypochlorite ( $\text{NaOCl}$ ), and hydrochloric acid ( $\text{HCl}$ ) were purchased from Daejung Chemicals & Metals Co., Ltd. (Korea) for evaluating membrane performance. Deionized (DI) water was produced with a Direct-Q system (Millipore, USA).

### **III.2.2. Preparation of graphene oxide nanosheets**

GO nanosheets were prepared through chemical exfoliation of graphite based on the Hummers method (Hummers, Offeman 1958). Graphite was oxidized by oxidants such as nitric acid, sulfuric acid, potassium permanganate, and hydrogen peroxide, and it was converted into graphitic oxide. The graphitic oxide aqueous solution was neutralized by removing acidic solvent using a centrifuge and adding DI water several times. Then, the graphitic oxide was converted into GO nanosheets by sonication under a sonication power of 563 W for 2 h. Lastly, the GO nanosheets were fractionated by a track-etch membrane with a pore size of 5  $\mu\text{m}$  (Nuclepore, Whatman, USA) to eliminate large-size GO nanosheets ( $> 10 \mu\text{m}$ ). Then only the fractionated small-size GO nanosheets ( $< 5 \mu\text{m}$ ) was used to prepare the GO-TFC membrane because the large-size GO nanosheets caused an abnormal surface morphology (Figure III-2b, b' and b'') whereas the small-size GO nanosheets exhibited higher dispersion stability in water. In addition, abnormal surface morphology could be caused by interference of GO nanosheets in MPD diffusion, and GO nanosheets would be placed at subsurface because the wrinkles in Figure III-2b'' and c'') resembled the wrinkles in Figure II-9.

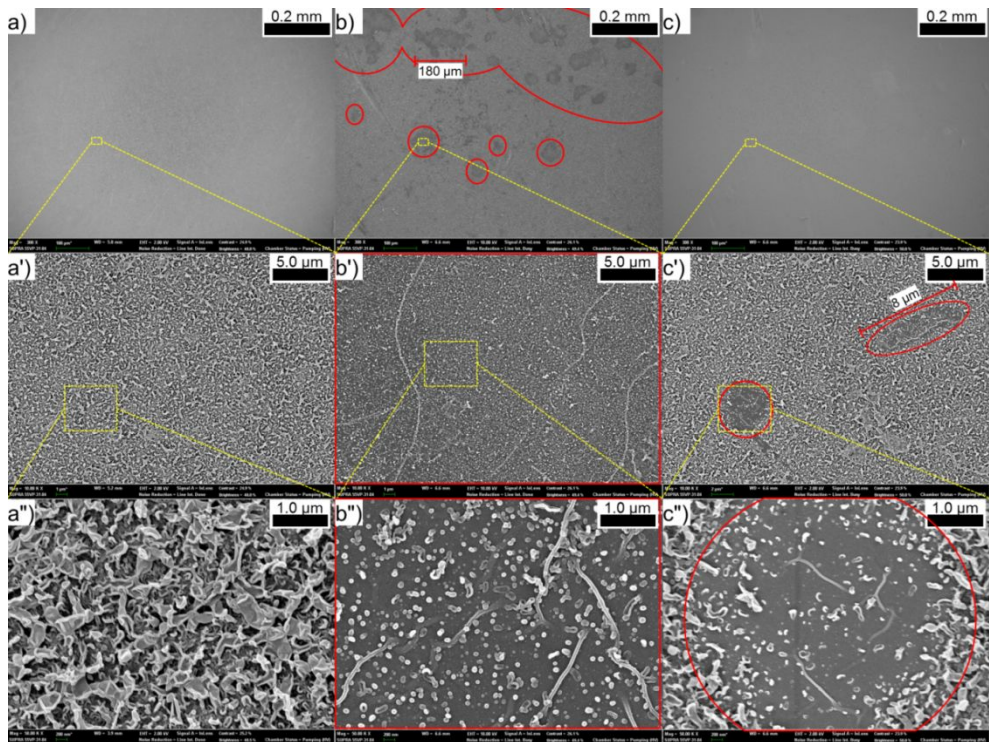


Figure III-2. SEM surface images of three TFC membranes: TFC membranes prepared (a, a', and a'') without GO nanosheets and with (b, b', and b'') non-fractionated and (c, c', and c'') fractionated GO nanosheets. The GO concentration in MPD solutions for the A- and AS-GO-TFC membranes was 15 ppm.

### **III.2.3. Preparation of GO-TFC membrane**

The GO-TFC membrane was prepared by interfacial polymerization on the PSF UF membrane: the PSF UF membrane was immersed into a 3 wt% MPD aqueous solution containing GO nanosheets (0, 15, 38, and 76 ppm of each) for 1 min. Excess MPD solution remaining on the PSF UF membrane was removed by squeezing it under a butadiene rubber roller for approximately 40 s. After drying in air for 1 min, the PSF UF membrane was immersed in 0.1 w/v% TMC in ISOL-C for 1 min to form an active layer via interfacial polymerization. Lastly, the membrane was dried in air for 10 min and stabilized in DI water for 90 min. The TFC membrane that was made using an MPD solution containing x ppm of GO nanosheets is denoted as the x-GO-TFC membrane.

### **III.2.4. Characterization of graphene oxide nanosheets**

The lateral size and thickness of the fractionated GO nanosheets were measured using a scanning probe microscope (SPM, INNV-BASE, VEECO, USA) with a cantilever tip (PPP-NCHR-10, NANOSENSORS, Switzerland). A silicon wafer (4 WAFER P-100, Sehyoung wafer-tech, Korea) was immersed in and removed vertically from the GO aqueous solution to orient the GO nanosheets horizontally (Yang, Yang et al. 2014) with the wafer similar to Langmuir–Blodgett film deposition (The film was deposited and arrayed horizontally with the substrate when the substrate was removed vertically from the solution) (Petty 1996). SPM measurements were performed after the residual water on the wafer had dried. The fractionated and non-fractionated GO nanosheets in DI water (500 ppm each) were evaluated in terms of the size distribution and zeta potential. The size distributions were measured using a laser diffraction particle size analyzer (LS 13 320, Beckman Coulter, USA). The numbers of GO nanosheets at various size ranges were counted over the range of 4–120  $\mu\text{m}$  using a particle counter (Multisizer 4, Beckman Coulter, USA) to observe the trace amounts of large-size GO nanosheets. The change in the zeta potential of GO nanosheets with fractionation was measured using a zeta-potential and particle-size analyzer (ELS-Z, Otsuka Electronics, Japan). The shape and composition of fractionated GO nanosheets were also estimated using transmission electron microscopy (TEM, LIBRA 120, Carl Zeiss, Germany), and X-ray photoelectron spectrometer (XPS, AXIS-His, Kratos, Japan), respectively. The GO solution was dropped and dried dozens of times on a Formvar

grid for TEM and on a silicon wafer for XPS. The Fourier transform infrared (FTIR) spectrum of the fractionated GO nanosheets was also acquired using an FTIR spectrophotometer (Nicolet 6700, Thermo Scientific, USA) using a mass of dried GO nanosheets.

### III.2.5. Characterization of GO-TFC membrane

The presence of GO nanosheets in the prepared membrane was examined using a Raman spectrometer (LabRam 300, Horiba Jobin Yvon, France). Raman spectra of 0- and 152-GO-TFC membranes were acquired in the range from 1000 to 3500  $\text{cm}^{-1}$  with 532-nm laser continuous wave, 100x objective lens (N.A. = 0.90, Olympus, Japan), 0.4-mW data sample power, and 30-s sample acquisition time.

The contact angle, surface zeta potential, and surface average roughness of the GO-TFC membranes were evaluated. The contact angles were measured by a drop shape analysis system (DSA 100, KRÜSS, Germany) to evaluate the membrane hydrophilicity. The membranes were dried for 24 h right after membrane preparation, and then the contact angles were measured with a 5.0- $\mu\text{L}$  DI water drop using the sessile drop method. The surface zeta potentials were measured using a zeta-potential and particle-size analyzer (ELS-Z, Otsuka Electronics, Japan) using a monitor solution provided by Otsuka Electronics (10-mM NaCl aqueous solution containing monitor particles) after the cell constant was set using a 10 mM NaCl aqueous solution.

The surface average roughnesses ( $R_a$ ) of the 0, 15, 38, and 76-GO-TFC membranes were measured using an SPM with a cantilever tip. The SPM was operated in tapping mode at a fixed scanning rate of 0.7 Hz over the scan range of  $3.0 \times 3.0 \mu\text{m}^2$ . The cross-sectional and surface morphology of the membranes were examined using a field-emission scanning electron microscope (FE-SEM, SUPRA 55VP, Carl Zeiss, Germany) to determine the change in the ridge and valley

structure with GO content in detail following platinum coating on the membranes with a platinum sputter coater (SCD 005, BAL-TEC, Germany). If the active layer has a high roughness (non-uniform thickness), the thickness of the active layer is not the same as the height of the ridges. For this reason, the thickness of the active layer in the cross-sectional SEM images was evaluated using a new method as follows. (1) Using the tilting and rotating option, the exact cross-sectional view of the horizontal membrane surface was obtained by FE-SEM (Figure III-3a). (2) That image was cut along the line that seemed to be the surface of support layer (Figure III-3b). (3) The area of the active layer in the cross-sectional SEM images was determined using a computer program “Image J” (Figure III-3c). Lastly, the area was divided by the width of the SEM image, with the quotient being the average thickness of the PA active layer.

The oxygen weight fractions of the 0, 15, 38 and 76-GO-TFC membranes were measured using an energy dispersive spectroscope (EDS, Xflash Detector 4010, Bruker, USA). The EDS measurements were conducted using a FE-SEM after coating the membrane surface with platinum using a platinum sputter coater. The FE-SEM was operated at an acceleration voltage of 15.0 kV under a magnification of 3000x.

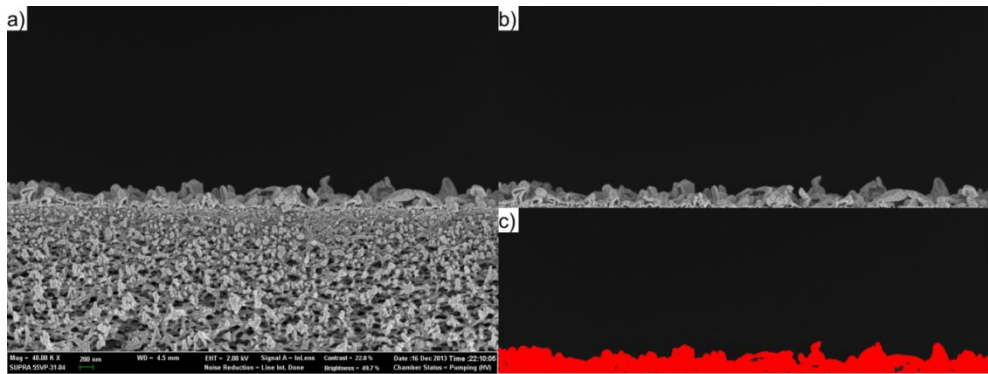


**Figure III-3. (a) Cross-sectional SEM image, (b) active layer part of the SEM image, and (c) silhouetted active layer part.**

### III.2.6. Performance of GO-TFC membrane

The membrane permselectivities of the 0, 15, 38, and 76-GO-TFC membranes were evaluated with a lab-scale cross-flow filtration system. Over the entire period, a 2000-ppm NaCl aqueous solution flowed in the cross-flow module, and the temperature was maintained at 25°C using a low-temperature bath circulator (RW-0525G, Lab Companion, Korea). Pre-filtration was conducted at 350 psi for 30 min to achieve membrane compaction before the main filtration, which was performed at 225 psi for 30 min. At the end of the run, both the water flux and salt rejection were measured. To verify the effect of GO fractionation, the water permeability of the 0, 15, 38, and 76-GO-TFC membranes containing non-fractionated GO nanosheets were also measured at the same method as above. The anti-biofouling property of the GO-TFC membrane was examined using a cell attachment test in a cocurrent downflow contactor reactor (CDC reactor, BioSurface Technologies Corporation, USA). First, *Pseudomonas aeruginosa* (PAO1) with a green fluorescent protein (GFP) tag cultured in 1/10 Tryptic Soy Broth (TSB, Becton, Dickinson and Company, USA) for 18 h at 37°C was diluted until the optical density reached 0.28. Then the CDC reactor in which the 0, 15, 38, and 76-GO-TFC membranes were set was filled with 300 mL of 1/100 TSB, and the diluted PAO1 was inoculated into the reactor. The inoculated PAO1 was cultured for 24 h at 25°C under batch condition with stirring at 80 rpm. Then 1/100 TSB was fed into the reactor at a flow rate of 1.4 mL/min for 24 h with continuous drain at the same flow rate. During the test, light was blocked out by wrapping the reactor with

aluminum foil to avoid the dissipation of fluorescence. After the test, cells attached on the membranes were observed using a confocal laser scanning microscope (CLSM, C1 Plus, Nikon, Japan). Using the CLSM data, the biovolume of the cells attached on the membranes was quantified by a computer program “image structure analyzer-2” (ISA-2), which Beyenal et al. (Beyenal, Donovan et al. 2004) developed and reported for the analysis of biofilm. The graphical threshold for ISA-2 processing was determined automatically by Otsu's method (Otsu 1979).

The chlorine resistances of the GO-TFC membranes were evaluated using the following procedure. A 2000-ppm sodium hypochlorite solution was prepared by 50 times dilution of a 10 wt% sodium hypochlorite solution, and then its pH was adjusted to 7 with hydrochloric acid to examine the chlorine stability while excluding the effect of acidic or basic condition. Each of the four membranes was immersed in the sodium hypochlorite solution individually. The beaker containing each membrane was sealed with parafilm (Bemis, USA) and wrapped with aluminum foil to block light. After 24 h, the membrane was rinsed and soaked for 1 h with DI water. Then, the water flux and salt rejection of each chlorine-treated membrane were measured using the same method as described in the above test for membrane permselectivity.

### **III.3. Results and discussion**

#### **III.3.1. Characterization of graphene oxide nanosheets**

The fractionated GO nanosheets were characterized in several ways. First, the lateral size and thickness of the fractionated GO nanosheets were measured by SPM and observed to be 70–140 nm and 1–2 nm, respectively (Figure III-4). The thickness of the GO nanosheets (1–2 nm) indicated that those were fully exfoliated single or double-layer GO nanosheets. After fractionation, the size distribution of GO nanosheets in Figure III-5a shifted to the left. That implied the fraction of small-size GO nanosheets was increased. Moreover, the average size of GO nanosheets was reduced from 1.0  $\mu\text{m}$  to 0.4  $\mu\text{m}$  (Figure III-5a). In addition, the total number of large-size GO nanosheets was reduced by approximately 74 % via fractionation (Figure III-5b). The discrepancy in the particle size results measured by SPM or particle analyzer might originate from the difference not only in the measurement mechanism but also in the number of measurements. Even though GO nanosheets were fractionated with a 5- $\mu\text{m}$  filter, undesired rejection of GO nanosheets smaller or passage of GO nanosheets larger than 5  $\mu\text{m}$  was unavoidable. The inhibition to the passage of small-size GO nanosheets might be attributed to the secondary dynamic membrane layer (Lee, Ahn et al. 2001) formed by large-size GO nanosheets. In addition, GO nanosheets with lengths greater than 5  $\mu\text{m}$  could pass through the membrane because of its planer and elliptical shape. Note that the zeta potential of GO nanosheets also changed from -33.8 mV to -45.5 mV after fractionation. In other words, GO nanosheets have a more negative zeta potential as

its average size decreases, which could be caused by increasing the “edge” of GO nanosheets to which numerous negatively charged functional groups are attached (Figure III-1). The augmentation of the negative zeta potential is considered to result in two advantages: (1) the surface zeta potential of the GO-TFC membrane became more negative with the same GO dosage and (2) the dispersion stability of GO nanosheets in water increased (Li, Muller et al. 2008), resulting in a more homogeneous dispersion of GO nanosheets in the active layer.

Many GO nanosheets with sizes from 10 to 50 nm were observed by TEM (Figure III-6), similarly to the SPM measurements (Figure III-4). In the TEM image, the shape of the GO nanosheets was a rounded square. The FTIR spectrum of fractionated GO nanosheets (Figure III-7a) indicated the presence of O–H groups ( $3369\text{ cm}^{-1}$ ), C=O stretching vibration in carboxyl groups ( $1722\text{ cm}^{-1}$ ), unoxidized  $\text{sp}^2$  aromatic C=C bonds ( $1623\text{ cm}^{-1}$ ), C–O stretching vibration in epoxy groups ( $1224\text{ cm}^{-1}$ ), C–O stretching vibration in alkoxy groups ( $1053\text{ cm}^{-1}$ ) (Wang, Wang et al. 2009, Wojtoniszak, Chen et al. 2012). The C1s XPS spectrum of fractionated GO nanosheets (Figure III-7b) was fitted by four components: C–C and C=C (33%, 284.5 eV), C–O (21%, 285.4 eV), C=O (37%, 287.1 eV) and C(O)OH (9%, 288.9 eV) (Dreyer, Park et al. 2010, Shang, Ma, et al. 2012). The XPS spectrum indicated that approximately 65% of the carbon atoms were successfully oxidized.

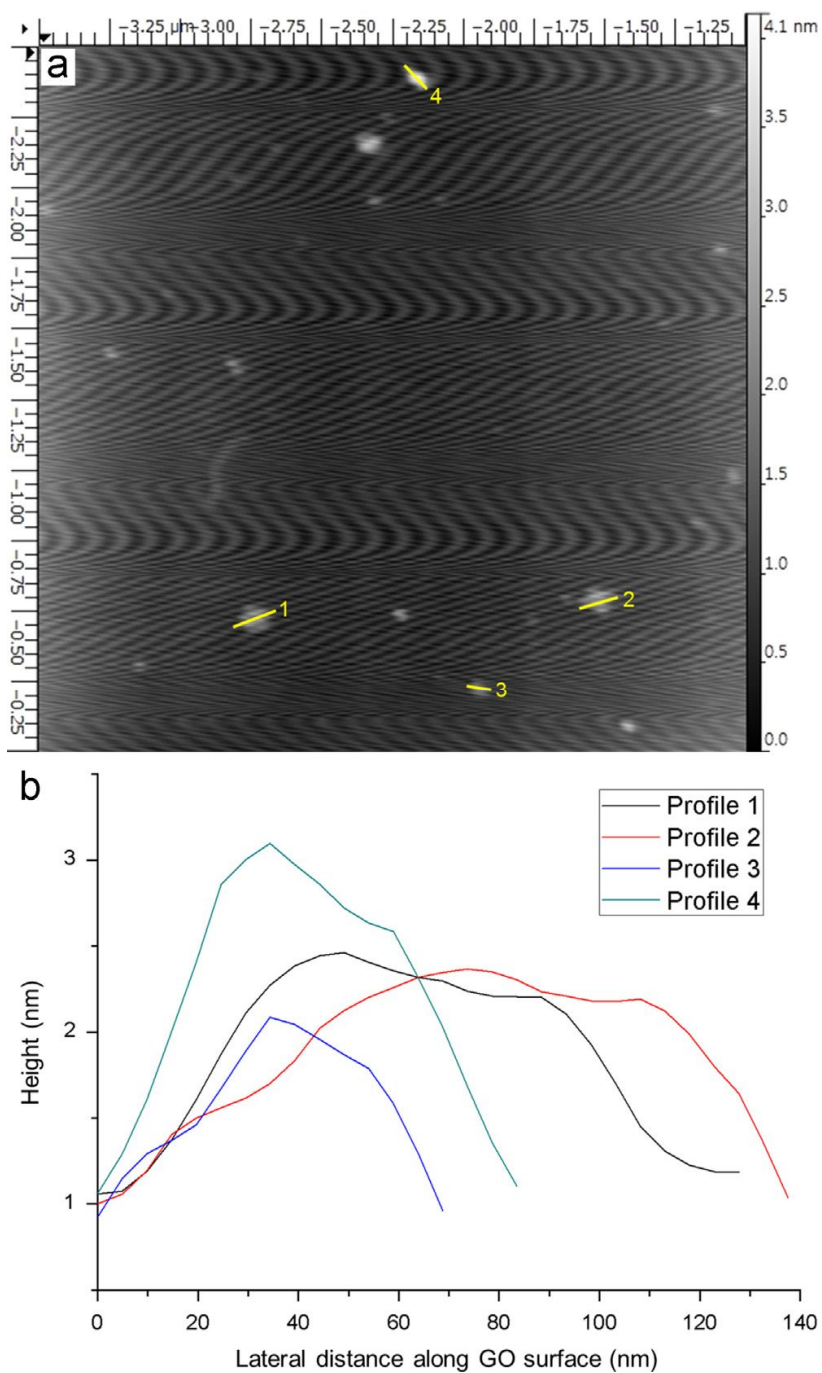


**Figure III-4. (a) SPM image of GO nanosheets (white spots) on silicon wafer (dark background) and (b) lateral size and thickness of several GO nanosheets.**

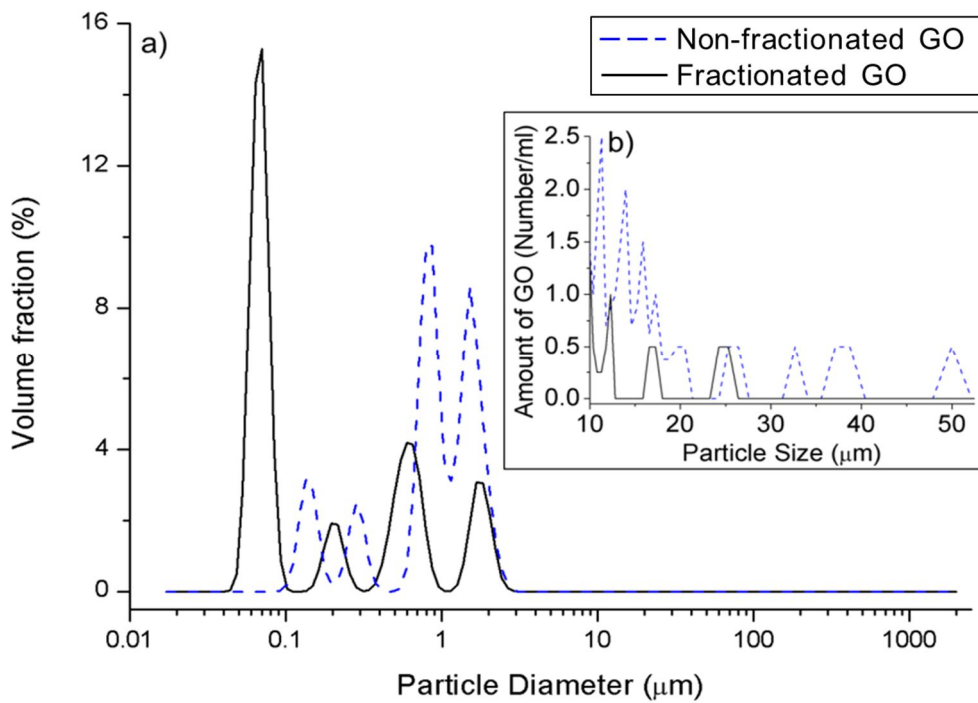


**Figure III-5. (a) Size distributions in volume fraction and (b) number concentration at each given size of fractionated and non-fractionated GO nanosheets.**

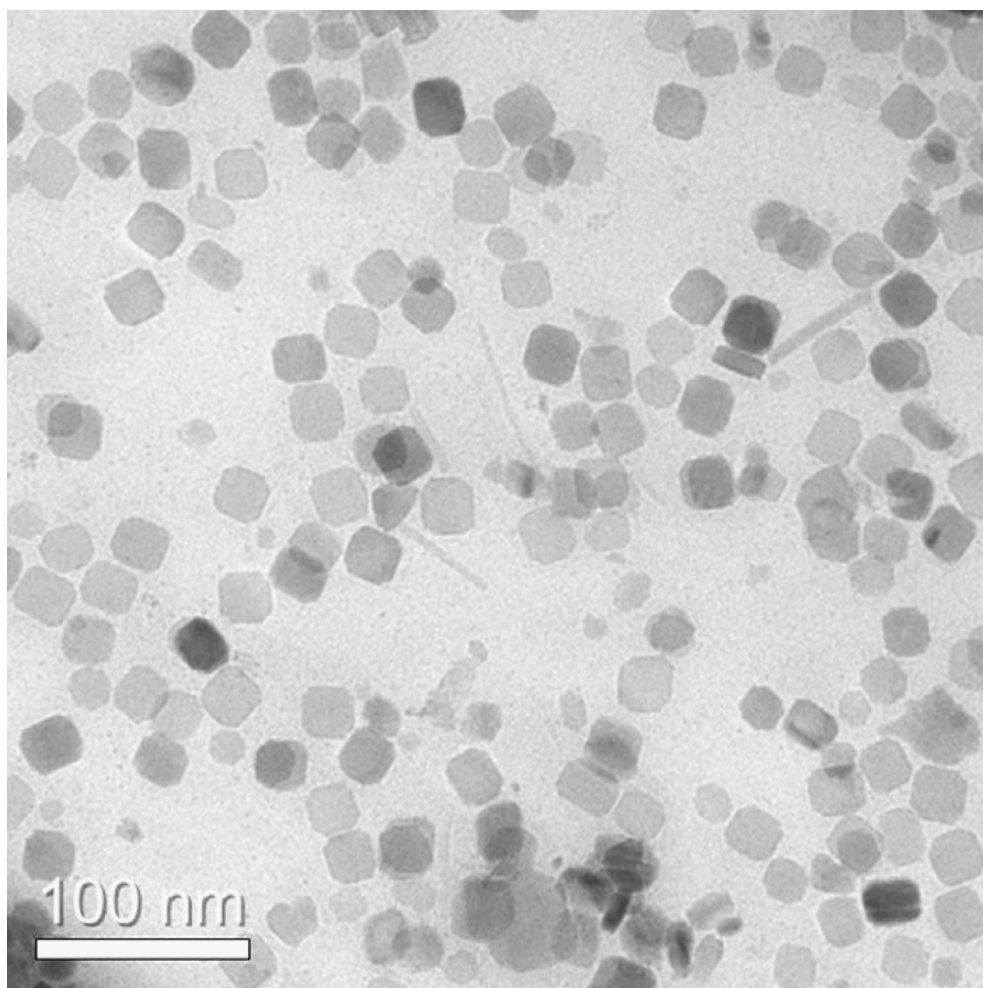


**Figure III-6. TEM image of fractionated GO nanosheets.**

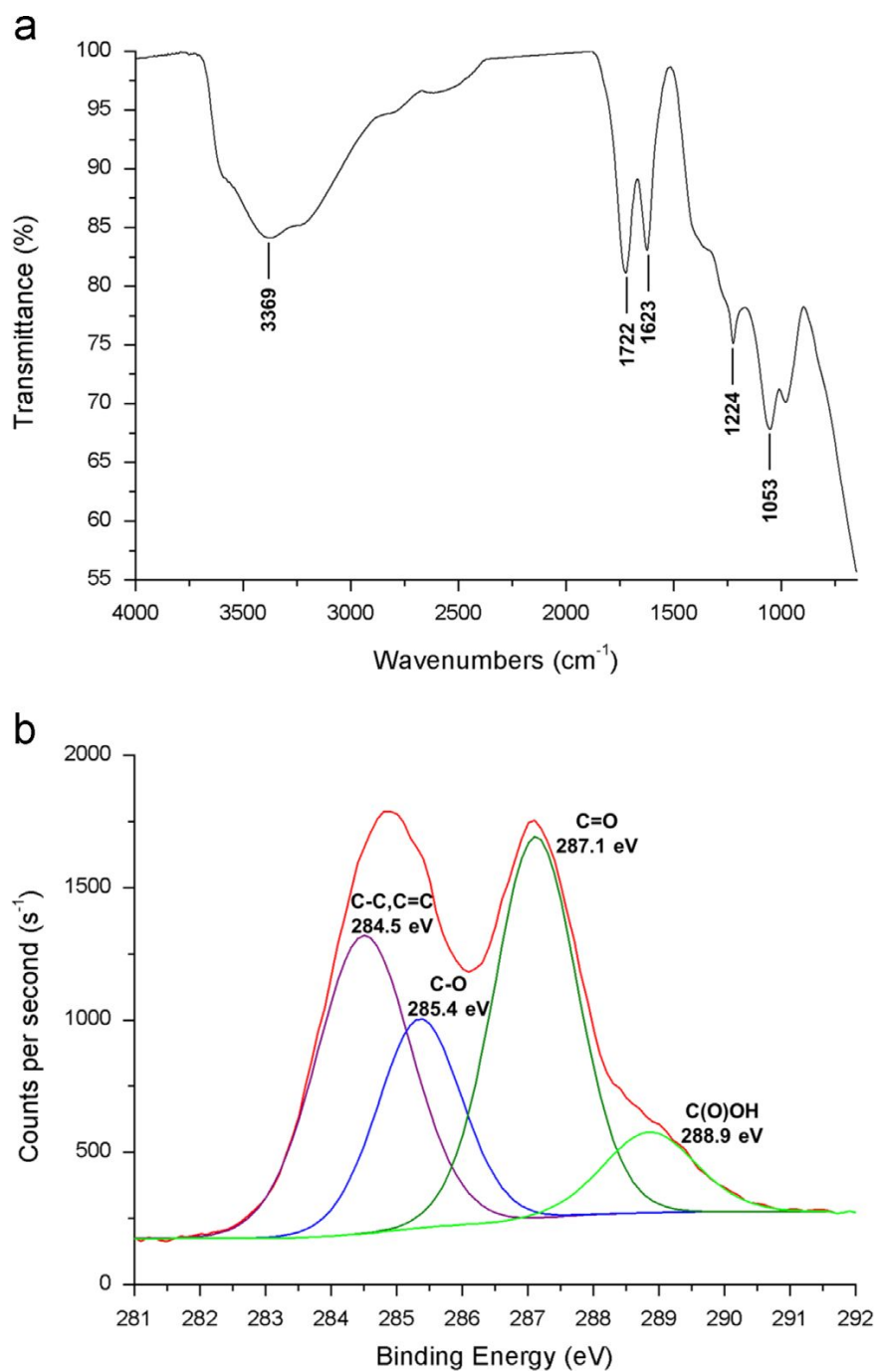


**Figure III-7. (a) FTIR spectrum and (b) C1s XPS spectrum of fractionated GO nanosheets.**

### III.3.2. Characterization of GO-TFC membrane

The presence of GO nanosheets in the active layer was inferred by Raman spectra (Figure III-8a). The Raman spectrum of the TFC membrane without GO nanosheets almost originated from the thick PSF layer (Perreault, Tousley et al. 2013): two bands at 1075.9 and 1109.2  $\text{cm}^{-1}$  originated from symmetric and antisymmetric  $\text{SO}_2$  stretching, respectively. One strong band at 1149.6  $\text{cm}^{-1}$  arose from symmetric C–O–C stretching, and two bands at 1586.1 and 1609.2  $\text{cm}^{-1}$  correspond to a phenyl ring vibration (Figure III-8b) (Kim, Fouda et al. 2000). In addition, the peaks of the phenyl ring vibration are higher than the typical PSF peaks because of the phenyl ring of aromatic PA (Figure III-8c). However, in the Raman spectrum of the 152-GO-TFC membrane, two broad peaks are observed at 1361.2  $\text{cm}^{-1}$  and  $\sim 1600 \text{ cm}^{-1}$ , which are the characteristic peaks of GO nanosheets, denoted as D and G peaks, respectively. The D and G peaks were caused by the in-plane stretch vibration of benzene, and in particular, the D peak appears only in the presence of (graphite lattice) disorder (Kudin, Ozbas et al. 2008). The presence of D and G peaks in Figure III-8a, therefore, verifies the presence of GO nanosheets in the GO-TFC membrane. The G peak is one broad peak similar to the D peak but is not clearly observed because of overlapping with PSF peaks.

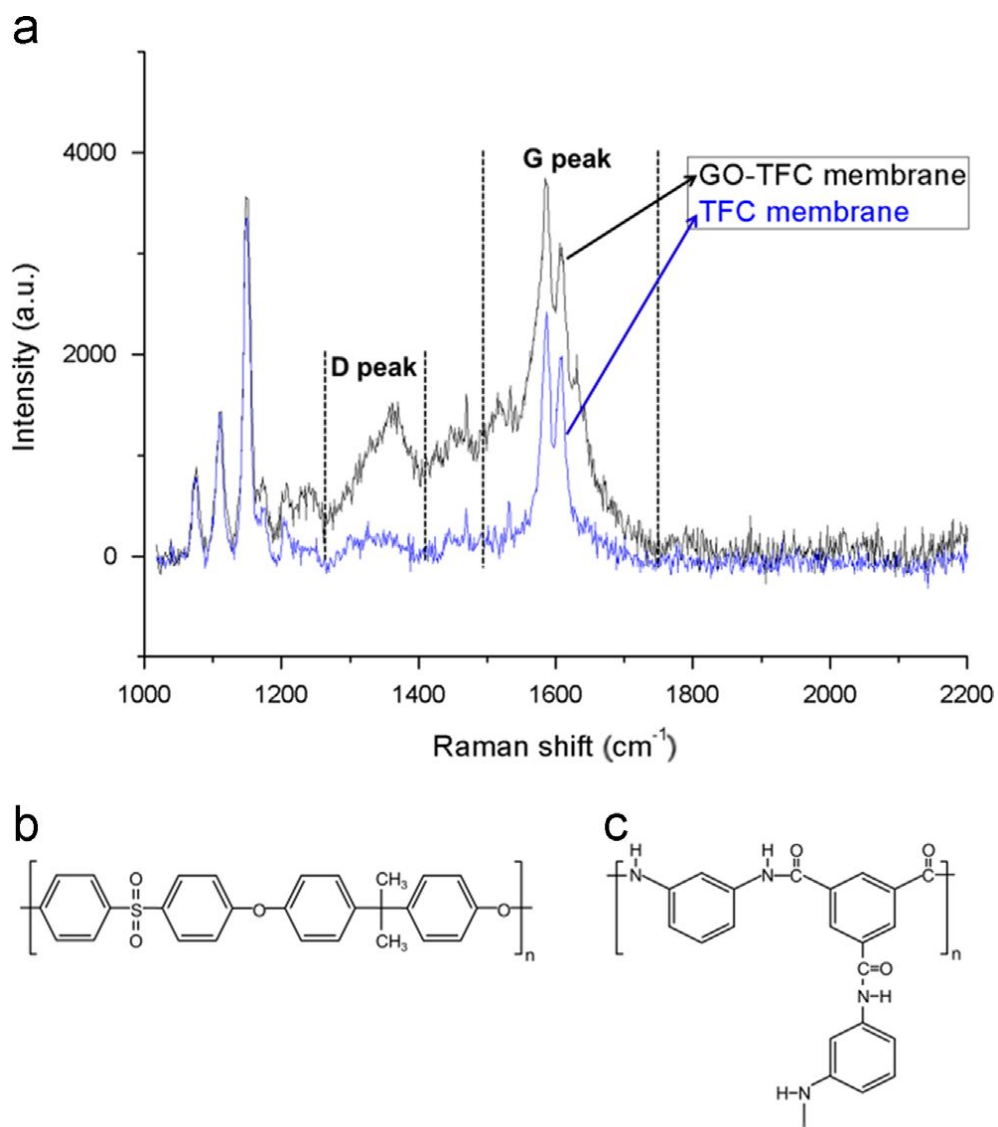


**Figure III-8.** (a) Raman spectra of 152-GO-TFC membrane and TFC membrane without GO nanosheets. D and G represent the typical GO peaks. Schematic molecular structure images of (b) PSF and (c) PA.

The average surface roughness, contact angle, and surface zeta potential of the 0, 15, 38, and 76-GO-TFC membranes decreased consistently with the GO content (Figure III-9). In other words, the GO-TFC membrane became smoother, more hydrophilic, and more negatively charged with the increase of the GO content. For the 76-GO-TFC membrane, these values reached 58 nm, 47°, and -42 mV, respectively, and correspond to reductions of 32%, 38%, and 106% compared with those of the TFC membrane. The decrease of the average surface roughness with GO content was also observed in the SPM and SEM images. The SPM images (Figure III-10) showed that the surface roughness of TFC membrane was decreased with increasing GO content. In addition, both of the maximum height of ridges and shadow caused by fluctuation of ridge heights in Figure III-10 are decreased.

The difference in surface morphology was also shown to compare surface morphology of 76-GO-TFC membrane with that of TFC membrane (Figure III-11). The brighter and darker parts on the surface SEM images (Figure III-11a and b) were believed to be ridges and valleys, respectively, of the active layer because protruding ridges are generally brighter in a SEM image because of the “edge effect” (Shimizu, Everhart et al. 1978). Therefore, higher contrast on the 0-GO-TFC membrane surface indicates that the surface roughness of the 0-GO-TFC membrane was greater than that of the 76-GO-TFC membrane. Moreover, the ridge heights of the TFC membrane appeared to be slightly higher than those of the 76-GO-TFC membrane (Figure III-11c and d), which could be associated with the higher surface roughness of the 0-GO-TFC. In addition, the average thickness of the active layer was also decreased with increasing GO content (Figure III-12). The

average thickness of the active layer of 76-GO-TFC membrane is 244 nm, which is thinner by approximately 30% compared with that of the TFC membrane.

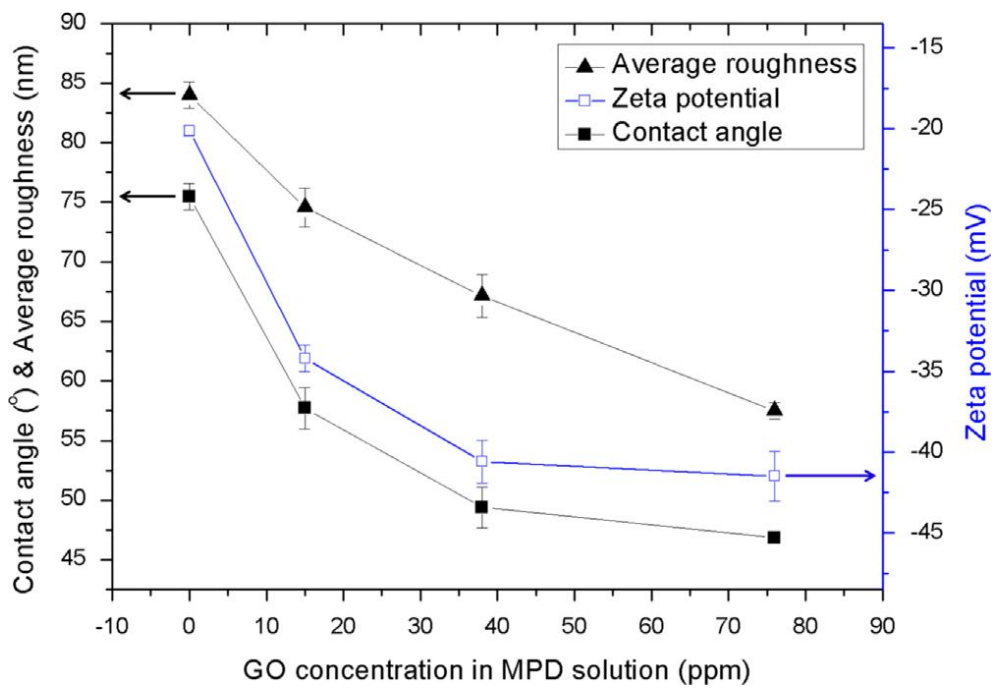


**Figure III-9. Contact angle, surface zeta potential and surface average roughness of the 0, 15, 38, and 76-GO-TFC membranes.**

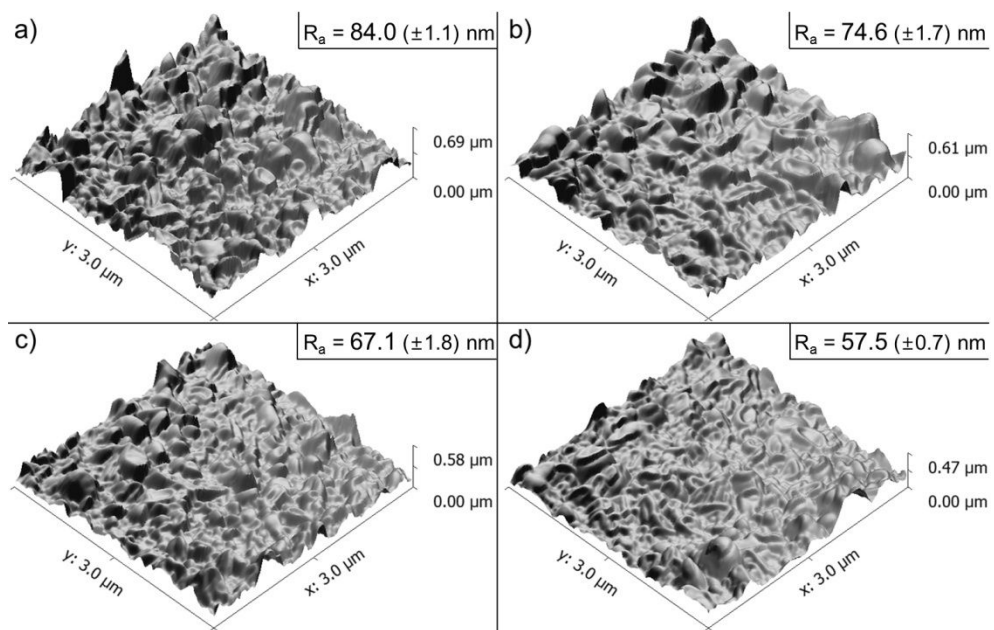


**Figure III-10. SPM surface images for the (a) 0, (b) 15, (c) 38, and (d) 76-GO-TFC membranes. The ridge heights and surface roughness were observed to decrease with increasing GO content. The average roughness of each membrane was shown in the upper right corner of each image.**

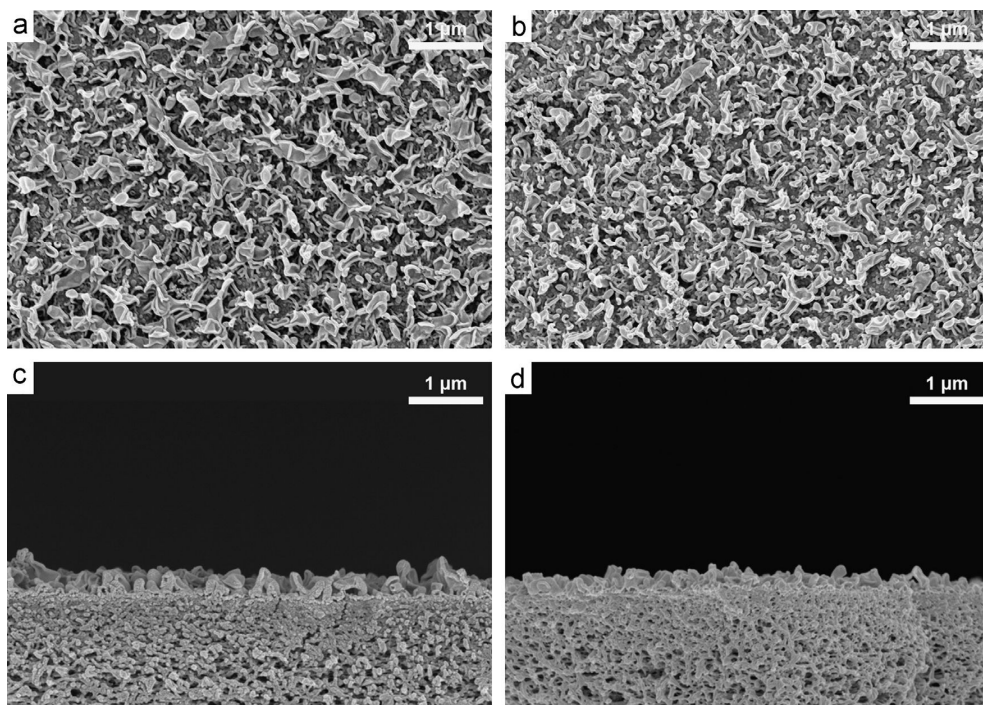


**Figure III-11. SEM images of top and cross-sectional views of 0-GO-TFC (a) and (c) and 76-GO-TFC membranes (b) and (d).**

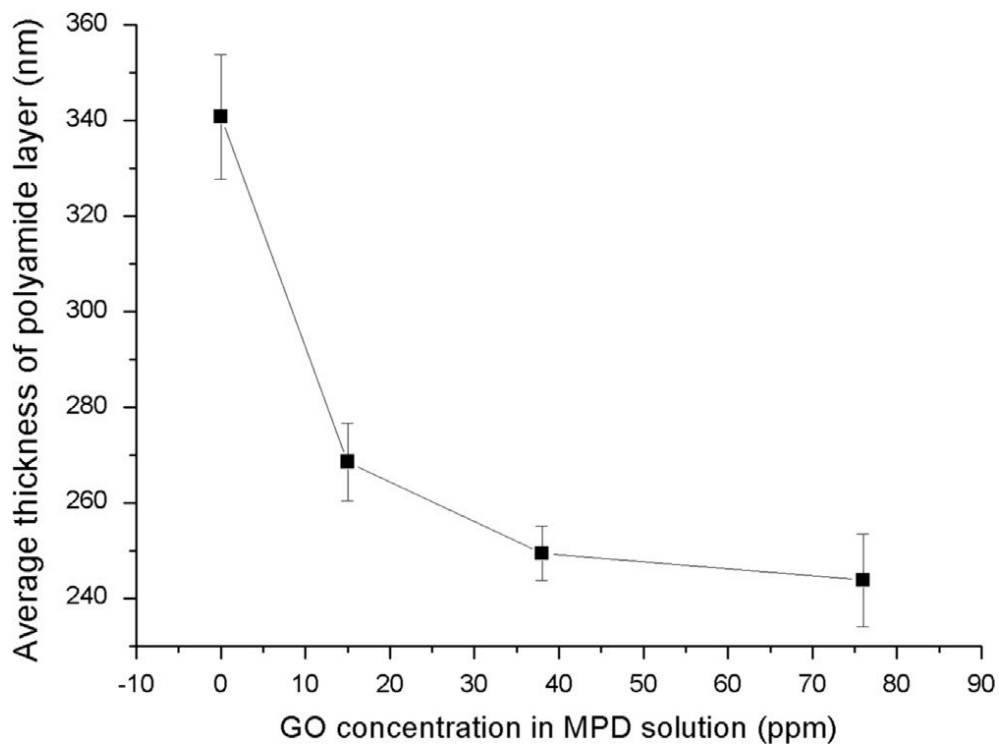


**Figure III-12. Average thickness of polyamide layer as a function of GO content for the 0, 15, 38, and 76-GO-TFC membranes.**

The decrease of the roughness and thickness of the active layer might be due to the retardation of MPD diffusion into the organic solvent by the GO nanosheets. The GO nanosheets on a PSf membrane were likely to be oriented horizontally along the membrane surface when the PSf support layer was vertically removed from the GO-MPD solution (Yang, Yang et al. 2014) due to the Langmuir–Blodgett film deposition (Petty 1996). During the interfacial polymerization, the MPD diffusion usually leads to ridge formation. However, further MPD diffusion is blocked by the initially formed dense active layer and consequently further growth of the ridge is restricted (Song, Sun et al. 2005). Likewise, the horizontally oriented GO nanosheets would inhibit the MPD diffusion and thus lower the roughness and thickness of the active layer. In fact, the non-fractionated larger-size GO nanosheets ( $> 10 \mu\text{m}$ ) seemed to block the MPD diffusion more efficiently such that only few and small ridges might have been formed (Figure III-2c).

The decrease of the surface zeta potential of the GO-TFC membrane should originate from numerous negatively charged functional groups of GO nanosheets. In contrast, the decline of the contact angle was attributed to the increase of the oxygen fraction in the active layer with GO addition (Figure III-13).

However, it was also observed that the decline rates of the contact angle decreased with increasing GO content (Figure III-9). The slowdown might be related to the decrease of the surface roughness. Wenzel et al. (Wenzel 1936) reported the effect of surface roughness on the contact angle and established the Wenzel equation

$$\cos \theta_2 = r \times \cos \theta_1$$

where  $\theta_1$  and  $\theta_2$  are the contact angles of the actual (rough) surface and projection (flat) surface, respectively, and “ $r$ ”, the roughness factor, is defined as the ratio of the actual surface area to the projection area. The Wenzel equation means that the contact angle should increase with decreasing surface roughness because the contact angle was smaller than  $90^\circ$ . Consequently, the slowdown of the change in contact angle could be caused by the trade-off between the increase of the oxygen content and the decrease of the surface roughness with increasing GO content.

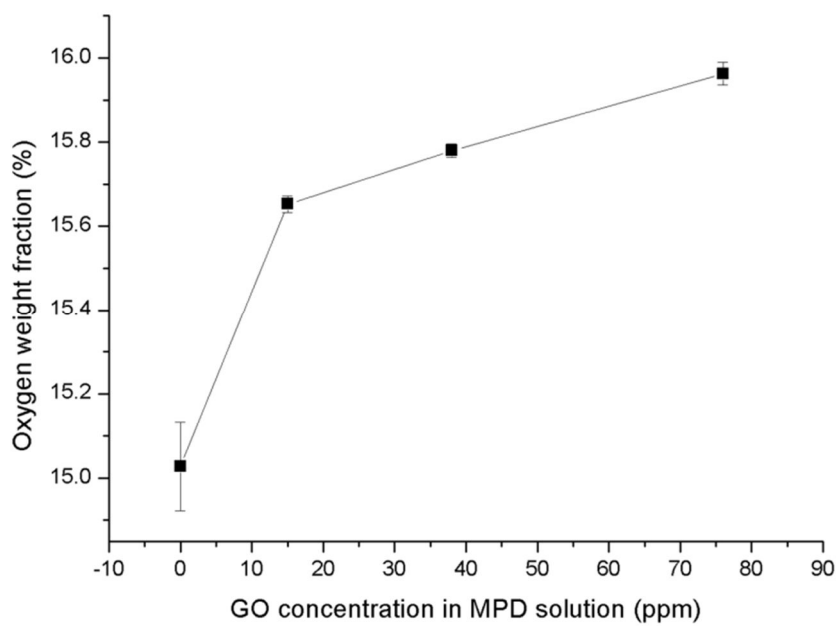


**Figure III-13. Oxygen weight fraction of the 0, 15, 38, and 76-GO-TFC membranes measured by EDS.**

### **III.3.3. Performance of GO-TFC membrane**

The GO-TFC membrane exhibited higher water flux than the TFC membrane without loss of salt rejection (Figure III-14). The water flux of the 38-GO-TFC membrane (16.6 LMH) was approximately 80% higher than that of the TFC membrane (9.2 LMH), still maintaining the same level of NaCl salt rejection within the standard deviation. The maintenance of rejection suggested that the increase of water flux was not due to the membrane defect resulting from the addition of GO nanosheets. When the GO content exceeded 38 ppm, however, the water flux decreased, which may have occurred because of three factors: (1) the increase of the membrane hydrophilicity generally increases the water permeability (Barona, Lim et al. 2013), (2) a decrease of the active layer thickness also increases water permeability (Mason, Lonsdale 1990), and (3) a decrease of the membrane surface roughness decreases water permeability (Hirose, Ito et al. 1996). In Figure III-9 and 12, the increase in the hydrophilicity and decrease in the average thickness were substantial with the addition of only small amounts of GO nanosheets; however, the change became weaker with increasing GO content. In contrast, the average surface roughness decreased almost linearly with the GO content. Therefore, the combination of these property changes appeared to cause the net result of the water flux observed in Figure III-14.

In addition, the Figure III-15 showed the effect of GO fractionation on water permeability. The water flux was quite increased via just fractionation of GO nanosheets. The increment could be attributed to disappearance of abnormal

surface morphology which is too smooth (Figure III-2).

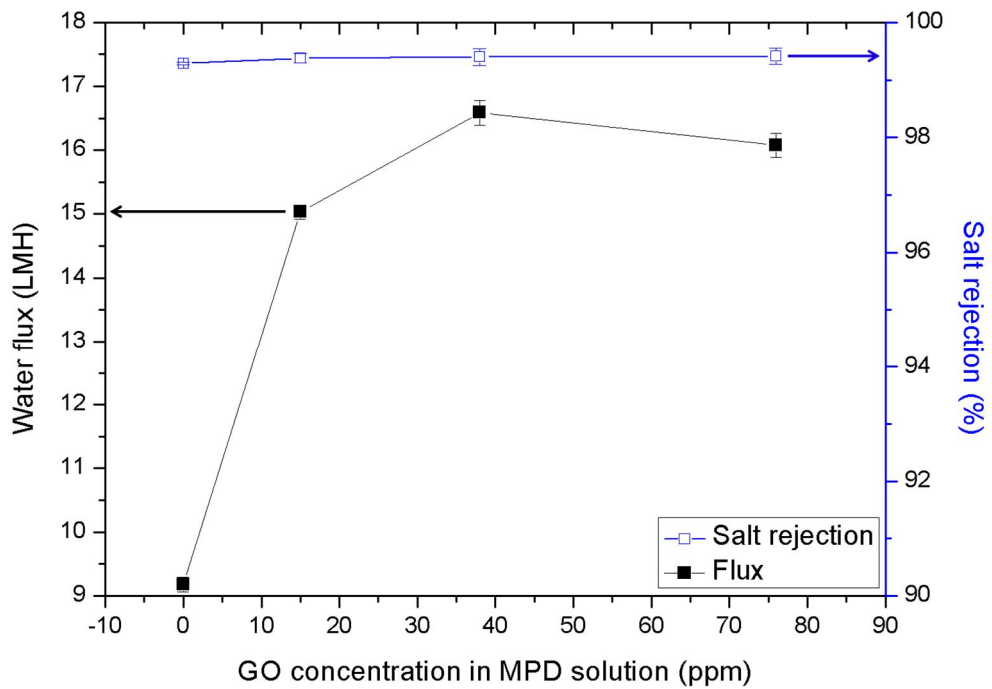


**Figure III-14. The water fluxes and salt rejections of the 0, 15, 38, and 76-GO-TFC membranes in a cross-flow filtration of 2000-ppm NaCl solution. Pre-filtration was conducted at 350 psi for 30 min to achieve membrane compaction before the main filtration, which was performed at 225 psi for 30 min.**

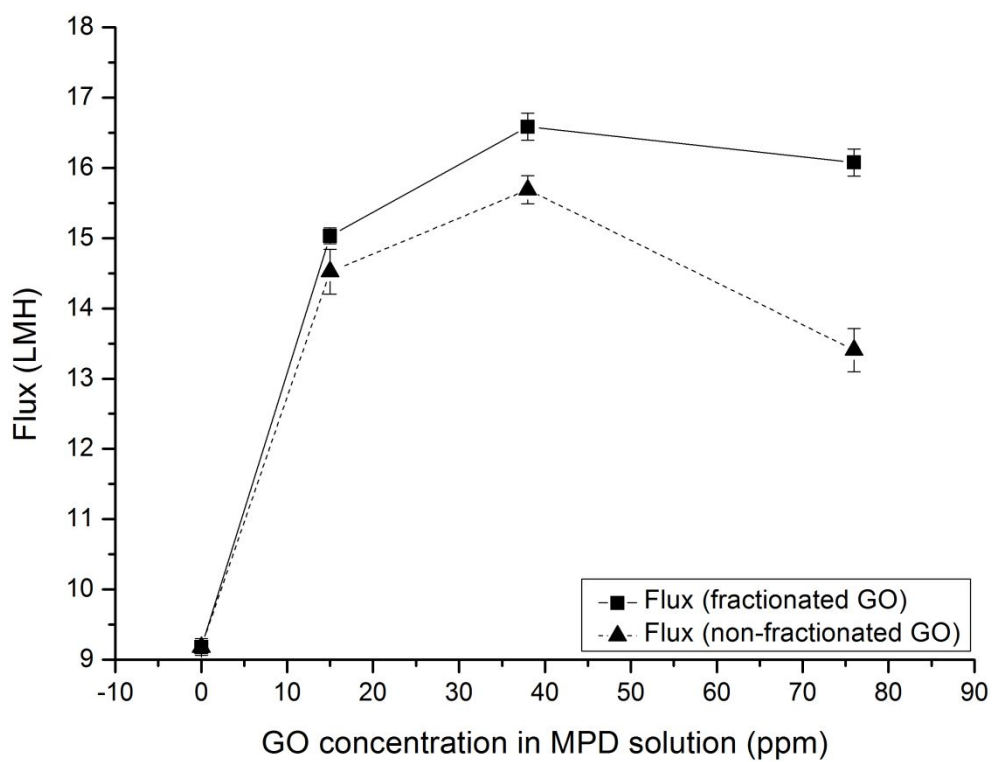


**Figure III-15. The water fluxes of the 0, 15, 38, and 76-GO-TFC membranes containing fractionated or non-fractionated GO nanosheets. The measurement condition was same as above.**

The anti-biofouling property of the GO-TFC membrane was evaluated by a cell attachment test. Based on the CLSM images, it was observed that the amount of cells attached on the membrane were substantially reduced as the GO content increased (Figure III-16a–d). Quantitatively, the biovolume of cells attached on the membrane decreased by approximately 98% with GO content (Figure III-16e). The enhanced anti-biofouling property of the GO-TFC membrane could be attributed to its hydrophilicity (Goosen, Sablani et al. 2004), negative charge (Bernstein, Belfer et al. 2011), and surface smoothness (Pang, Hong et al. 2005). In detail, the hydrophilicity would suppress the hydrophobic–hydrophobic interaction between bacteria and the membrane surface. A negatively charged membrane surface could generate electrostatic repulsions against negatively charged bacteria (Loosdrecht, Norde et al. 1990) and extracellular polymeric substance (EPS) (Costerton, Lewandowski et al. 1995) which is in close association with biofilm formation. The surface smoothness would result in less adhesion sites on the membrane surface.

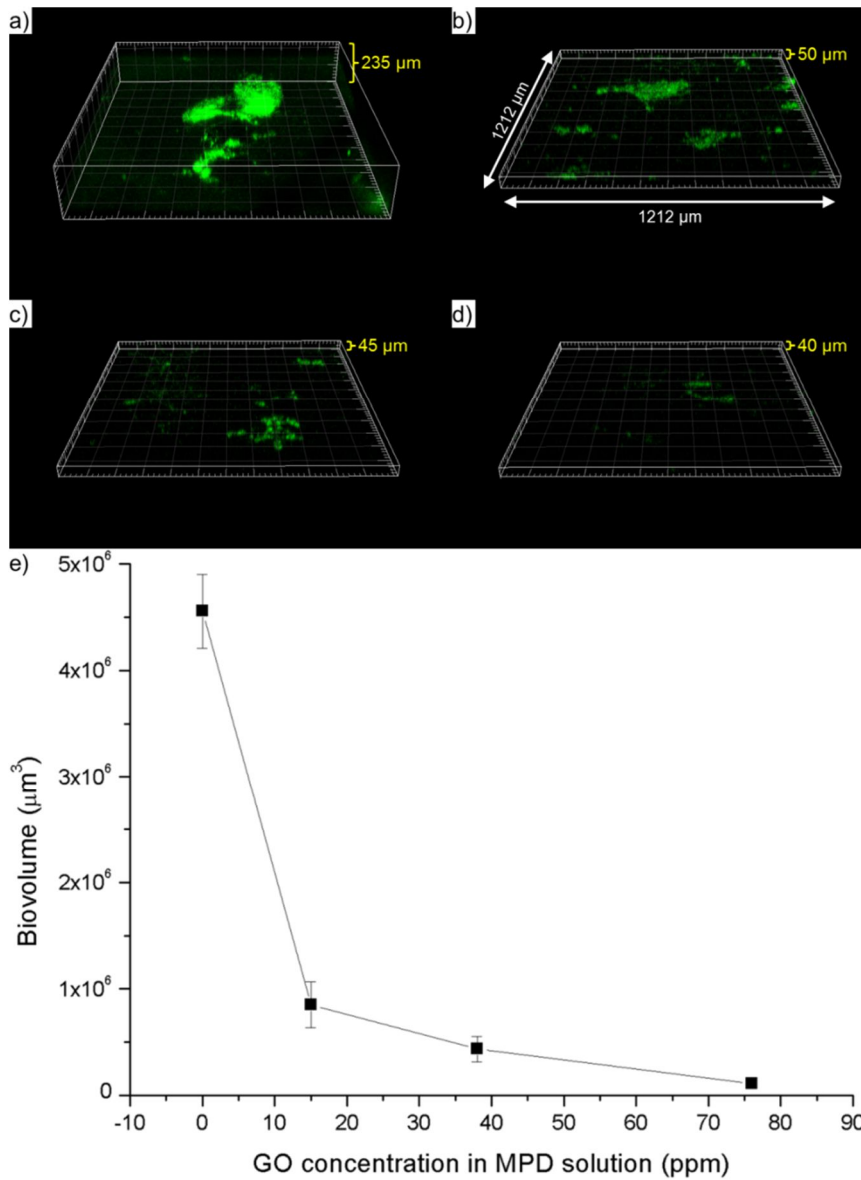


**Figure III-16. CLSM images of biofilm formed on the (a) 0, (b) 15, (c) 38, and (d) 76-GO-TFC membranes and (e) biovolume of cells attached on the membrane surface with corresponding GO content. GFP tagged PAO1 were cultured in a CDC reactor in which membranes containing various GO contents were set.**

The change in the salt rejection of the GO-TFC membrane is smaller than that of the TFC membrane after the chlorination. The salt rejection and water flux of the TFC membrane without GO nanosheets decreased from 99.3% to 91.1% and increased from 9.18 LMH to 32.5 LMH, respectively, after the chlorination (Figure III-17). The change in the membrane properties after the chlorination could arise from PA degradation caused by chlorine substitution (Glater, Hong et al. 1994). However, the salt rejection and water flux of the 76-GO-TFC membrane were almost maintained at the same level as those before the chlorination. The increased chlorine resistance of the 76-GO-TFC membrane might be attributed to hydrogen bonding between GO nanosheets and PA because the replacement of amidic hydrogen with chlorine (i.e., the first step of the chlorination (Glater, Hong et al. 1994)) could be impeded by the hydrogen bonding (Kim, Hyeon et al. 2013). In addition, the GO nanosheets could protect the underlying PA from chlorine attack (Choi, Choi et al. 2013).

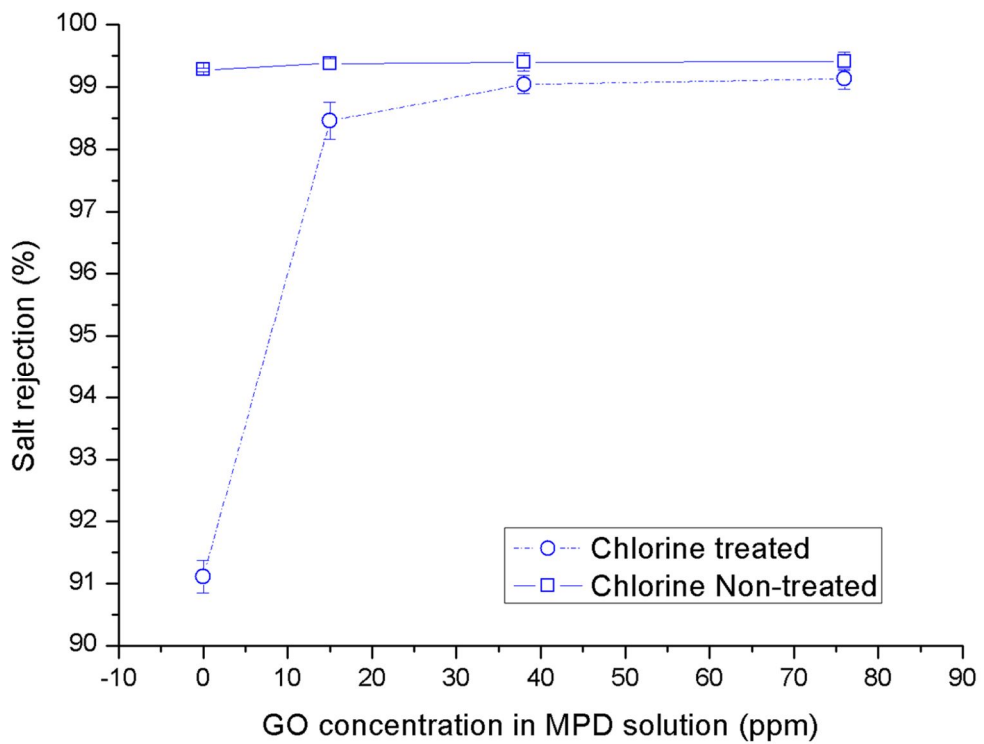


**Figure III-17. Salt rejections and water fluxes of the 0, 15, 38, and 76-GO-TFC membranes before and after chlorination which was conducted with a 2000-ppm NaOCl solution (pH 7) for 24 h.**

### **III.4. Conclusions**

GO nanosheets were embedded in the active layer of a TFC membrane by dispersing it into an MPD solution after fractionation. The embedment of GO nanosheets was then inferred by Raman spectrometer. The GO nanosheets enhanced the performance of the TFC membrane in terms of the water permeability, anti-biofouling property, and chlorine resistance by not only increasing the hydrophilicity and negative surface zeta potential but also decreasing the thickness and roughness of the active layer. Both the concentration and size of GO nanosheets substantially affected the performance of the GO-TFC membrane.

## **Chapter IV**

**Synergistic Effect of Graphene Oxide Nanosheets  
embedded in the Active and Support Layers on the  
performance of Thin-Film Composite Membranes**

## **IV.1. Introduction**

Seawater desalination is essential due to the water scarcity problem caused by the climate change (Oki, Kanae 2006, Veldkamp, Wada et al. 2015). Reverse osmosis (RO) is the most popular desalination technique (Greenlee, Lawler et al. 2009, Miller, Shemer et al. 2015), and most RO processes adopt thin-film composite (TFC) membranes. A TFC RO membrane has been developed over the past 30 years. However, it is still required to improve it in terms of permselectivity, anti-biofouling, and chlorine resistance (Clark, Allgeier et al. 1998, Escobar, Hoek et al. 2005). Biofouling that results in high operational cost is a major limiting factor of the RO process (Tiraferri, Vecitis et al. 2011, Kwak, Kim et al. 2001). Chlorine is very effective for reducing biofouling and thus is widely employed for cleaning membranes. However, it is difficult to directly apply chlorination to the RO processes because a common active layer of TFC membranes is polyamide (PA), which is very vulnerable to chlorine (Elimelech, Phillip 2011, Glater, Hong et al. 1994). Therefore, it is important to enhance both the anti-biofouling and chlorine resistance properties of a TFC membrane.

Recently, graphene oxide (GO) nanosheets have been utilized to modify TFC membranes due to its numerous hydrophilic functional groups (Kim, Hyeon et al. 2013, Perreault, Tousley et al. 2013, Choi, Choi et al. 2013, Chae, Lee et al. 2015, Yin, Zhu, et al. 2016). In some studies, the anti-biofouling property or chlorine resistance of a membrane were improved by coating GO nanosheets on the membrane surface as an active layer. However, this did not enhance water

permeability because the GO coating layer interfered with water permeation (Kim, Hyeon et al. 2013, Perreault, Tousley et al. 2013, Choi, Choi et al. 2013). In other studies, GO nanosheets were embedded in the PA active layer to reduce the resistance to water flow. This led to the enhancement in anti-biofouling, chlorine resistance as well as water permeability (Chae, Lee et al. 2015, Yin, Zhu, et al. 2016).

In this study, to further improve the TFC membrane properties GO nanosheets were embedded in both the PA active and polysulfone (PSf) support layers. A TFC membrane with embedded GO nanosheets in both the active and support layers (abbreviated as the AS-GO-TFC membrane) was prepared by adding GO nanosheets to the PSf solution, to fabricate a support layer and to the MPD aqueous solution, for interfacial polymerization of the PA layer. The AS-GO-TFC membrane was evaluated in terms of water permeability, salt rejection, anti-biofouling, and chlorine resistance using a lab-scale cross-flow filtration system.

## **IV.2. Experimental**

### **IV.2.1. Materials**

Graphite (Sigma-Aldrich, USA), potassium permanganate ( $\text{KMnO}_4$ , Sigma-Aldrich, USA), sulfuric acid ( $\text{H}_2\text{SO}_4$ , Daejung Chemical, Korea), nitric acid ( $\text{HNO}_3$ , DC Chemical, Korea), and hydrogen peroxide ( $\text{H}_2\text{O}_2$ , Junsei Chemical, Japan) were used to make GO nanosheets. Polysulfone (Solvay, Belgium), and 1-Methyl-2-pyrrolidinone (NMP, Sigma-Aldrich, USA) were used to prepare the PSf support layer of the TFC membrane. MPD (DuPont, USA), trimesoyl chloride (TMC, Sigma-Aldrich, USA), and isoparaffin (ISOL-C, SK Chemical, Korea) were used to fabricate the PA active layer of the TFC membrane. Sodium chloride ( $\text{NaCl}$ , Daejung, Korea), bovine serum albumin (BSA, Sigma-Aldrich, USA), and sodium hypochlorite ( $\text{NaOCl}$ , Daejung Chemical, Korea) were used to evaluate the membrane performance.

## **IV.2.2. Preparation of graphene oxide nanosheets**

GO nanosheets were prepared using chemical exfoliation of graphite on the basis of the Hummers method (Hummers, Offeman 1958). Graphitic oxide was made by oxidizing graphite using oxidants such as potassium permanganate, sulfuric acid, nitric acid, and hydrogen peroxide. The graphitic oxide solution was neutralized by replacing the acidic supernatant, obtained via centrifugation, with DI water several times. i) To embed the GO nanosheets in the PSf support layer, the DI water of the graphitic oxide solution was replaced with NMP using at least two periods of centrifugation. Then, graphitic oxides in NMP were converted to GO nanosheets using sonication at 563 W for 2 h. ii) To embed GO nanosheets in the PA active layer, the graphitic oxide in DI water was converted to GO nanosheets using the same sonication. Then, the sonicated GO nanosheets were fractionated using a track-etched membrane with a pore size of 3  $\mu\text{m}$  (Nuclepore, Whatman<sup>®</sup>, USA). This step was required because the GO nanosheets larger than 10  $\mu\text{m}$  can produce defects on the PA active layer. The small-sized fraction of the sonicated GO nanosheets was used to prepare the active layer embedded GO nanosheets.

### **IV.2.3. Preparation of GO-support layers**

The PSf support layers with embedded GO nanosheets (GO-support layer) were prepared via non-solvent induced phase separation. The aqueous GO solution was prepared as mentioned above, and PSf was dissolved in NMP. These solutions were prepared separately, to avoid the thermal reduction of GO nanosheets, and then mixed via shaking and stirring. In the solution mixture that contained both PSf and GO, the ratio of PSf to NMP was 0.176, and the ratio of GO to PSf was 0.0086. The solution was sonicated for 99 min to eliminate bubbles. After one day, the solution was cast on a polyester non-woven fabric using a micrometer film applicator (1117, SI, UK) that was immersed in DI water for 3 h. Additionally, the support layers without GO nanosheets (control support layer) were prepared as the control.

#### **IV.2.4. Preparation of GO-TFC membranes**

The GO-TFC membranes were prepared via interfacial polymerization using the GO-support or control support layer. A support layer was immersed into a 3 wt% MPD aqueous solution including GO nanosheets with 0, 38, 76, 114, or 152 ppm concentration for 1 min. The excess MPD solution remaining on the support layer was removed by squeezing it using a butadiene rubber roller for approximately 30 s. After 1 min of drying in the air, the support layer was immersed in a 0.04 w/v% TMC in ISOL-C for 1 min to make a PA active layer via interfacial polymerization. Finally, the GO-TFC membranes were dried in air for 10 min and were stabilized in DI water for 90 min.

As previously mentioned, the TFC membranes prepared by immersing the GO-support layer into the MPD solution with GO nanosheets (38–152 ppm) were abbreviated as the AS-GO-TFC membranes. The TFC membrane prepared using the GO-support layer and the MPD solution without GO nanosheets (0 ppm) was denoted as the S-GO-TFC membrane, which contained GO nanosheets only in its support layer. The TFC membranes prepared by immersing the control (no GO nanosheets) support layer into each MPD solution including the GO nanosheets (38–152 ppm) were designated as the A-GO-TFC membranes, which included GO nanosheets only in its active layer. Additionally, a TFC membrane containing GO nanosheets in neither active nor support layers was prepared as a control.

## **IV.2.5 Characterization of graphene oxide nanosheets**

The lateral size and thickness of the GO nanosheets were measured using a scanning probe microscope (SPM, INNV-BASE, VEECO, USA) with a cantilever tip (PPP-NCHR-10, NANOSENSORS, Switzerland). The GO solution was repeatedly dropped on a silicon wafer (4 WAFER P-100, Sehyoung wafer-tech, Korea). SPM measurements were performed after the residual water on the wafer had dried. To identify composition of GO nanosheets, the FTIR spectrum of the GO nanosheets was acquired using an FTIR spectrophotometer (Nicolet 6700, Thermo Scientific, USA) using a mass of dried GO nanosheets. The zeta potential of GO nanosheets in DI water was measured using a zeta-potential and particle-size analyzer (ELS-Z, Otsuka Electronics, Japan).

#### **IV.2.6. Characterization of the GO-support layers**

The contact angle, average pore size, and average surface roughness of the support layers were analyzed using the 24 hour dried samples. The contact angle was evaluated using a drop shape analysis system (DSA 100, KRÜSS, Germany) with a 5.0  $\mu\text{L}$  DI water drop using the sessile drop method. The average pore size of the support layers was examined using a capillary flow porometer (CFP-1500AEL, PMI, USA) with a wetting liquid (Galwick<sup>®</sup>, PMI, USA) using the ‘wet up-dry down’ method (Fang 2009, Jena, Gupta 2010). The average surface roughness of the support layers was measured using SPM with a cantilever tip. In addition, the surface zeta potential was measured using a zeta-potential/particle-size analyzer (ELS-Z1000, Otsuka Electronics, Japan) with a monitor solution (Otsuka Electronics, Japan).

### **IV.2.7. Characterization of the GO-TFC membranes**

GO nanosheets in the prepared GO-TFC membranes were investigated using Raman spectrometer (LabRam 300, Horiba Jobin Yvon, France). The Raman spectra of the TFC, S-GO-TFC, A-GO-TFC, and AS-GO-TFC membranes were acquired in a range from 1000 to 2000  $\text{cm}^{-1}$  with a 532 nm continuous wave laser, 100 $\times$  objective lens (N.A. = 0.90, Olympus, Japan), 0.5 mW data sample power, and 20 s sample acquisition time.

The average surface roughness, Ra, of the membranes was evaluated using a scanning probe microscope (SPM, INNV-BASE, Veeco, USA) with a cantilever tip (PPP-NCHR-10, Nanosensors, Switzerland). The SPM was operated in tapping mode at a 0.8 Hz scanning rate over the scan range of  $3.0 \times 3.0 \mu\text{m}^2$ .

The surface morphology was observed using a field-emission scanning electron microscope (FE-SEM, SUPRA 55VP, Carl Zeiss, Germany) after a platinum coating was deposited on the membranes with a platinum sputter coater (SCD 005, BAL-TEC, Germany) to examine changes in the ridge and valley structures.

The contact angle and surface zeta potential of the membranes were examined using the same method as the support layer characterization method mentioned above.

#### **IV.2.8. Evaluation of the GO-TFC membrane performance**

The membrane permselectivity of the TFC, S-GO-TFC, A-GO-TFC, and AS-GO-TFC membranes was evaluated using a lab-scale cross-flow filtration system. The filtration was conducted at 225 psi for 30 min with a 2000-ppm NaCl aqueous solution. The temperature was maintained at 25°C using a low-temperature bath/circulator (RW-0525G, Lab Companion, Korea). During the last 10 min of each run, both the water flux and salt rejection were measured.

The anti-biofouling property of membranes was evaluated using a cell attachment test in a cocurrent downflow contactor reactor (CDC reactor, BioSurface Technologies Corporation, USA). A green fluorescent protein (GFP) tagged *Pseudomonas aeruginosa* PAO1 was cultured in a 1/10 Tryptic Soy Broth (TSB, Becton, Dickinson and Company, USA) for 18 h at 37°C, which was diluted until the optical density reached 0.28. Then, the CDC reactor containing the samples of TFC, S-GO-TFC, A-GO-TFC, and AS-GO-TFC membranes was filled with 300 mL of 1/100 TSB and inoculated with the diluted PAO1. It was cultured at 25°C for 24 h with stirring at 80 rpm. Then, additional 1/100 TSB was continuously fed into the CDC reactor at a 1.4 mL/min flow rate for another 24 h. During the cultivation, light was blocked out by wrapping the reactor with aluminum foil to prevent the dissipation of fluorescence. Then, the images of cells attached on the membranes were taken using a confocal laser scanning microscope (CLSM, C1 Plus, Nikon, Japan). Using the CLSM data, the biovolume of the attached cells on the membranes was quantified with a software (image structure

analyzer-2, ISA-2) (Beyenal, Donovan et al. 2004). The graphical threshold for ISA-2 was determined automatically using Otsu's method (Otsu 1979). The anti-biofouling property of membranes was also evaluated using protein fouling test with BSA in cross-flow system. The filtration was conducted at 225 psi for 2 hours with 1 g/L BSA aqueous solution. The temperature was maintained at 25°C using a low-temperature bath/circulator. The decline rate of relative water flux with the operation time was calculated to assess the anti-biofouling property.

The chlorine resistance of the membranes was examined via the following procedure. 1) Each membrane was put on a glass plate, and its boundary was sealed using a silicon frame (gasket) to expose only the active layer of the membrane. An acrylic frame was placed on the silicon frame to evenly press the membrane. Then, all of them were bound with binder clips. 2) A 5000 ppm sodium hypochlorite solution was poured on the active layer in the frame. 3) After 16 h, the membranes were rinsed with DI water several times and then were immersed in DI water for 1 h. Then, the water flux and salt rejection of each chlorine-treated membrane were measured as mentioned above.

## **IV.3. Results and discussion**

### **IV.3.1. Characterization of the graphene oxide nanosheets**

The lateral size and thickness of the GO nanosheets were 100–200 nm and 1–2 nm, respectively (Figure IV-1). The thickness of the GO nanosheets implied that the prepared GO nanosheets were fully exfoliated single or double-layer GO nanosheets. The FTIR spectrum of GO nanosheets (Figure IV-2) verified the existence of O–H groups ( $3335\text{ cm}^{-1}$ ), C=O stretching vibration in carboxyl groups ( $1719\text{ cm}^{-1}$ ), unoxidized  $\text{sp}^2$  aromatic C=C bonds ( $1622\text{ cm}^{-1}$ ), C–O stretching vibration in epoxy groups ( $1224\text{ cm}^{-1}$ ), and C–O stretching vibration in alkoxy groups ( $1053\text{ cm}^{-1}$ ) (Wang, Wang et al. 2009, Wojtoniszak, Chen et al. 2012). The FTIR spectrum confirmed that graphene was successfully oxidized. In addition, The zeta potential of GO nanosheets was  $-46.8\text{ mV}$ . The negative charge was attributed to numerous carboxylate functional groups.

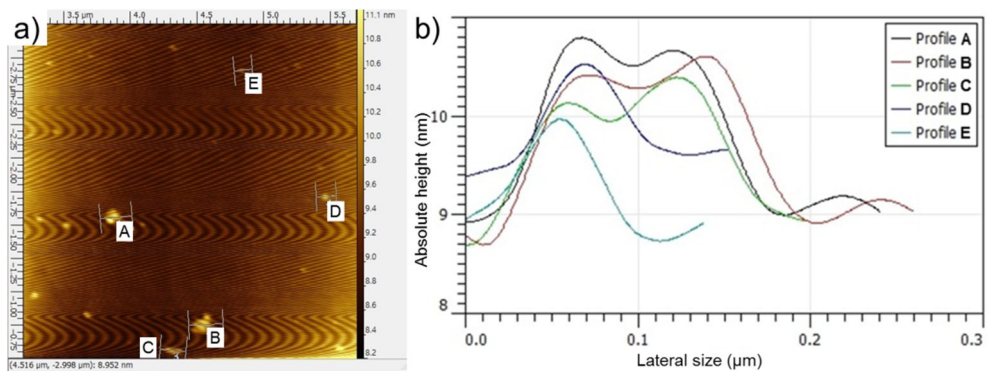


**Figure IV-1. (a) SPM image of the GO nanosheets on silicon wafer. The background wave is the wafer roughness. (b) The thickness was calculated as the difference between the maximum and minimum absolute heights. The wave pattern is due to the wafer roughness.**

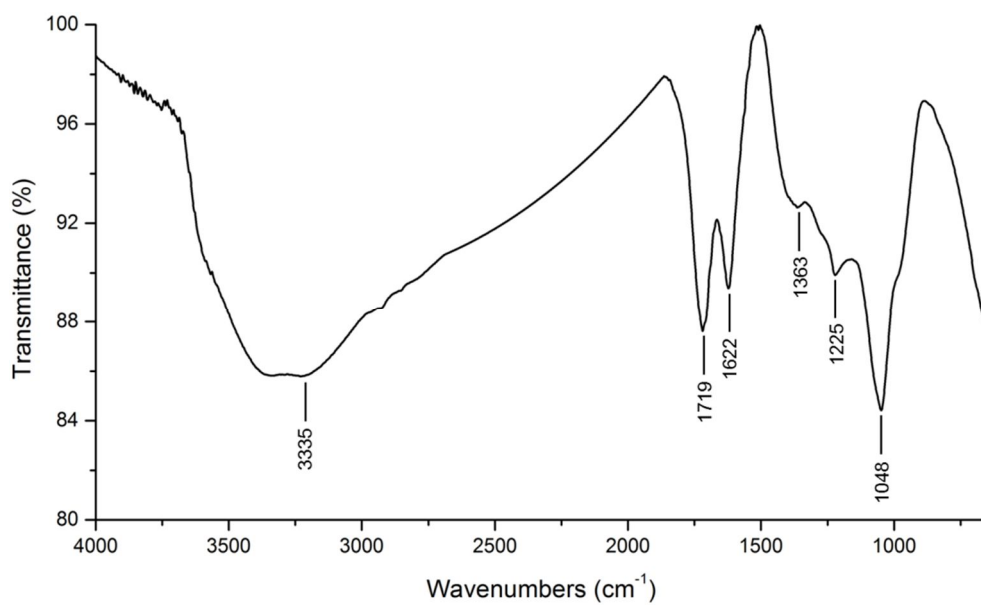


**Figure IV-2. FTIR spectrum of GO nanosheets.**

### **IV.3.2. Characterization of the GO-support layers**

The contact angle and surface zeta potential of the GO-support layer were 42° and -16 mV, respectively, whereas those of the control support layer without GO nanosheets were 59° and 0.6 mV, respectively (Figure IV-3). In other words, the GO-support layer was more hydrophilic and exhibited more negative zeta potential than the control support layer due to the functional groups of GO nanosheets. As shown in Figure IV-4, the average pore size and the average roughness of the GO-support layer were 27 nm and 25 nm, respectively, and they were larger than those of the control support layer. During the preparation of support layers, the demixing rate between the polymer solution and non-solvent (water) may increase due to hydrophilic GO nanosheets, which caused the pore size enhancement of the GO-support layers (Mulder 1996, Lee, Jang et al. 2015). In addition, the high surface roughness of GO-support layers might be attributed to the increased demixing rate in some parts between the polymer solution and non-solvent due to the dispersed GO. In detail, some tiny parts of polymer solution without GO would have conventional demixing rate whereas other parts of polymer solution containing GO might have higher demixing rate. Such unevenness might induce rougher surface of GO-support layers.

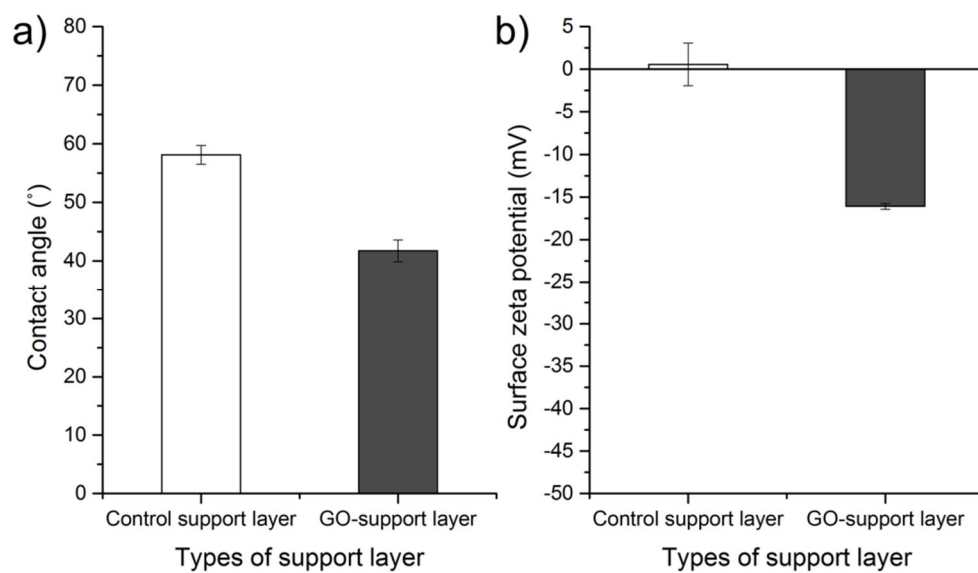


**Figure IV-3. (a) Contact angle (n=6) and (b) surface zeta potential (n=3) of the control support and GO-support layers.**

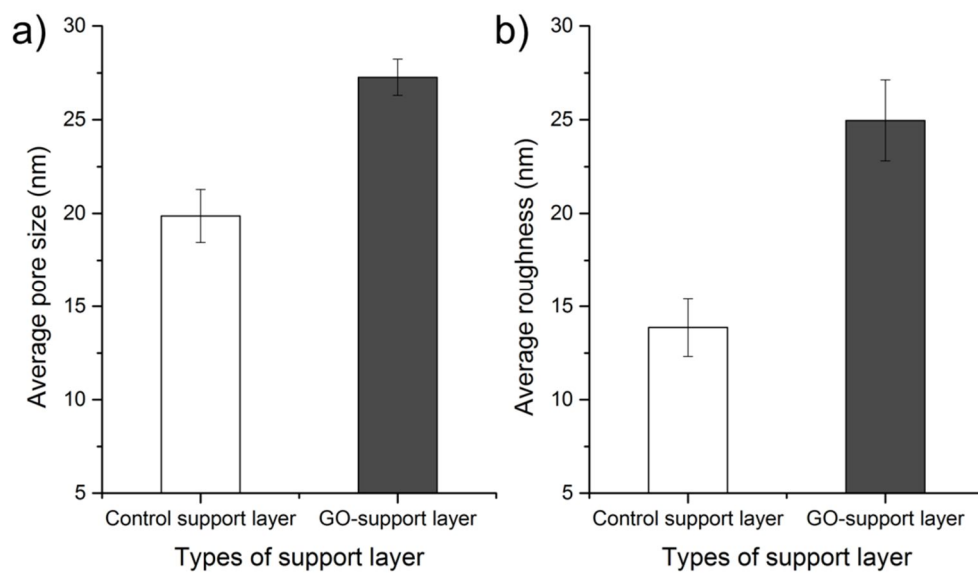


**Figure IV-4. Average pore size (n=3) and average surface roughness (n=9) of the control support and GO-support layers.**

### IV.3.3. Characterization of the GO-TFC membranes

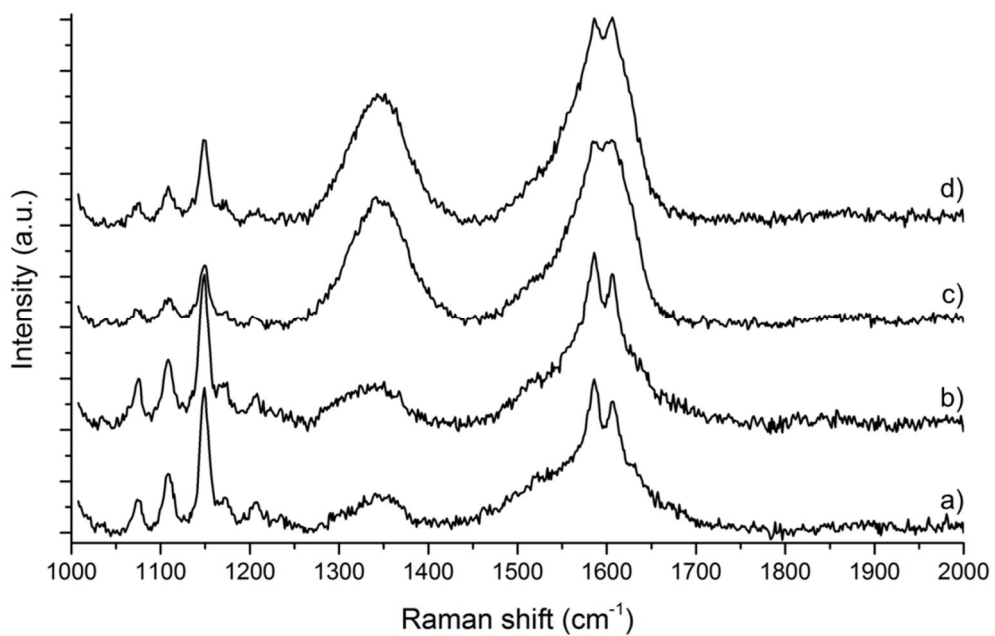
The existence of GO nanosheets in the TFC, S-GO-TFC, A-GO-TFC, and AS-GO-TFC membranes was investigated using Raman spectra (Figure IV-5). Figure IV-5a corresponds to the Raman spectrum of the TFC membranes without GO nanosheets. The Raman spectrum contained distinct PSf and PA bands (Figure IV-5a) (Deimede, Voyiatzis et al. 2000, Bader, Maenz et al. 2015).

Figure IV-5b shows the Raman spectrum of the S-GO-TFC membranes, which was similar to Figure IV-5a except that the broad band at 1350.7 and the doublet at around 1600  $\text{cm}^{-1}$  had slightly higher intensities than those of Figure IV-5a on the same base line: the peak intensities in Figure IV-5a and b at around 1350  $\text{cm}^{-1}$  were 765 and 936, respectively, and those at around 1600  $\text{cm}^{-1}$  were 2900 and 3467, respectively. GO nanosheet has characteristic peaks at around 1350 and 1600  $\text{cm}^{-1}$ , generally denoted as D and G peaks, respectively (Kudin, Ozbas et al. 2008). This suggests that GO nanosheets in the GO-support layer may result in the differences between Figure IV-5a and b.

The Raman spectrum of the A-GO-TFC membranes represented in Figure IV-5c indicates that the bands corresponding to D peak were significantly strengthened by embedding GO nanosheets in the active layer.

The Raman spectrum of the AS-GO-TFC membranes was similar to that of the A-GO-TFC membranes. However, the peak at 1600  $\text{cm}^{-1}$  was slightly higher than that of the A-GO-TFC membranes on the same base line (Figure IV-5d): the

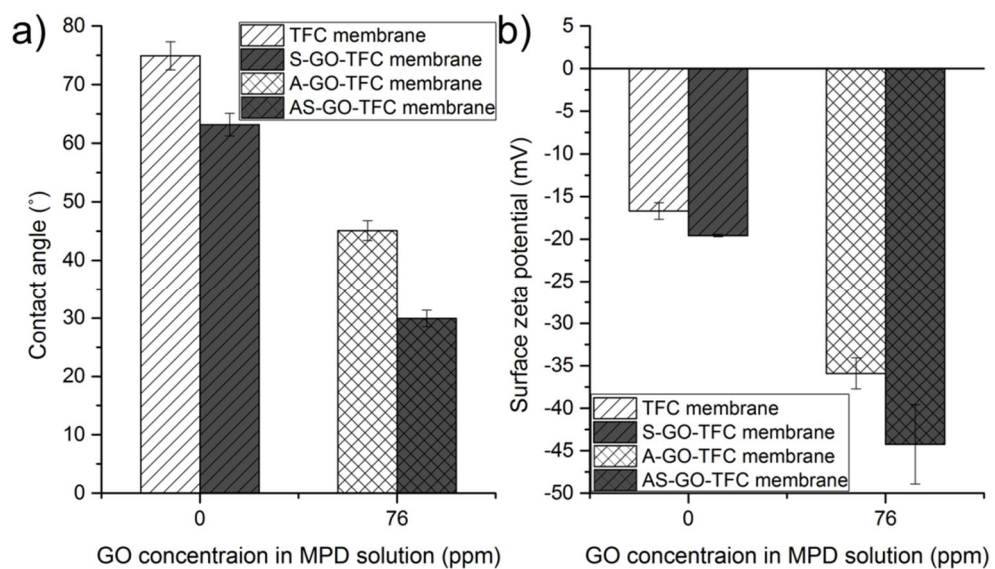
peak intensities at around  $1600\text{ cm}^{-1}$  of Figure IV-5c and d were 3650 and 4043, respectively. This confirmed that the AS-GO-TFC membranes contained GO nanosheets in both the support and active layers.



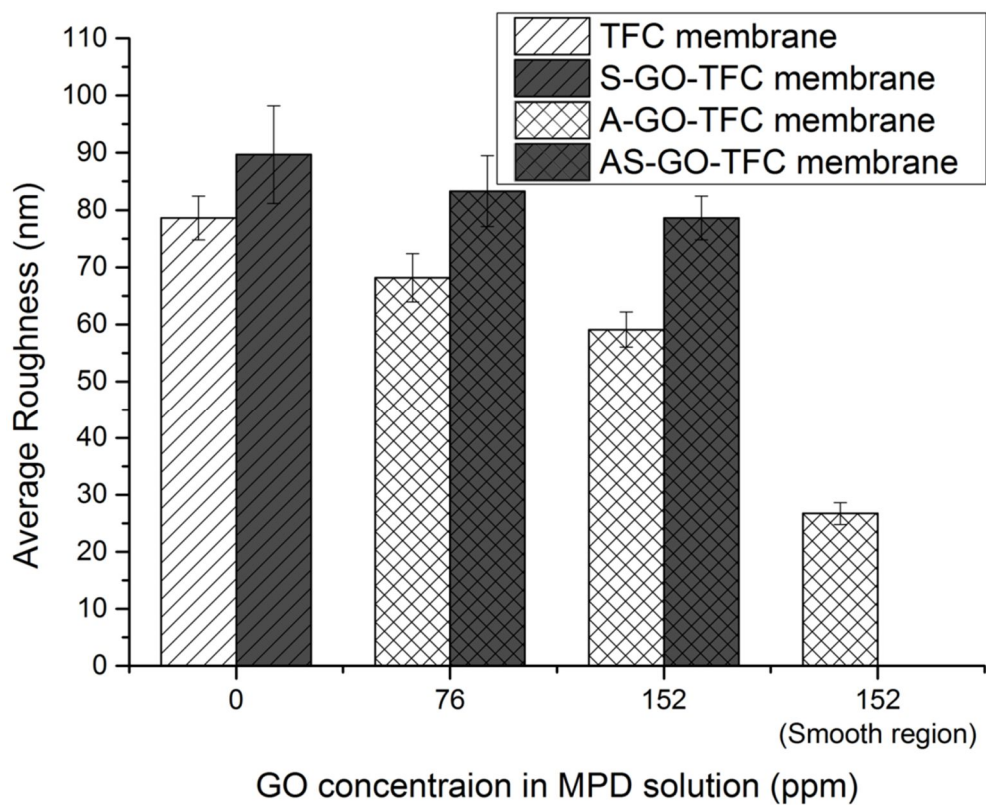
**Figure IV-5. Raman spectra of (a) TFC, (b) S-GO-TFC, (c) A-GO-TFC, and (d) AS-GO-TFC membranes (n=2). The GO concentration in MPD solutions for the A- and AS-GO-TFC membranes was 76 ppm.**

Figure IV-6 shows dramatic decreases in the contact angle and surface zeta potential of the membranes with increasing GO content in the active and/or support layers. Consequently, the AS-GO-TFC membrane was the most hydrophilic and negatively charged. These changes in hydrophilicity and surface charge would be advantageous to membrane performance in terms of water flux and salt rejection.

The average surface roughness of the membranes decreased with the increase of GO content in the active layer by raising GO concentration in MPD solution from 0 to 152 ppm (Figure IV-7). MPD diffusion, which led to ridge formation on the surface (Song, Sun et al. 2005), was retarded by the horizontally oriented GO nanosheets (Yang, Yang et al. 2014), causing the reduction in surface roughness. The roughness decrease generally lessens water permeability. However, as depicted by the grey bars (S- and AS-GO-TFC membranes) in Figure IV-7, the roughness was enhanced when the GO-support layers were utilized. That could originate from higher surface roughness of the GO-support layer (Figure IV-4b). As a result, the roughness values of the A-GO-TFC membranes were significantly lower than those of the TFC membranes, whereas the values for the AS-GO-TFC membranes were higher than those of the A-GO-TFC membranes and comparable to those of the TFC-membranes, as shown in Figure IV-7. This is a reason why embedding GO nanosheets in both the active and support layers is preferable.



**Figure IV-6. (a) Contact angle (n=6) and (b) surface zeta potential (n=3) of the TFC, S-GO-TFC, A-GO-TFC, and AS-GO-TFC membranes.**



**Figure IV-7. Average surface roughness of the TFC, S-GO-TFC, A-GO-TFC, and AS-GO-TFC membranes (n=5). The average surface roughness of smooth regions on the A-GO-TFC membrane with 152 ppm is also plotted.**

The SEM images in Figure IV-8 show the surface morphologies of the A- and AS-GO-TFC membranes. Locally, smoother areas (designated as ‘smooth regions’) were identified on the surface of the A-GO-TFC membranes, as shown in Figure IV-8a and 8c. A smooth region could be developed due to the aggregation of GO nanosheets: GO nanosheets might transversely adhere to each other above the critical aggregation concentration (Yang, Chang et al. 2010). The aggregated GO could interfere with MPD diffusion during interfacial polymerization, which resulted in small ridges that appeared as the smooth region. The roughness at the smooth region was significantly lower than the average value, as represented in Figure IV-7. However, there were almost no smooth regions found on the AS-GO-TFC membranes (Figure IV-8b). The GO-support layer prepared for AS-GO-TFC membranes might have higher affinity with GO nanosheets in MPD solution than did the control support layer because of the higher hydrophilicity of the GO-support layer. The affinity between GO nanosheets and the GO-support layer could be helpful for dispersing GO nanosheets and for preventing GO nanosheets from agglomerating together, resulting in rough regions almost entirely on the surface of AS-GO-TFC membranes.

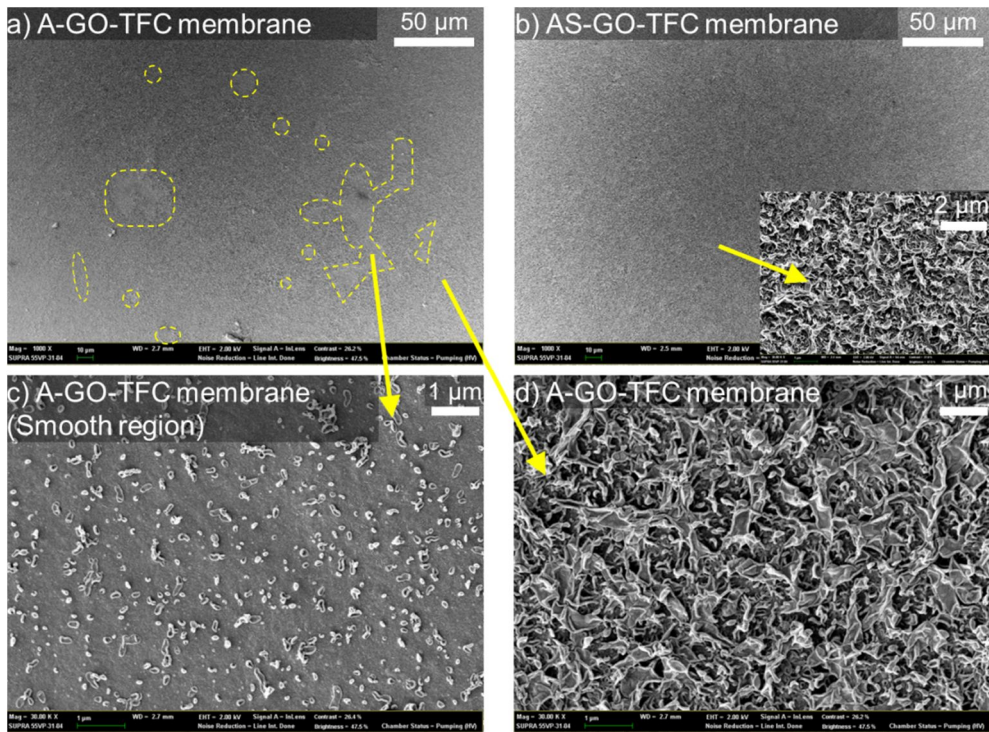


**Figure IV-8. SEM images of the (a) A-GO-TFC and (b) AS-GO-TFC membranes with 152 ppm of GO concentration in MPD solution at 1000× magnification, and of (c) a smooth region and (d) a rough region of A-GO-TFC at 30000× magnification. The dashed regions indicate the smooth regions.**

#### **IV.3.4. Performance of the GO-TFC membranes**

The water flux and salt rejection of the TFC membrane were improved by embedding GO nanosheets in the active and/or support layers (Figure IV-9). Figure IV-9a shows that the water fluxes of A-GO-TFC and AS-GO-TFC membranes were gradually enhanced when the GO content in an MPD solution increased from 0 to 76 ppm because of the increasing hydrophilicity (Barona, Lim et al. 2013). The AS-GO-TFC membranes had higher water flux than the A-GO-TFC membranes due to the higher hydrophilicity and surface roughness, as discussed above (Hirose, Ito et al. 1996). However, the water flux of the A-GO-TFC membranes was decreased when the GO content was greater than 76 ppm, whereas that of the AS-GO-TFC membranes was consistently increasing. The reduction in water flux at high GO concentration in the MPD solution would be attributed to the aggregation of GO nanosheets (Yin, Zhu, et al. 2016), similarly to other nanoparticles (Kim, Deng 2011, Yin, Kim et al. 2012, Huang, Qu et al. 2013), and the quite low surface roughness of smooth regions caused by the aggregation of GO nanosheets (Figure IV-8c). However, the water flux of the AS-GO-TFC membranes increased further because the smooth regions did not appear owing to high dispersity of GO nanosheets in MPD solution in using the GO-support layer. Due to such a synergistic effect of GO nanosheets embedded in both the active and support layers, the AS-GO-TFC membranes showed the highest water flux at 152 ppm, which was 19% and 70% higher than those of the A-GO-TFC and TFC membranes, respectively.

The salt rejection by TFC membranes can be explained by the Donnan exclusion (Mukherjee, Sharma et al. 2015) and homogeneous diffusion (Lonsdale, Merten et al. 1965). According to the Donnan exclusion model, the more negatively charged membrane has higher salt rejection due to charge repulsion between the Cl<sup>-</sup> ions and the membrane. Consequently, salt rejections of the more negatively charged A- and AS-GO-TFC membranes were higher than those of the less negatively charged TFC and S-GO-TFC membranes (Figure IV-9b). The homogeneous diffusion model describes salt rejection as the following equation.

$$S = 1 - \frac{J_2}{A \times J_1}$$

where S, J<sub>1</sub>, and J<sub>2</sub> are salt rejection, water flux, and salt flux, respectively. The equation implies that an increase of water flux causes enhancement of salt rejection when salt flux does not change much due to inducing dilution of the filtrate. The zeta potential of TFC and S-GO-TFC membrane were not significantly different, but the S-GO-TFC membrane had a higher water flux than the TFC membrane. This might be the reason why the S-GO-TFC membrane had higher salt rejection than the TFC membrane. In addition, the salt rejection of A- and AS-GO-TFC membranes were almost the same because of the similar zeta potential, but the salt rejections became slightly different upon increasing the GO content in the active layer. Such discrepancy between their salt rejections might be caused by the difference in their water fluxes.

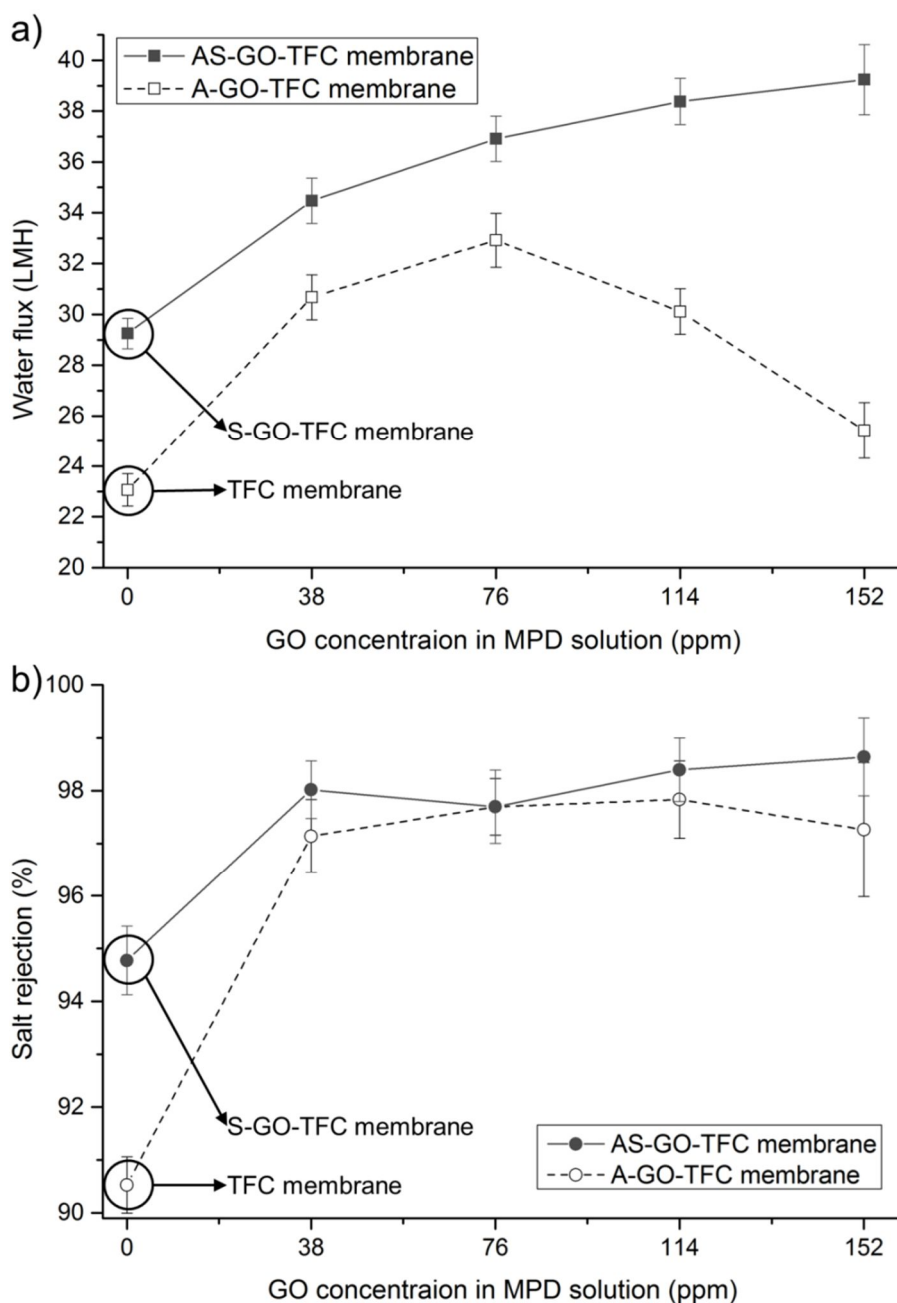


**Figure IV-9. (a) Water flux and (b) salt rejection of the TFC, S-GO-TFC, A-GO-TFC, and AS-GO-TFC membranes with 38, 76, 114, and 152 ppm of GO concentration in an MPD solution (n=3).**

In Figure IV-10, the water permeability and salt rejection of the AS-GO-TFC membranes developed in this study were quantitatively compared to those of various TFC membranes with one kind of nanoparticles embedded in their active and/or support layers without other additives which have been reported since 2012 (Kim, Choi et al. 2014, Yin, Zhu, et al. 2016, Barona, Lim et al. 2013, Bano, Mahmood et al. 2015, Zhao, Qiu et al. 2014, Huang, Qu et al. 2013, Kim, Hwang, et al. 2012). Only the data which exhibited water permeability over 1.0 L/m<sup>2</sup>·h·bar and salt rejections over 80% of at 2000 ppm NaCl feed solution were used for the comparison. As shown in Figure IV-10, the AS-GO-TFC membrane prepared in this study showed the highest salt rejection of about 99 %, and its water permeability was relatively higher among them. Consequently, the AS-GO-TFC membrane exhibited the best permselectivity among them according to the trade-off lines for water permeability and salt rejection. The water permeability and salt rejection were altered along the trade-off lines when the concentrations of MPD or TMC were changed.

The water flux and salt rejection data of the GO applied NF/RO membranes with NaCl feed solution were listed in Table IV-1. As shown in Table IV-1, GO was applied to the NF/RO membranes via layer-by-layer assembly (Hu, Mi 2013, Choi, Choi et al. 2013), embedment in an active layer (Yin, Zhu et al. 2016, Kim, Lim et al. 2015, Ali, Wang et al. 2016, Bano, Mahmood et al. 2015), or chemical grafting on a membrane surface (Hegab, Wimalasiri et al. 2015, Wang, Gao et al. 2015). The applications of GO to the NF/RO membranes increased water permeability of the membranes due to an increment of hydrophilicity.

The water permeability and salt rejection of the AS-GO-TFC membranes in this study were also compared to those of GO applied NF/RO membranes regardless of using other additives and measurement conditions (Figure IV-11). Only the data which exhibited water permeability over  $1.0 \text{ L/m}^2\cdot\text{h}\cdot\text{bar}$  and salt rejections over 80% of at 2000 ppm NaCl feed solution were used. Figure IV-11 confirmed that the AS-GO-TFC membranes exhibited the highest salt rejection and quite high permselectivity according to the trade-off lines among the NF/RO membranes applied GO.

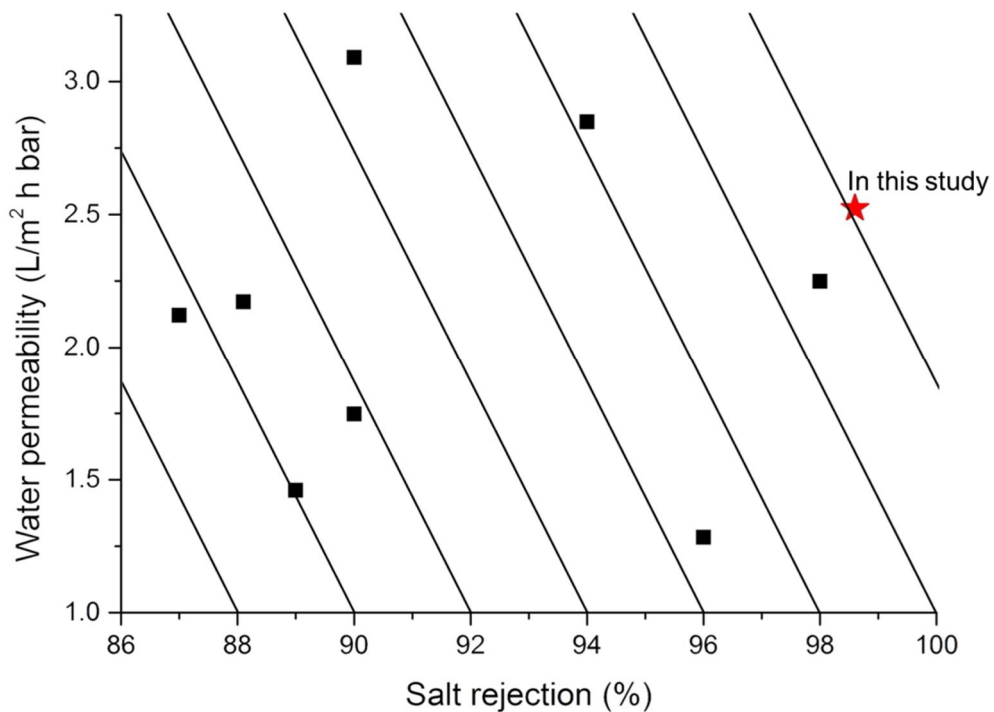


**Figure IV-10. Comparison of the water permeability and salt rejection of the AS-GO-TFC membrane (152 ppm of GO concentration in an MPD solution) prepared in this study to various reported TFC membranes with nanoparticles in their active layers. Only the data which exhibited water permeability over 1.0 L/m<sup>2</sup>·h·bar and salt rejections over 80% of at 2000 ppm NaCl feed solution were showed. The diagonal lines represents the trade-off lines for water permeability and salt rejection.**

**Table IV-1. The water flux and salt rejection of the NF/RO membranes applied GO.**

Application method	Other additives	Concentration of NaCl (ppm)	Pressure (bar)	Water flux (LMH)	Salt rejection (%)
Layer-by-layer assembly	✗	1168	3.4	69	19
Layer-by-layer assembly	○	2000	15.5	14	96
Embedment in active layer	✗	2000	20.7	59	94
Embedment in active layer	○	2000	15.5	59	96
Embedment in active layer	○	2000	15.0	30	98
Embedment in active layer	○	2000	15.0	22	88
Chemical grafting	✗	1500	14.0	61	96
Chemical grafting	✗	1000	15.0	24	69

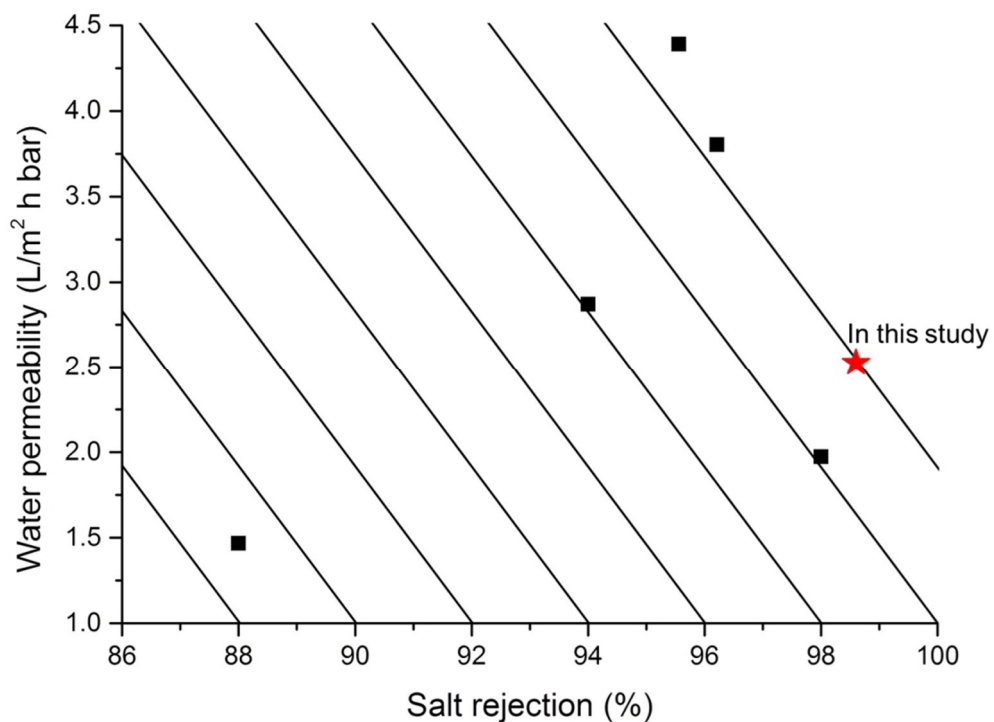


**Figure IV-11. Comparison of the water permeability and salt rejection of the AS-GO-TFC membrane (152 ppm of GO concentration in an MPD solution) prepared in this study to various reported GO applied NF/RO membranes. Only the data which exhibited water permeability over 1.0 L/m<sup>2</sup>·h·bar and salt rejections over 80% of at 2000 ppm NaCl feed solution were showed. The diagonal lines represents the trade-off lines for water permeability and salt rejection.**

Using CLSM images of various TFC membranes (Figure IV-12), their anti-biofouling properties were compared to one another in terms of a biovolume of biofilm on each membrane surface (Figure IV-13). As shown in Figure IV-12a–d, the amount of cells attached on the membrane was the least for the AS-GO-TFC membranes. The biovolumes of cells attached on the S-, A-, and AS-GO-TFC membranes were much less than that of the TFC membranes, respectively (Figure IV-13). Moreover, that of AS-GO-TFC membrane was 77% less than that of the A-GO-TFC membrane for 76 ppm of GO concentration in the MPD solution.

The changes in the relative water flux of the TFC and AS-GO-TFC (76 and 152 ppm of GO) membranes using 1 g/L BSA feed solution were shown in Figure IV-14. The relative water fluxes of the AS-GO-TFC membranes were declined less than that of the TFC membrane. In detail, the decrease of relative water flux was alleviated with increasing GO content in the active layer. Quantitatively, the decline rate of the relative water flux of the TFC and AS-GO-TFC (76 and 152 ppm of GO) membranes during the operation time were -0.1184, -0.0571, -0.0209  $\text{h}^{-1}$ , respectively. The decline of relative water flux of the AS-GO-TFC membranes with 76 and 152 ppm of GO in an active layer were mitigated by 52% and 82%, respectively. The result implied that the AS-GO-TFC membrane with 152 ppm of GO was 82% less fouled by BSA than the TFC membrane did.

The enhanced anti-biofouling property of the GO-TFC membranes could be attributed to its hydrophilicity (Goosen, Sablani et al. 2004) and negative surface zeta potential (Bernstein, Belfer et al. 2011). Specifically, hydrophilic surfaces are

less likely to be fouled by bacteria than hydrophobic surfaces are because the surface of bacteria (Rosenberg, Gutnick et al. 1980), including PAO1 (Kirisits, Prost et al. 2005), are relatively hydrophobic. A negatively charged membrane surface resulted in the electrostatic repulsion of negatively charged bacteria (Loosdrecht, Norde et al. 1990) and extracellular polymeric substance (Costerton, Lewandowski et al. 1995), which is closely associated with biofilm formation. In case of the AS-GO-TFC membrane, its surface roughness was higher than A-GO-TFC membrane, and this could cause more severe biofouling. However, the hydrophilicity and negative surface zeta potential of AS-GO-TFC membrane were much higher than those of A-GO-TFC membrane. Therefore, enhanced anti-biofouling property would originate from the sum of those effects.

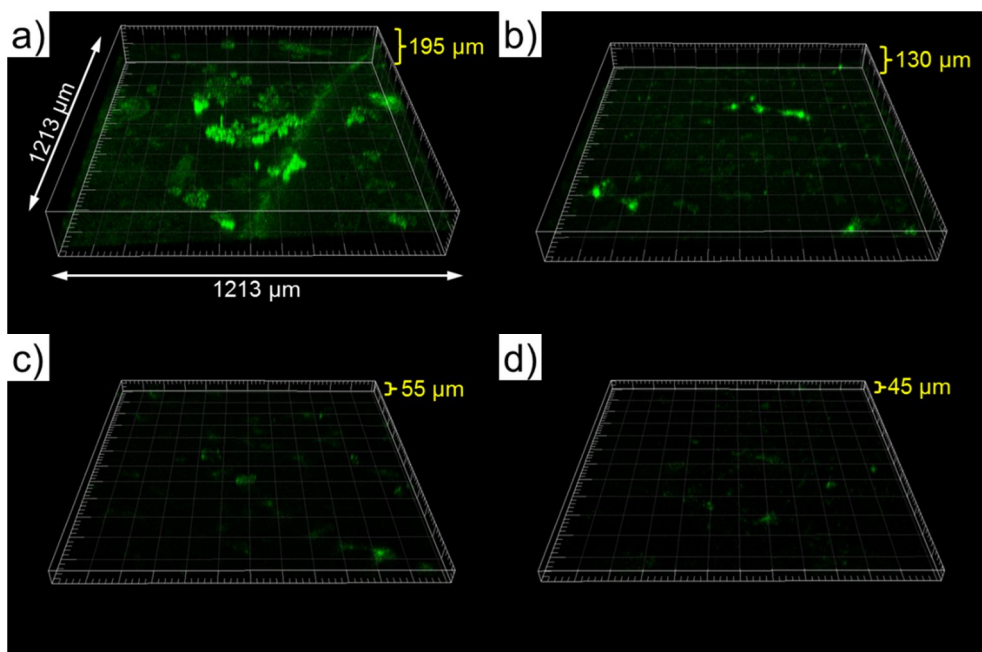


**Figure IV-12. CLSM images of biofilm formed on the (a) TFC, (b) S-GO-TFC, (c) A-GO-TFC, and (d) AS-GO-TFC membranes. The GO concentration in MPD solutions for the A- and AS-GO-TFC membranes was 76 ppm. Green color indicates microorganisms.**

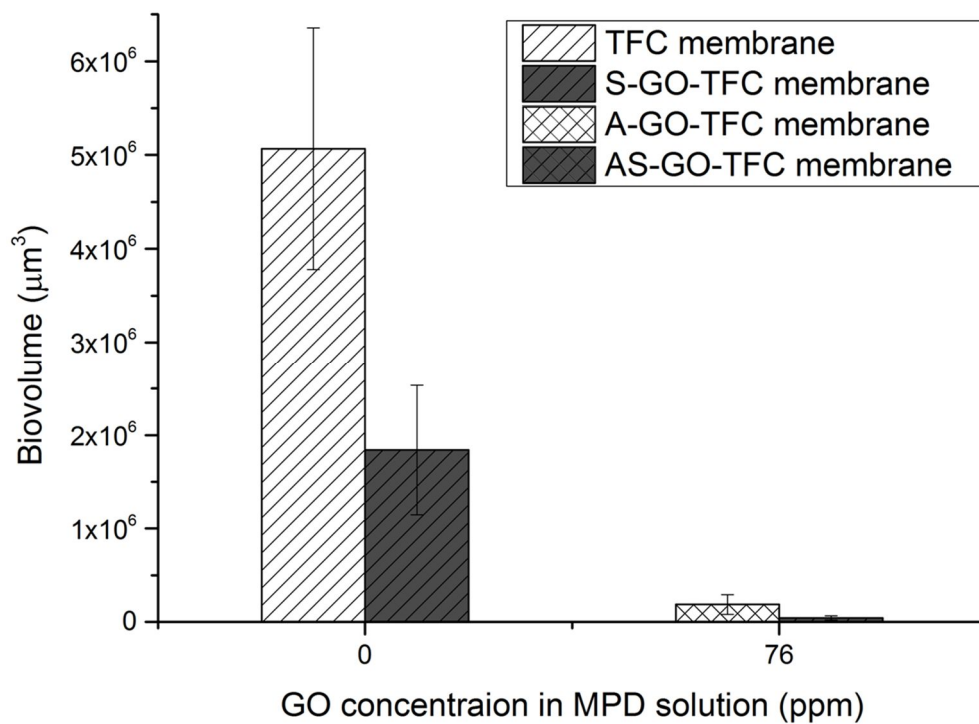


**Figure IV-13. The biovolume of cells attached on the TFC, S-GO-TFC, A-GO-TFC, and AS-GO-TFC membranes (n=9).**

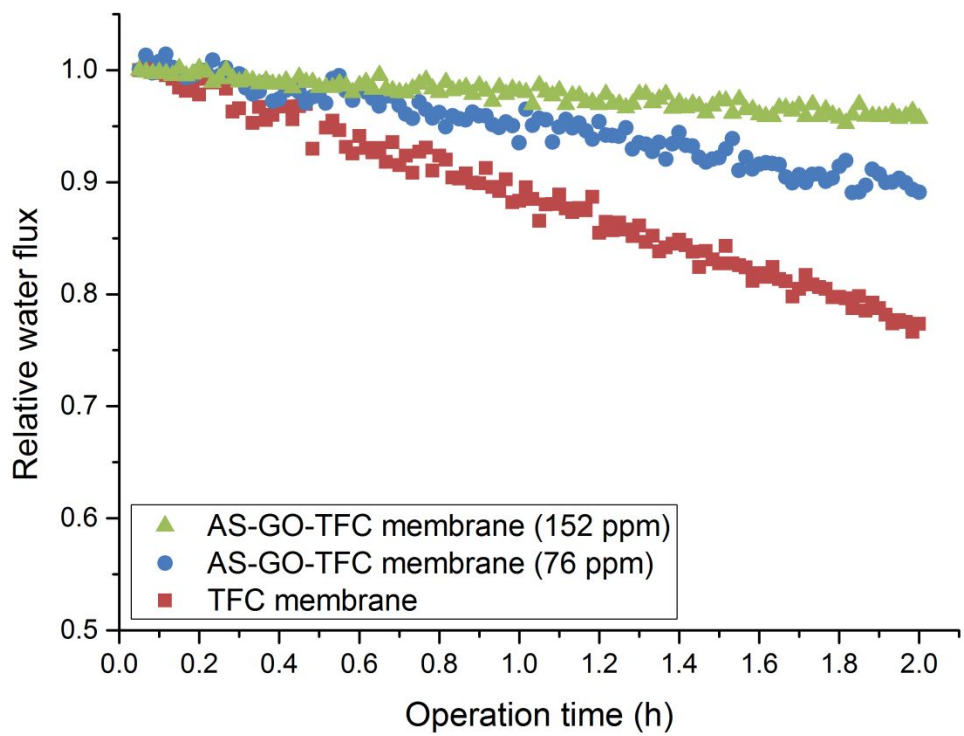


**Figure IV-14.** The plot of relative water fluxes of the TFC and AS-GO-TFC (76 and 152 ppm of GO) membranes with the operation time (n=3).

For the chlorine resistance, the changes in the water flux (Figure IV-15a) and salt rejection (Figure IV-15b) were compared before and after chlorine treatment. The changes in salt rejection of the TFC and S-GO-TFC membranes via chlorination were significant, whereas those of the A- and AS-GO-TFC membranes were relatively well maintained (Figure IV-15b). This means that the embedment of GO nanosheets in the active layer was very effective for the enhancement in chlorine resistance. Meanwhile, the changes by chlorine treatment for the TFC and S-GO-TFC membranes were similar to each other (12.9%p and 11.1%p, respectively), and those for the A- and AS-GO-TFC membranes were approximately the same between them (2.9%p and 2.1%p, respectively). Likewise, the considerable changes in the flux of the TFC and S-GO-TFC membranes were similar to each other (51.6 LMH and 51.3 LMH, respectively), and the changes in the flux of the A- and AS-GO-TFC membranes were approximately the same (15.2 LMH and 15.9 LMH, respectively) (Figure IV-15a). This suggests that embedding GO nanosheets in the active layer should be more significant for chlorine resistance than embedding GO nanosheets in the support layer.

The change in membrane properties after the chlorination results from PA degradation due to chlorine substitution (Glater, Hong et al. 1994). Nevertheless, the salt rejections of A- and AS-GO-TFC membranes were maintained after the chlorination. This chlorine resistance of A- and AS-GO-TFC membranes may arise from hydrogen bonding between the PA and GO nanosheets. The first step of PA chlorination is to replace amidic hydrogen with chlorine (Glater, Hong et al. 1994). The hydrogen bonding between PA and GO nanosheet can impede the replacement

(Kim, Hyeon et al. 2013). Moreover, GO nanosheets can protect the underlying PA from chlorine attack (Choi, Choi et al. 2013). Therefore, the GO nanosheets embedment in active layers was efficient in enhancing chlorine resistance of the TFC membranes.

In summary, the changes in the membrane properties and performances with respect to in which layer GO nanosheets were embedded were listed in Table IV-2.

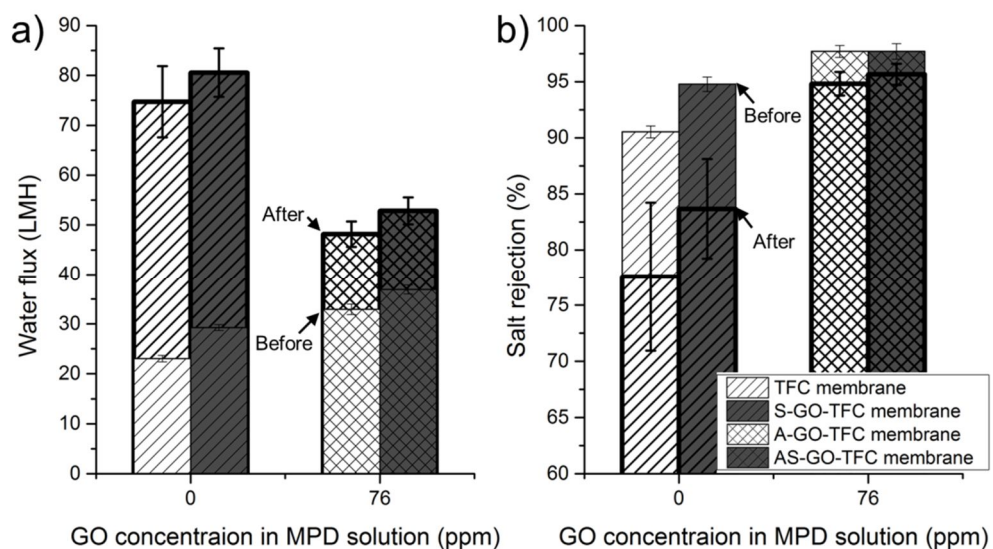


**Figure IV-15. Water fluxes and salt rejection of the TFC, S-GO-TFC, A-GO-TFC, and AS-GO-TFC membranes before and after chlorine treatment, which was conducted with 5000 ppm of NaOCl solution for 16 h (n=3). The thick boundaries indicate water fluxes and salt rejection after the chlorine treatment. The GO concentration in MPD solutions for the A- and AS-GO-TFC membranes was 76 ppm.**

Table IV-2. The summary of the changes in the membrane properties and performances depending on types of GO-TFC membrane.

Membrane properties	S-GO-TFC membrane	A-GO-TFC membrane	AS-GO-TFC membrane
Contact angle	↓	↓↓	↓↓↓
Surface zeta potential	↓	↓↓	↓↓↓
Surface roughness	↑	↓	⇒
Water permeability	↑	↑↑↘	↑↑↗
Salt rejection	↑	↑↑	↑↑↑
Anti-biofouling property	↑↑	↑↑↑	↑↑↑
Chlorine resistance	⇒	↑↑	↑↑

⇒: Comparable, ↑: Increased, ↓: Decreased,  
 ↗, ↘: Increased or decreased at high GO concentration

## **IV.4. Conclusions**

The embedment of GO nanosheets in both the active and support layers significantly increased the hydrophilicity, negative surface charge, and surface roughness of the AS-GO-TFC membranes compared with the A-GO-TFC membranes. Consequently, the water permeability, salt rejection, and anti-biofouling property of the AS-GO-TFC membranes were improved over the A-GO-TFC membranes even though the chlorine resistance of the AS-GO-TFC membranes was almost as much as that of the A-GO-TFC membranes. For AS-GO-TFC membranes, there were hardly any local smooth regions because the GO-support layer might be helpful to disperse GO nanosheets in MPD solution during polymerization of active layer, which was crucial for enhancing its water permeability.

# **Chapter V**

## **Conclusions**

## V.1. Conclusions

The prepared TFC membrane with GO nanosheets embedded in both the active and support layers exhibited outstanding permselectivity, anti-biofouling property, and chlorine resistance. The detail conclusions are as follows.

- The hydrophilicity and negative zeta potential of the AS-GO-TFC membrane were enhanced by numerous functional groups of the GO nanosheets embedded in both the active and support layers. In addition, its surface roughness was also increased due to high surface roughness of the GO-support layer.
- The water flux of the AS-GO-TFC membrane was notably improved compared with that of A-GO-TFC membrane. This is thought to be attributed to the increased hydrophilicity and surface roughness, and alleviation of GO aggregation due to the high affinity of a GO-support layer with GO nanosheets in MPD solution.
- The anti-biofouling property of the AS-GO-TFC membrane was dramatically enhanced compared with that of A-GO-TFC membrane because of further increment in hydrophilicity, and negative zeta potential.
- The chlorine resistance of the AS-GO-TFC membrane was similar to that of A-GO-TFC membrane because the chlorine resistances would result from the protection of PA by GO only in active layer.

## 국문 초록

최근 여러 연구에서 그래핀 옥사이드 코팅이 박막 복합 역삼투 분리막의 내염소성과 방오성(anti-biofouling)을 향상시킨 결과를 보고하였다. 하지만 그래핀 옥사이드 코팅층이 물의 흐름을 방해하여 수투수도를 증가시키기는 어려웠다. 이에 본 연구에서는, 물의 흐름 저하를 해소하기 위해 그래핀옥사이드를 박막 복합 역삼투 분리막 내에 분포시켰다. 그 후, 분리막의 성능을 평가하고 성능 향상의 요인을 조사하였다.

첫 번째로, 크기를 조정한 그래핀 옥사이드를 계면중합용 수용액에 첨가하여 그래핀 옥사이드를 활성층에 함유한 박막 복합 역삼투 분리막을 제조하였다. 그래핀 옥사이드를 활성층에 함유한 결과, 함유된 그래핀 옥사이드의 아민 단량체 확산 방해로 인해 분리막의 표면 거칠기는 감소하였으나 그래핀 옥사이드의 기능기로 인해 분리막의 친수성과 음전하도가 증가하였다. 그 결과, 분리막의 내염소성과 방오성뿐만 아니라 수투수도 현격히 증가하였다.

두 번째로, 그래핀 옥사이드를 계면중합용 수용액과 지지층 고분자 용액 첨가하여 그래핀 옥사이드를 활성층과 지지층에도 함유한 박막 복합 역삼투 분리막을 제조하였다. 그래핀 옥사이드를 지지층에 함유한 결과, 그래핀 옥사이드의 기능기와 그래핀 옥사이드 함유 지지층의 커진

공극 크기로 인해 분리막의 친수성, 음전하도, 그리고 표면 거칠기까지 추가로 증가하였다. 또한 그래핀 옥사이드 함유 지지층은 계면중합용 수용액 속의 그래핀 옥사이드를 더 분산시켰다. 이로 인해, 그래핀 옥사이드를 양 층 모두에 함유한 분리막의 수투수도와 방오성이 활성층에만 함유한 경우에 비해 크게 증가하였다.

그래핀 옥사이드를 박막 복합 분리막 양 층에 함유시켜 분리막의 수투수도, 염제거율, 내염소성, 방오성을 성공적으로 개선한 결과는, 이 기술을 실제 역삼투 공정이나 다양한 환경공학적인 시스템 적용할 가능성이 있음을 보여주었다.

**주요어:** 박막 복합 분리막, 역삼투, 그래핀 옥사이드, 나노복합, 방오성, 내염소성

**학번:** 2010-23334

## Reference

- Ahn, J.-H., and Hong, B. H. (2014). Graphene for displays that bend. *Nature Nanotechnology*, 9(10), 737-738.
- Aizawa, T., Souda, R., Otani, S., Ishizawa, Y., and Oshima, C. (1990). ANOMALOUS BOND OF MONOLAYER GRAPHITE ON TRANSITION-METAL CARBIDE SURFACES. *Physical Review Letters*, 64(7), 768-771.
- Ali, M. E. A., Wang, L., Wang, X., and Feng, X. (2016). Thin film composite membranes embedded with graphene oxide for water desalination. *Desalination*, 386, 67-76.
- Amirilargani, M., Saljoughi, E., Mohammadi, T., and Moghbeli, M. R. (2010). Effects of Coagulation Bath Temperature and Polyvinylpyrrolidone Content on Flat Sheet Asymmetric Polyethersulfone Membranes. *Polymer Engineering and Science*, 50(5), 885-893.
- Arthanareeswaran, G., Thanikaivelan, P., Raguime, J. A., Raajenthiren, M., and Mohan, D. (2007). Metal ion separation and protein removal from aqueous solutions using modified cellulose acetate membranes: Role of polymeric additives. *Separation and Purification Technology*, 55(1), 8-15.
- Bader, M., Maenz, T., Schmiederer, D., Kuehnert, I., Leuteritz, A., and Heinrich, G. (2015). Correlation Between Morphological Properties and Thermal

- Conductivity of Injection-Molded Polyamide 46. *Polymer Engineering and Science*, 55(10), 2231-2236.
- Bae, T.-H., Kim, I.-C., and Tak, T.-M. (2006). Preparation and characterization of fouling-resistant TiO<sub>2</sub> self-assembled nanocomposite membranes. *Journal of Membrane Science*, 275(1–2), 1-5.
- Baker, R. W. (2004). *Membrane Technology and Applications*, John Wiley & Sons, Ltd.
- Balandin, A. A., Ghosh, S., Bao, W., Calizo, I., Teweldebrhan, D., Miao, F., and Lau, C. N. (2008). Superior thermal conductivity of single-layer graphene. *Nano Letters*, 8(3), 902-907.
- Bano, S., Mahmood, A., Kim, S.-J., and Lee, K.-H. (2015). Graphene oxide modified polyamide nanofiltration membrane with improved flux and antifouling properties. *Journal of Materials Chemistry A*, 3(5), 2065-2071.
- Baroña, G. N. B., Choi, M., and Jung, B. (2012). High permeate flux of PVA/PSf thin film composite nanofiltration membrane with aluminosilicate single-walled nanotubes. *Journal of Colloid and Interface Science*, 386(1), 189-197.
- Barona, G. N. B., Lim, J., Choi, M., and Jung, B. (2013). Interfacial polymerization of polyamide-aluminosilicate SWNT nanocomposite membranes for reverse osmosis. *Desalination*, 325, 138-147.
- Bartels, C. R. (1989). A SURFACE SCIENCE INVESTIGATION OF

COMPOSITE MEMBRANES. *Journal of Membrane Science*, 45(3), 225-245.

Ben-Sasson, M., Zodrow, K. R., Genggeng, Q., Kang, Y., Giannelis, E. P., and Elimelech, M. (2014). Surface Functionalization of Thin-Film Composite Membranes with Copper Nanoparticles for Antimicrobial Surface Properties. *Environmental Science & Technology*, 48(1), 384-393.

Berger, C., Song, Z., Li, X., Wu, X., Brown, N., Naud, C., Mayou, D., Li, T., Hass, J., Marchenkov, A. N., Conrad, E. H., First, P. N., and de Heer, W. A. (2006). Electronic confinement and coherence in patterned epitaxial graphene. *Science*, 312(5777), 1191-1196.

Bernstein, R., Belfer, S., and Freger, V. (2011). Bacterial Attachment to RO Membranes Surface-Modified by Concentration-Polarization-Enhanced Graft Polymerization. *Environmental Science & Technology*, 45(14), 5973-5980.

Beyenal, H., Donovan, C., Lewandowski, Z., and Harkin, G. (2004). Three-dimensional biofilm structure quantification. *Journal of Microbiological Methods*, 59(3), 395-413.

Boehm, S. (2014). Graphene against corrosion. *Nature Nanotechnology*, 9(10), 741-742.

Bolotin, K. I., Sikes, K. J., Jiang, Z., Klima, M., Fudenberg, G., Hone, J., Kim, P., and Stormer, H. L. (2008). Ultrahigh electron mobility in suspended

graphene. *Solid State Communications*, 146(9-10), 351-355.

Bonaccorso, F., Colombo, L., Yu, G., Stoller, M., Tozzini, V., Ferrari, A. C., Ruoff, R. S., and Pellegrini, V. (2015). Graphene, related two-dimensional crystals, and hybrid systems for energy conversion and storage. *Science*, 347(6217).

Buchsteiner, A., Lerf, A., and Pieper, J. (2006). Water dynamics in graphite oxide investigated with neutron scattering. *Journal of Physical Chemistry B*, 110(45), 22328-22338.

Cadotte, J. E., Petersen, R. J., Larson, R. E., and Erickson, E. E. (1980). NEW THIN-FILM COMPOSITE SEAWATER REVERSE-OSMOSIS MEMBRANE. *Desalination*, 32(1-3), 25-31.

Calado, V. E., Schneider, G. F., Theulings, A. M. M. G., Dekker, C., and Vandersypen, L. M. K. (2012). Formation and control of wrinkles in graphene by the wedging transfer method. *Applied Physics Letters*, 101(10), 103116.

Chae, H.-R., Lee, J., Lee, C.-H., Kim, I.-C., and Park, P.-K. (2015). Graphene oxide-embedded thin-film composite reverse osmosis membrane with high flux, anti-biofouling, and chlorine resistance. *Journal of Membrane Science*, 483, 128-135.

Chae, S. J., Güneş, F., Kim, K. K., Kim, E. S., Han, G. H., Kim, S. M., Shin, H.-J., Yoon, S.-M., Choi, J.-Y., Park, M. H., Yang, C. W., Pribat, D., and Lee, Y. H.

- (2009). Synthesis of Large-Area Graphene Layers on Poly-Nickel Substrate by Chemical Vapor Deposition: Wrinkle Formation. *Advanced Materials*, 21(22), 2328-2333.
- Chan, E. P., Lee, J.-H., Chung, J. Y., and Stafford, C. M. (2012). An automated spin-assisted approach for molecular layer-by-layer assembly of crosslinked polymer thin films. *Review of Scientific Instruments*, 83(11), 114102.
- Chan, E. P., Young, A. P., Lee, J.-H., and Stafford, C. M. (2013). Swelling of Ultrathin Molecular Layer-by-Layer Polyamide Water Desalination Membranes. *Journal of Polymer Science Part B: Polymer Physics*, 51(22), 1647-1655.
- Choi, J.-H., Jegal, J., and Kim, W.-N. (2006). Fabrication and characterization of multi-walled carbon nanotubes/polymer blend membranes. *Journal of Membrane Science*, 284(1-2), 406-415.
- Choi, W., Choi, J., Bang, J., and Lee, J.-H. (2013). Layer-by-Layer Assembly of Graphene Oxide Nanosheets on Polyamide Membranes for Durable Reverse-Osmosis Applications. *Acs Applied Materials & Interfaces*, 5(23), 12510-12519.
- Chuang, W. Y., Young, T. H., Chiu, W. Y., and Lin, C. Y. (2000). The effect of polymeric additives on the structure and permeability of poly(vinyl alcohol) asymmetric membranes. *Polymer*, 41(15), 5633-5641.
- Clark, M. M., Allgeier, S., Amy, G., Chellam, S., DiGiano, F., Elimelech, M.,

- Freeman, S., Jacangelo, J., Jones, K., Laine, J. M., Lozier, J., Marinas, B., Riley, R., Taylor, J., Thompson, M., Vickers, J., Wiesner, M., Zander, A., and Comm, A. M. T. R. (1998). Committee report: Membrane processes. *Journal American Water Works Association*, 90(6), 91-105.
- Compton, O. C., and Nguyen, S. T. (2010). Graphene oxide, highly reduced graphene oxide, and graphene: versatile building blocks for carbon-based materials. *Small*, 6.
- Congjie, G. (2003). Development and extension of seawater desalination by reverse osmosis. *Chinese Journal of Oceanology and Limnology*, 21(1), 40-45.
- Coronell, O., Mariñas, B. J., and Cahill, D. G. (2011). Depth Heterogeneity of Fully Aromatic Polyamide Active Layers in Reverse Osmosis and Nanofiltration Membranes. *Environmental Science & Technology*, 45(10), 4513-4520.
- Corry, B. (2008). Designing Carbon Nanotube Membranes for Efficient Water Desalination. *The Journal of Physical Chemistry B*, 112(5), 1427-1434.
- Costerton, J. W., Lewandowski, Z., Caldwell, D. E., Korber, D. R., and Lappinscott, H. M. (1995). MICROBIAL BIOFILMS. *Annual Review of Microbiology*, 49, 711-745.
- Dato, A., Radmilovic, V., Lee, Z., Phillips, J., and Frenklach, M. (2008). Substrate-free gas-phase synthesis of graphene sheets. *Nano Letters*, 8(7), 2012-2016.

- Deimede, V., Voyiatzis, G. A., Kallitsis, J. K., Qingfeng, L., and Bjerrum, N. J. (2000). Miscibility behavior of polybenzimidazole/sulfonated polysulfone blends for use in fuel cell applications. *Macromolecules*, 33(20), 7609-7617.
- Díez-Betriu, X., Mompeán, F. J., Munuera, C., Rubio-Zuazo, J., Menéndez, R., Castro, G. R., and de Andrés, A. (2014). Graphene-oxide stacking and defects in few-layer films: Impact of thermal and chemical reduction. *Carbon*, 80, 40-49.
- Dikin, D. A., Stankovich, S., Zimney, E. J., Piner, R. D., Dommett, G. H. B., Evmenenko, G., Nguyen, S. T., and Ruoff, R. S. (2007). Preparation and characterization of graphene oxide paper. *Nature*, 448(7152), 457-460.
- Ding, C., Yin, J., and Deng, B. (2014). Effects of Polysulfone (PSf) Support Layer on the Performance of Thin-Film Composite (TFC) Membranes. *Journal of chemical and process engineering*, 1, 1-8.
- Dreyer, D. R., Park, S., Bielawski, C. W., and Ruoff, R. S. (2010). The chemistry of graphene oxide. *Chemical Society Reviews*, 39(1), 228-240.
- Eizenberg, M., and Blakely, J. M. (1979). CARBON MONOLAYER PHASE CONDENSATION ON NI(111). *Surface Science*, 82(1), 228-236.
- Elimelech, M., and Phillip, W. A. (2011). The Future of Seawater Desalination: Energy, Technology, and the Environment. *Science*, 333(6043), 712-717.
- Escobar, I. C., Hoek, E. M., Gabelich, C. J., DiGiano, F. A., Le Gouellec, Y. A.,

Berube, P., Howe, K. J., Allen, J., Atasi, K. Z., Benjamin, M. M., Brandhuber, P. J., Brant, J., Chang, Y. J., Chapman, M., Childress, A., Conlon, W. J., Cooke, T. H., Crossley, I. A., Crozes, G. F., Huck, P. M., Kommineni, S. N., Jacangelo, J. G., Karimi, A. A., Kim, J. H., Lawler, D. F., Li, Q. L., Schideman, L. C., Sethi, S., Tobiasson, J. E., Tseng, T., Veerapanemi, S., Zander, A. K., and Comm, A. M. T. R. (2005). Committee Report: Recent advances and research needs in membrane fouling. *Journal American Water Works Association*, 97(8), 79-89.

Fang, Y. (2009). Pore size characterization of monolithic capillary columns using capillary flow porometry. Brigham Young University, Provo.

Feinberg, B. J., Ramon, G. Z., and Hoek, E. M. V. (2013). Thermodynamic Analysis of Osmotic Energy Recovery at a Reverse Osmosis Desalination Plant. *Environmental Science & Technology*, 47(6), 2982-2989.

Fontananova, E., Jansen, J. C., Cristiano, A., Curcio, E., and Drioli, E. (2006). Effect of additives in the casting solution on the formation of PVDF membranes. *Desalination*, 192(1-3), 190-197.

Freger, V. (2003). Nanoscale Heterogeneity of Polyamide Membranes Formed by Interfacial Polymerization. *Langmuir*, 19(11), 4791-4797.

Gao, L., Ren, W., Xu, H., Jin, L., Wang, Z., Ma, T., Ma, L.-P., Zhang, Z., Fu, Q., Peng, L.-M., Bao, X., and Cheng, H.-M. (2012). Repeated growth and bubbling transfer of graphene with millimetre-size single-crystal grains using

platinum. *Nat Commun*, 3, 699.

Glater, J., Hong, S. K., and Elimelech, M. (1994). THE SEARCH FOR A CHLORINE-RESISTANT REVERSE-OSMOSIS MEMBRANE. *Desalination*, 95(3), 325-345.

Glater, J., Zachariah, M. R., McCray, S. B., and McCutchan, J. W. (1983). REVERSE-OSMOSIS MEMBRANE SENSITIVITY TO OZONE AND HALOGEN DISINFECTANTS. *Desalination*, 48(1), 1-16.

Gomez-Navarro, C., Weitz, R. T., Bittner, A. M., Scolari, M., Mews, A., Burghard, M., and Kern, K. (2007). Electronic transport properties of individual chemically reduced graphene oxide sheets. *Nano Letters*, 7(11), 3499-3503.

Goosen, M. F. A., Sablani, S. S., Ai-Hinai, H., Ai-Obeidani, S., Al-Belushi, R., and Jackson, D. (2004). Fouling of reverse osmosis and ultrafiltration membranes: A critical review. *Separation Science and Technology*, 39(10), 2261-2297.

Greenlee, L. F., Lawler, D. F., Freeman, B. D., Marrot, B., and Moulin, P. (2009). Reverse osmosis desalination: Water sources, technology, and today's challenges. *Water Research*, 43(9), 2317-2348.

Gu, J.-E., Lee, S., Stafford, C. M., Lee, J. S., Choi, W., Kim, B.-Y., Baek, K.-Y., Chan, E. P., Chung, J. Y., Bang, J., and Lee, J.-H. (2013). Molecular Layer-by-Layer Assembled Thin-Film Composite Membranes for Water Desalination. *Advanced Materials*, 25(34), 4778-4782.

- Gunawan, P., Guan, C., Song, X., Zhang, Q., Leong, S. S. J., Tang, C., Chen, Y., Chan-Park, M. B., Chang, M. W., Wang, K., and Xu, R. (2011). Hollow Fiber Membrane Decorated with Ag/MWNTs: Toward Effective Water Disinfection and Biofouling Control. *ACS Nano*, 5(12), 10033-10040.
- Hansen, C. M. (2007). *Hansen Solubility Parameters: A User's Handbook*, CRC Press, Boca Raton.
- He, H. Y., Klinowski, J., Forster, M., and Lerf, A. (1998). A new structural model for graphite oxide. *Chemical Physics Letters*, 287(1-2), 53-56.
- Hegab, H. M., Wimalasiri, Y., Ginic-Markovic, M., and Zou, L. (2015). Improving the fouling resistance of brackish water membranes via surface modification with graphene oxide functionalized chitosan. *Desalination*, 365, 99-107.
- Hirose, M., Ito, H., and Kamiyama, Y. (1996). Effect of skin layer surface structures on the flux behaviour of RO membranes. *Journal of Membrane Science*, 121(2), 209-215.
- Hu, M., and Mi, B. X. (2013). Enabling Graphene Oxide Nanosheets as Water Separation Membranes. *Environmental Science & Technology*, 47(8), 3715-3723.
- Huang, H., Qu, X., Dong, H., Zhang, L., and Chen, H. (2013). Role of NaA zeolites in the interfacial polymerization process towards a polyamide nanocomposite reverse osmosis membrane. *Rsc Advances*, 3(22), 8203-8207.

- Huang, H., Qu, X., Ji, X., Gao, X., Zhang, L., Chen, H., and Hou, L. (2013). Acid and multivalent ion resistance of thin film nanocomposite RO membranes loaded with silicalite-1 nanozeolites. *Journal of Materials Chemistry A*, 1(37), 11343-11349.
- Hummers, W. S., and Offeman, R. E. (1958). Preparation of Graphitic Oxide. *Journal of the American Chemical Society*, 80(6), 1339-1339.
- Jadav, G. L., and Singh, P. S. (2009). Synthesis of novel silica-polyamide nanocomposite membrane with enhanced properties. *Journal of Membrane Science*, 328(1-2), 257-267.
- Jena, A., and Gupta, K. (2010). Advances in Pore Structure Evaluation by Porometry. *Chemical Engineering & Technology*, 33(8), 1241-1250.
- Jeong, B. H., Hoek, E. M. V., Yan, Y. S., Subramani, A., Huang, X. F., Hurwitz, G., Ghosh, A. K., and Jawor, A. (2007). Interfacial polymerization of thin film nanocomposites: A new concept for reverse osmosis membranes. *Journal of Membrane Science*, 294(1-2), 1-7.
- Jin, F., Lv, W., Zhang, C., Li, Z., Su, R., Qi, W., Yang, Q.-H., and He, Z. (2013). High-performance ultrafiltration membranes based on polyethersulfone-graphene oxide composites. *Rsc Advances*, 3(44), 21394-21397.
- Joshi, R. K., Carbone, P., Wang, F. C., Kravets, V. G., Su, Y., Grigorieva, I. V., Wu, H. A., Geim, A. K., and Nair, R. R. (2014). Precise and Ultrafast Molecular Sieving Through Graphene Oxide Membranes. *Science*, 343(6172), 752-754.

- Kang, G., Liu, M., Lin, B., Cao, Y., and Yuan, Q. (2007). A novel method of surface modification on thin-film composite reverse osmosis membrane by grafting poly(ethylene glycol). *Polymer*, 48(5), 1165-1170.
- Kim, E.-S., and Deng, B. (2011). Fabrication of polyamide thin-film nanocomposite (PA-TFN) membrane with hydrophilized ordered mesoporous carbon (H-OMC) for water purifications. *Journal of Membrane Science*, 375(1-2), 46-54.
- Kim, E.-S., Hwang, G., Gamal El-Din, M., and Liu, Y. (2012). Development of nanosilver and multi-walled carbon nanotubes thin-film nanocomposite membrane for enhanced water treatment. *Journal of Membrane Science*, 394-395, 37-48.
- Kim, H. J., Baek, Y., Choi, K., Kim, D.-G., Kang, H., Choi, Y.-S., Yoon, J., and Lee, J.-C. (2014). The improvement of antibiofouling properties of a reverse osmosis membrane by oxidized CNTs. *Rsc Advances*, 4(62), 32802-32810.
- Kim, H. J., Choi, K., Baek, Y., Kim, D.-G., Shim, J., Yoon, J., and Lee, J.-C. (2014). High-Performance Reverse Osmosis CNT/Polyamide Nanocomposite Membrane by Controlled Interfacial Interactions. *Acs Applied Materials & Interfaces*, 6(4), 2819-2829.
- Kim, H. J., Fouda, A. E., and Jonasson, K. (2000). In situ study on kinetic behavior during asymmetric membrane formation via phase inversion process using raman spectroscopy. *Journal of Applied Polymer Science*, 75(1), 135-141.

- Kim, H. J., Lim, M.-Y., Jung, K. H., Kim, D.-G., and Lee, J.-C. (2015). High-performance reverse osmosis nanocomposite membranes containing the mixture of carbon nanotubes and graphene oxides. *Journal of Materials Chemistry A*, 3(13), 6798-6809.
- Kim, I.-C., Jeong, B.-R., Kim, S.-J., and Lee, K.-H. (2013). Preparation of high flux thin film composite polyamide membrane: The effect of alkyl phosphate additives during interfacial polymerization. *Desalination*, 308, 111-114.
- Kim, K. S., Zhao, Y., Jang, H., Lee, S. Y., Kim, J. M., Kim, K. S., Ahn, J.-H., Kim, P., Choi, J.-Y., and Hong, B. H. (2009). Large-scale pattern growth of graphene films for stretchable transparent electrodes. *Nature*, 457(7230), 706-710.
- Kim, S. G., Hyeon, D. H., Chun, J. H., Chun, B. H., and Kim, S. H. (2013). Novel thin nanocomposite RO membranes for chlorine resistance. *Desalination and Water Treatment*, 51(31-33), 6338-6345.
- Kirisits, M. J., Prost, L., Starkey, M., and Parsek, M. R. (2005). Characterization of colony morphology variants isolated from *Pseudomonas aeruginosa* biofilms. *Applied and Environmental Microbiology*, 71(8), 4809-4821.
- Kirsh, Y. E., and Popkov, Y. M. (1988). New trends in the development of polymeric materials for reverse osmosis membranes. *Russian chemical Reviews*, 57(6), 566-571.
- Koo, J. Y., Petersen, R. J., and Cadotte, J. E. (1986). ESCA characterization of

chlorine-damaged polyamide reverse-osmosis membrane. *Abstracts of Papers of the American Chemical Society*, 192, 214-POLY.

Kools (1998). Membrane formation by phase inversion in multicomponent polymer systems. University of Twente, Enschede.

Kudin, K. N., Ozbas, B., Schniepp, H. C., Prud'homme, R. K., Aksay, I. A., and Car, R. (2008). Raman spectra of graphite oxide and functionalized graphene sheets. *Nano Letters*, 8(1), 36-41.

Kumar, A., and Lee, C. H. (2013). Synthesis and biomedical applications of graphene: present and future trends. *Advances in Graphene Science*, M. Aliofkhazraei, ed., InTech, Rijeka.

Kwak, S. Y., Kim, S. H., and Kim, S. S. (2001). Hybrid organic/inorganic reverse osmosis (RO) membrane for bactericidal anti-fouling. 1. Preparation and characterization of TiO<sub>2</sub> nanoparticle self-assembled aromatic polyamide thin-film-composite (TFC) membrane. *Environmental Science & Technology*, 35(11), 2388-2394.

Lafreniere, L. Y., Talbot, F. D. F., Matsuura, T., and Sourirajan, S. (1987). EFFECT OF POLYVINYLPYRROLIDONE ADDITIVE ON THE PERFORMANCE OF POLYETHERSULFONE ULTRAFILTRATION MEMBRANES. *Industrial & Engineering Chemistry Research*, 26(11), 2385-2389.

Lalia, B. S., Kochkodan, V., Hashaikeh, R., and Hilal, N. (2013). A review on membrane fabrication: Structure, properties and performance relationship.

*Desalination*, 326, 77-95.

- Lau, W. J., Ismail, A. F., Misdan, N., and Kassim, M. A. (2012). A recent progress in thin film composite membrane: A review. *Desalination*, 287, 190-199.
- Lee, C., Wei, X., Kysar, J. W., and Hone, J. (2008). Measurement of the Elastic Properties and Intrinsic Strength of Monolayer Graphene. *Science*, 321(5887), 385-388.
- Lee, H. J., Won, J., Lee, H., and Kang, Y. S. (2002). Solution properties of poly(amic acid)-NMP containing LiCl and their effects on membrane morphologies. *Journal of Membrane Science*, 196(2), 267-277.
- Lee, H. S., Im, S. J., Kim, J. H., Kim, H. J., Kim, J. P., and Min, B. R. (2008). Polyamide thin-film nanofiltration membranes containing TiO<sub>2</sub> nanoparticles. *Desalination*, 219(1-3), 48-56.
- Lee, J.-H. Molecular assembly approach for advanced water desalination membranes. *Proc., 2014 The Membrane Society of Korea Fall Meeting*.
- Lee, J., Ahn, W. Y., and Lee, C. H. (2001). Comparison of the filtration characteristics between attached and suspended growth microorganisms in submerged membrane bioreactor. *Water Research*, 35(10), 2435-2445.
- Lee, J., Chae, H.-R., Won, Y. J., Lee, K., Lee, C.-H., Lee, H. H., Kim, I.-C., and Lee, J.-m. (2013). Graphene oxide nanoplatelets composite membrane with hydrophilic and antifouling properties for wastewater treatment. *Journal of*

*Membrane Science*, 448, 223-230.

Lee, J., Jang, J. H., Chae, H.-R., Lee, S. H., Lee, C.-H., Park, P.-K., Won, Y.-J., and Kim, I.-C. (2015). A facile route to enhance the water flux of a thin-film composite reverse osmosis membrane: incorporating thickness-controlled graphene oxide into a highly porous support layer. *Journal of Materials Chemistry A*, 3(44), 22053-22060.

Lee, K. P., Arnot, T. C., and Mattia, D. (2011). A review of reverse osmosis membrane materials for desalination—Development to date and future potential. *Journal of Membrane Science*, 370(1–2), 1-22.

Lee, S. Y., Kim, H. J., Patel, R., Im, S. J., Kim, J. H., and Min, B. R. (2007). Silver nanoparticles immobilized on thin film composite polyamide membrane: characterization, nanofiltration, antifouling properties. *Polymers for Advanced Technologies*, 18(7), 562-568.

Lerf, A., He, H. Y., Forster, M., and Klinowski, J. (1998). Structure of graphite oxide revisited. *Journal of Physical Chemistry B*, 102(23), 4477-4482.

Li, D., Muller, M. B., Gilje, S., Kaner, R. B., and Wallace, G. G. (2008). Processable aqueous dispersions of graphene nanosheets. *Nat Nano*, 3(2), 101-105.

Li, Z., Zhang, W., Luo, Y., Yang, J., and Hou, J. G. (2009). How Graphene Is Cut upon Oxidation? *Journal of the American Chemical Society*, 131(18), 6320-6321.

- Lin, X., Shen, X., Zheng, Q., Yousefi, N., Ye, L., Mai, Y.-W., and Kim, J.-K. (2012). Fabrication of Highly-Aligned, Conductive, and Strong Graphene Papers Using Ultralarge Graphene Oxide Sheets. *ACS Nano*, 6(12), 10708-10719.
- Liu, J. (2014). Charging graphene for energy. *Nature Nanotechnology*, 9(10), 739-741.
- Lloyd, D. R. (1985). *Materials science of synthetic membranes*, American Chemical Society, Washington, D.C.
- Loeb, S., and Sourirajan, S. (1963). Sea Water Demineralization by Means of an Osmotic Membrane. *Saline Water Conversion—II*, AMERICAN CHEMICAL SOCIETY, 117-132.
- Lonsdale, H. K., Merten, U., and Riley, R. L. (1965). Transport properties of cellulose acetate osmotic membranes. *Journal of Applied Polymer Science*, 9(4), 1341-1362.
- Loosdrecht, Mark C.M. Van, Norde, W., and Zehnder, A. J. B. (1990). Physical Chemical Description of Bacterial Adhesion. *Journal of Biomaterials Applications*, 5(2), 91-106.
- Marchese, J., Ponce, M., Ochoa, N. A., Pradanos, P., Palacio, L., and Hernandez, A. (2003). Fouling behaviour of polyethersulfone UF membranes made with different PVP. *Journal of Membrane Science*, 211(1), 1-11.
- Mason, E. A., and Lonsdale, H. K. (1990). STATISTICAL-MECHANICAL

THEORY OF MEMBRANE-TRANSPORT. *Journal of Membrane Science*, 51(1-2), 1-81.

McCloskey, B. D., Park, H. B., Ju, H., Rowe, B. W., Miller, D. J., Chun, B. J., Kin, K., and Freeman, B. D. (2010). Influence of polydopamine deposition conditions on pure water flux and foulant adhesion resistance of reverse osmosis, ultrafiltration, and microfiltration membranes. *Polymer*, 51(15), 3472-3485.

Miller, S., Shemer, H., and Semiat, R. (2015). Energy and environmental issues in desalination. *Desalination*, 366, 2-8.

Misdan, N., Lau, W. J., Ismail, A. F., and Matsuura, T. (2013). Formation of thin film composite nanofiltration membrane: Effect of polysulfone substrate characteristics. *Desalination*, 329, 9-18.

Mukherjee, R., Sharma, R., Saini, P., and De, S. (2015). Nanostructured polyaniline incorporated ultrafiltration membrane for desalination of brackish water. *Environmental Science: Water Research & Technology*, 1(6), 893-904.

Mulder, M. (1996). *Basic principles of membrane technology*, Kluwer Academic, Dordrecht ; Boston.

Mysels, K. J., and Wrasidlo, W. (1991). STRENGTH OF INTERFACIAL POLYMERIZATION FILMS. *Langmuir*, 7(12), 3052-3053.

Novoselov, K. S., Geim, A. K., Morozov, S. V., Jiang, D., Zhang, Y., Dubonos, S.

- V., Grigorieva, I. V., and Firsov, A. A. (2004). Electric Field Effect in Atomically Thin Carbon Films. *Science*, 306(5696), 666-669.
- Oki, T., and Kanae, S. (2006). Global hydrological cycles and world water resources. *Science*, 313(5790), 1068-1072.
- Otsu, N. (1979). A threshold selection method from gray-level histograms. *IEEE Transactions on Systems, Man and Cybernetics*, 9(1), 62-66.
- Pandey, D., Reifengerger, R., and Piner, R. (2008). Scanning probe microscopy study of exfoliated oxidized graphene sheets. *Surface Science*, 602(9), 1607-1613.
- Pang, C. M., Hong, P. Y., Guo, H. L., and Liu, W. T. (2005). Biofilm formation characteristics of bacterial isolates retrieved from a reverse osmosis membrane. *Environmental Science & Technology*, 39(19), 7541-7550.
- Paredes, J. I., Villar-Rodil, S., Martinez-Alonso, A., and Tascon, J. M. D. (2008). Graphene oxide dispersions in organic solvents. *Langmuir*, 24(19), 10560-10564.
- Park, S., and Ruoff, R. S. (2009). Chemical methods for the production of graphenes. *Nature Nanotechnology*, 4(4), 217-224.
- Pendergast, M. M., Ghosh, A. K., and Hoek, E. M. V. (2013). Separation performance and interfacial properties of nanocomposite reverse osmosis membranes. *Desalination*, 308, 180-185.

- Perreault, F., Tousley, M. E., and Elimelech, M. (2013). Thin-Film Composite Polyamide Membranes Functionalized with Biocidal Graphene Oxide Nanosheets. *Environmental Science & Technology Letters*, 1(1), 71-76.
- Petersen, R. J. (1993). COMPOSITE REVERSE-OSMOSIS AND NANOFILTRATION MEMBRANES. *Journal of Membrane Science*, 83(1), 81-150.
- Petty, M. C. (1996). *Langmuir-Blodgett Films*, Cambridge University Press.
- Porter, M. C. (1990). *Handbook of Industrial Membrane Technology*, Noyes publications, New Jersey.
- Potts, J. R., Dreyer, D. R., Bielawski, C. W., and Ruoff, R. S. (2011). Graphene-based polymer nanocomposites. *Polymer*, 52(1), 5-25.
- Rafiee, M. A., Rafiee, J., Wang, Z., Song, H., Yu, Z.-Z., and Koratkar, N. (2009). Enhanced Mechanical Properties of Nanocomposites at Low Graphene Content. *ACS Nano*, 3(12), 3884-3890.
- Rajabzadeh, S., Maruyama, T., Ohmukai, Y., Sotani, T., and Matsuyama, H. (2009). Preparation of PVDF/PMMA blend hollow fiber membrane via thermally induced phase separation (TIPS) method. *Separation and Purification Technology*, 66(1), 76-83.
- Rajabzadeh, S., Maruyama, T., Sotani, T., and Matsuyama, H. (2008). Preparation of PVDF hollow fiber membrane from a ternary polymer/solvent/nonsolvent

- system via thermally induced phase separation (TIPS) method. *Separation and Purification Technology*, 63(2), 415-423.
- Riley, P. L., Milstead, C. E., Lloyd, A. L., Seroy, M. W., and Tagami, M. (1977). Spiral-wound thin-film composite membrane systems for brackish and seawater desalination by reverse osmosis. *Desalination*, 23(1), 331-355.
- Riley, R. L., Lonsdale, H. K., and Lyons, C. R. (1971). COMPOSITE MEMBRANES FOR SEAWATER DESALINATION BY REVERSE OSMOSIS. *Journal of Applied Polymer Science*, 15(5), 1267-&.
- Rosenberg, M., Gutnick, D., and Rosenberg, E. (1980). ADHERENCE OF BACTERIA TO HYDROCARBONS - A SIMPLE METHOD FOR MEASURING CELL-SURFACE HYDROPHOBICITY. *FEMS Microbiology Letters*, 9(1), 29-33.
- Saleh, T. A., and Gupta, V. K. (2012). Synthesis and characterization of alumina nano-particles polyamide membrane with enhanced flux rejection performance. *Separation and Purification Technology*, 89(0), 245-251.
- Schedin, F., Geim, A. K., Morozov, S. V., Hill, E. W., Blake, P., Katsnelson, M. I., and Novoselov, K. S. (2007). Detection of individual gas molecules adsorbed on graphene. *Nat Mater*, 6(9), 652-655.
- Shang, J., Ma, L., Li, J., Ai, W., Yu, T., and Gurzadyan, G. G. (2012). The Origin of Fluorescence from Graphene Oxide. *Scientific Reports*, 2.

- Shaw, D. (1994). *Introduction to colloid and surface chemistry*, Butterworth/Heinemann, Boston.
- Shi, H., Liu, F., and Xue, L. (2013). Fabrication and characterization of antibacterial PVDF hollow fibre membrane by doping Ag-loaded zeolites. *Journal of Membrane Science*, 437, 205-215.
- Shimizu, R., Everhart, T. E., Macdonald, N. C., and Hovland, C. T. (1978). EDGE EFFECT IN HIGH-RESOLUTION SCANNING AUGER-ELECTRON MICROSCOPY. *Applied Physics Letters*, 33(6), 549-551.
- Smolders, C. A., Reuvers, A. J., Boom, R. M., and Wienk, I. M. (1992). MICROSTRUCTURES IN PHASE-INVERSION MEMBRANES .1. FORMATION OF MACROVOIDS. *Journal of Membrane Science*, 73(2-3), 259-275.
- Song, C., and Corry, B. (2009). Intrinsic Ion Selectivity of Narrow Hydrophobic Pores. *The Journal of Physical Chemistry B*, 113(21), 7642-7649.
- Song, Y. J., Sun, P., Henry, L. L., and Sun, B. H. (2005). Mechanisms of structure and performance controlled thin film composite membrane formation via interfacial polymerization process. *Journal of Membrane Science*, 251(1-2), 67-79.
- Stankovich, S., Dikin, D. A., Dommett, G. H. B., Kohlhaas, K. M., Zimney, E. J., Stach, E. A., Piner, R. D., Nguyen, S. T., and Ruoff, R. S. (2006). Graphene-based composite materials. *Nature*, 442(7100), 282-286.

- Stankovich, S., Dikin, D. A., Piner, R. D., Kohlhaas, K. A., Kleinhammes, A., Jia, Y., Wu, Y., Nguyen, S. T., and Ruoff, R. S. (2007). Synthesis of graphene-based nanosheets via chemical reduction of exfoliated graphite oxide. *Carbon*, 45(7), 1558-1565.
- Strathmann, H. (1985). PRODUCTION OF MICROPOROUS MEDIA BY PHASE INVERSION PROCESSES. *ACS Symposium Series*, 269, 165-195.
- Strathmann, H., and Kock, K. (1977). The formation mechanism of phase inversion membranes. *Desalination*, 21(3), 241-255.
- Sun, G., Chung, T.-S., Jeyaseelan, K., and Armugam, A. (2013). A layer-by-layer self-assembly approach to developing an aquaporin-embedded mixed matrix membrane. *Rsc Advances*, 3(2), 473-481.
- Szabo, T., Berkesi, O., and Dekany, I. (2005). DRIFT study of deuterium-exchanged graphite oxide. *Carbon*, 43(15), 3186-3189.
- Tiraferri, A., Vecitis, C. D., and Elimelech, M. (2011). Covalent Binding of Single-Walled Carbon Nanotubes to Polyamide Membranes for Antimicrobial Surface Properties. *Acs Applied Materials & Interfaces*, 3(8), 2869-2877.
- Tiraferri, A., Vecitis, C. D., and Elimelech, M. (2011). Covalent Binding of Single-Walled Carbon Nanotubes to Polyamide Membranes for Antimicrobial Surface Properties. *Acs Applied Materials & Interfaces*, 3(8), 2869-2877.
- Tiraferri, A., Yip, N. Y., Phillip, W. A., Schiffman, J. D., and Elimelech, M. (2011).

Relating performance of thin-film composite forward osmosis membranes to support layer formation and structure. *Journal of Membrane Science*, 367(1-2), 340-352.

Torrise, F., and Coleman, J. N. (2014). Electrifying inks with 2D materials. *Nature Nanotechnology*, 9(10), 738-739.

Veldkamp, T. I. E., Wada, Y., de Moel, H., Kumm, M., Eisner, S., Aerts, J. C. J. H., and Ward, P. J. (2015). Changing mechanism of global water scarcity events: Impacts of socioeconomic changes and inter-annual hydro-climatic variability. *Global Environmental Change*, 32, 18-29.

Wang, G., Wang, B., Park, J., Yang, J., Shen, X., and Yao, J. (2009). Synthesis of enhanced hydrophilic and hydrophobic graphene oxide nanosheets by a solvothermal method. *Carbon*, 47(1), 68-72.

Wang, H., Yu, T., Zhao, C., and Du, Q. (2009). Improvement of hydrophilicity and blood compatibility on polyethersulfone membrane by adding polyvinylpyrrolidone. *Fibers and Polymers*, 10(1), 1-5.

Wang, J., Gao, X., Wang, J., Wei, Y., Li, Z., and Gao, C. (2015). O-(Carboxymethyl)-chitosan Nanofiltration Membrane Surface Functionalized with Graphene Oxide Nanosheets for Enhanced Desalting Properties. *ACS Applied Materials & Interfaces*, 7(7), 4381-4389.

Wang, X., Chen, X., Yoon, K., Fang, D., Hsiao, B. S., and Chu, B. (2005). High Flux Filtration Medium Based on Nanofibrous Substrate with Hydrophilic

- Nanocomposite Coating. *Environmental Science & Technology*, 39(19), 7684-7691.
- Wang, X., Wang, L., Zhao, F., Hu, C., Zhao, Y., Zhang, Z., Chen, S., Shi, G., and Qu, L. (2015). Monoatomic-thick graphitic carbon nitride dots on graphene sheets as an efficient catalyst in the oxygen reduction reaction. *Nanoscale*, 7(7), 3035-3042.
- Wang, X., Zhi, L., and Müllen, K. (2008). Transparent, Conductive Graphene Electrodes for Dye-Sensitized Solar Cells. *Nano Letters*, 8(1), 323-327.
- Wang, Z., Yu, H., Xia, J., Zhang, F., Li, F., Xia, Y., and Li, Y. (2012). Novel GO-blended PVDF ultrafiltration membranes. *Desalination*, 299, 50-54.
- Wenzel, R. N. (1936). Resistance of solid surfaces to wetting by water. *Industrial and Engineering Chemistry*, 28, 988-994.
- Witte, P. van de, Dijkstra, P. J., vandenBerg, J. W. A., and Feijen, J. (1996). Phase separation processes in polymer solutions in relation to membrane formation. *Journal of Membrane Science*, 117(1-2), 1-31.
- Wojtoniszak, M., Chen, X., Kalenczuk, R. J., Wajda, A., Lapczuk, J., Kurzewski, M., Drozdik, M., Chu, P. K., and Borowiak-Palen, E. (2012). Synthesis, dispersion, and cytocompatibility of graphene oxide and reduced graphene oxide. *Colloids and Surfaces B-Biointerfaces*, 89, 79-85.
- Wu, H., Tang, B., and Wu, P. (2010). MWNTs/Polyester Thin Film Nanocomposite

Membrane: An Approach To Overcome the Trade-Off Effect between Permeability and Selectivity. *The Journal of Physical Chemistry C*, 114(39), 16395-16400.

Wu, L., Liu, L., Gao, B., Munoz-Carpena, R., Zhang, M., Chen, H., Zhou, Z., and Wang, H. (2013). Aggregation Kinetics of Graphene Oxides in Aqueous Solutions: Experiments, Mechanisms, and Modeling. *Langmuir*, 29(49), 15174-15181.

Xie, J., and Spallas, J. P. (2012). Different Contrast Mechanisms in SEM Imaging of Graphene. Agilent Technologies, Santa Clara.

Xie, W., Geise, G. M., Freeman, B. D., Lee, H.-S., Byun, G., and McGrath, J. E. (2012). Polyamide interfacial composite membranes prepared from m-phenylene diamine, trimesoyl chloride and a new disulfonated diamine. *Journal of Membrane Science*, 403–404, 152-161.

Yang, R., Xu, J., Ozaydin-Ince, G., Wong, S. Y., and Gleason, K. K. (2011). Surface-Tethered Zwitterionic Ultrathin Antifouling Coatings on Reverse Osmosis Membranes by Initiated Chemical Vapor Deposition. *Chemistry of Materials*, 23(5), 1263-1272.

Yang, S.-T., Chang, Y., Wang, H., Liu, G., Chen, S., Wang, Y., Liu, Y., and Cao, A. (2010). Folding/aggregation of graphene oxide and its application in Cu<sup>2+</sup> removal. *Journal of Colloid and Interface Science*, 351(1), 122-127.

Yang, Y., Yang, X., Yang, W., Li, S., Xu, J., and Jiang, Y. (2014). Ordered and

ultrathin reduced graphene oxide LB films as hole injection layers for organic light-emitting diode. *Nanoscale Research Letters*, 9(1), 1-6.

Yang, Y., Zhang, H., Wang, P., Zheng, Q., and Li, J. (2007). The influence of nano-sized TiO<sub>2</sub> fillers on the morphologies and properties of PSF UF membrane. *Journal of Membrane Science*, 288(1–2), 231-238.

Yin, J., and Deng, B. (2015). Polymer-matrix nanocomposite membranes for water treatment. *Journal of Membrane Science*, 479, 256-275.

Yin, J., Kim, E.-S., Yang, J., and Deng, B. (2012). Fabrication of a novel thin-film nanocomposite (TFN) membrane containing MCM-41 silica nanoparticles (NPs) for water purification. *Journal of Membrane Science*, 423, 238-246.

Yin, J., Yang, Y., Hu, Z., and Deng, B. (2013). Attachment of silver nanoparticles (AgNPs) onto thin-film composite (TFC) membranes through covalent bonding to reduce membrane biofouling. *Journal of Membrane Science*, 441, 73-82.

Yin, J., Zhu, G., and Deng, B. (2016). Graphene oxide (GO) enhanced polyamide (PA) thin-film nanocomposite (TFN) membrane for water purification. *Desalination*, 379, 93-101.

Zhang, S., Qiu, G., Ting, Y. P., and Chung, T.-S. (2013). Silver-PEGylated dendrimer nanocomposite coating for anti-fouling thin film composite membranes for water treatment. *Colloids and Surfaces A: Physicochemical and Engineering Aspects*, 436, 207-214.

- Zhao, H. Y., Qiu, S., Wu, L. G., Zhang, L., Chen, H. L., and Gao, C. J. (2014). Improving the performance of polyamide reverse osmosis membrane by incorporation of modified multi-walled carbon nanotubes. *Journal of Membrane Science*, 450, 249-256.
- Zhao, H. Y., Wu, L. G., Zhou, Z. J., Zhang, L., and Chen, H. L. (2013). Improving the antifouling property of polysulfone ultrafiltration membrane by incorporation of isocyanate-treated graphene oxide. *Physical Chemistry Chemical Physics*, 15(23), 9084-9092.
- Zheng, Q.-Z., Wang, P., Yang, Y.-N., and Cui, D.-J. (2006). The relationship between porosity and kinetics parameter of membrane formation in PSF ultrafiltration membrane. *Journal of Membrane Science*, 286(1-2), 7-11.
- Zodrow, K., Brunet, L., Mahendra, S., Li, D., Zhang, A., Li, Q., and Alvarez, P. J. J. (2009). Polysulfone ultrafiltration membranes impregnated with silver nanoparticles show improved biofouling resistance and virus removal. *Water Research*, 43(3), 715-723.